2019

Multi-Sensor Approach to Determine the Effect of Geometry on Microstructure in Additive Manufacturing

Joseph R. Walker
Wright State University

MULTI-SENSOR APPROACH TO DETERMINE THE EFFECT OF GEOMETRY ON MICROSTRUCTURE IN ADDITIVE MANUFACTURING

A thesis submitted in partial fulfillment of the requirements for the degree of Master of Science in Materials Science and Engineering

By

JOSEPH R. WALKER
B.S.M.E, Wright State University, 2017

2019
Wright State University

WRIGHT STATE UNIVERSITY
GRADUATE SCHOOL

April 10, 2019

I HEREBY RECOMMEND THAT THE THESIS PREPARED UNDER MY SUPERVISION BY **Joseph R. Walker** ENTITLED **Multi-Sensor Approach to Determine the Effect of Geometry on Microstructure in Additive Manufacturing** BE ACCEPTED IN PARTIAL FULFILLMENT OF THE REQUIREMENTS FOR THE DEGREE OF Masters of Science in Materials Science Engineering**.**

_____
Joy Gockel, Ph.D.
Thesis Director

_____
Joseph C. Slater, Ph.D., P.E.
Chair, **Mechanical & Material Engineering**

Committee on Final Examination:

_____
Joy Gockel, Ph.D.

_____
John Middendorf, Ph.D.

_____
Nathan W. Klingbeil, Ph.D.

_____
Barry Milligan, Ph.D.
Interim Dean of the Graduate School

ABSTRACT

Walker, Joseph R., M.S.M.S.E. Department of Mechanical and Materials Engineering, Wright State University, 2019. Multi-Sensor Approach to Determine the Effect of Geometry on Microstructure in Additive Manufacturing.

Laser powder bed fusion (LPBF) is an additive manufacturing technique used for making complex parts through a layer-by-layer process with fine feature resolution. However, the layer-by-layer process, with complex scanning patterns within each layer, introduces variability in thermal behavior leading to inconsistent microstructure and defects. The in-situ process monitoring approach in this work uses sensors including a high-speed visible camera, thermal camera, and spectrometer to evaluate each location in the LPBF process. Each sensor focuses on a different process phenomenon such as the melt pool or thermal behavior. An experimental study, using metallographic analysis and collection of sensor data, is used to determine the influence of processing parameters and geometric changes on the final microstructure of Alloy 718. The multi-sensor approach creates a comprehensive view of the microstructural changes. Combining in-situ process monitoring with process control allows for the prediction of part quality and reliable material properties.

TABLE OF CONTENTS

LIST OF FIGURES

LIST OF EQUATIONS

LIST OF TABLES

Chapter 1: Introduction and Literature Review

1.1 Additive Manufacturing

1.1.1 General overview

Additive Manufacturing (AM) is a complex and powerful tool that has the capability of replacing traditional manufacturing techniques for new, more efficient means. Traditionally, manufacturers create casts out of metal to mold molten material into various shapes for commercial use. This system is beneficial for many applications along with other forms such as forging, pressing, and rolling. These traditional methods all have areas for which they are well suited. With casting, a simple mold can produce millions of parts efficiently and cost effectively. However, this method cannot make complex parts with internal features. An example of impossible geometrical structures are integrated lattice structures or variable internal channels. Both of these designs can be useful, and AM can create them. By creating these parts in a layer-by-layer process, many new techniques hold the capability to create complex parts. AM is capable of making many complex designs that are impossible to create otherwise. This creates a strong demand for the manufacturing community. There are many different AM systems available, all with strengths and weakness.

There are various types of AM 3-Dimentional (3D) printers available. The most common 3D printers are polymer printers known as Fusion Deposition Modeling (FDM). The FDM printers use a thermoplastic polymer material as filament, and a heated nozzle to distribute the filament. This makes the FDM printer inexpensive and thus more widely used. Figure 1.1 displays FDM and other common 3D printer.

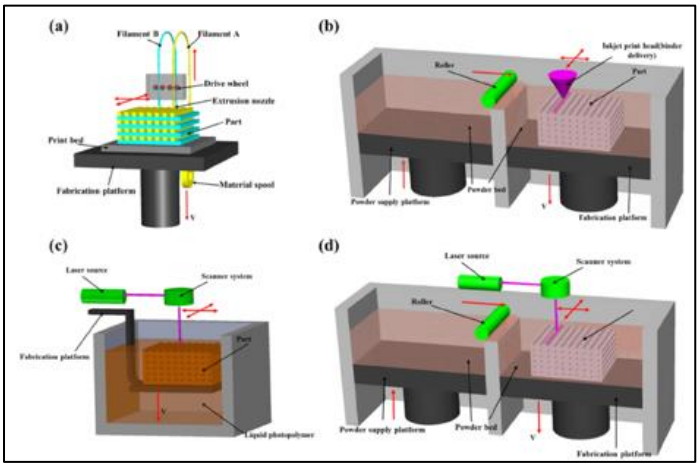

Figure 1.1: Types of 3D Printers. a) FDM, b) Ink Jet, c) Stereolithographic, d) LPBF [1].

Other AM systems that use stronger materials, such as metal, are in a different class of 3D printers based on the capabilities, operation, and purchasing price. Another common printing style is Stereolithographic, which uses a resin and UV light to cure the resin leaving a solidified part. Laser Powder Bed Fusion (LPBF) uses metal powder as the material and laser optics as the heat source. Similar to this, 3D Binder Jet printing uses powders, however the melting source normally occurs in a kiln after the printing process. Other 3D printers include Direct Energy Deposition (DED), Laser Deposition (LD) and Laminated Object Manufacturing (LOM) [2]. Each type includes benefits and drawbacks.

1.1.1.1 Fusion Deposition Modeling

FDM printers are the most common because of the low purchasing cost and the ease of use. The material available for FDM printers is vast, all having various melting temperatures and strengths such as PLA, ABS, Nylon, and Flex [1]. FDM has a heated nozzle that controls the melting temperature of the filament. The nozzle heats the thermoplastic filament close to the melting temperature to allow the molding of the filament, which is then deposited in lines along a build plate. This repeats every layer until the desired part is complete. The temperatures range from 200˚ C to just below 300˚ C.

The advantage of FDM printers is primarily the price, ease of use, simplicity of the printer's design, and the capability for multiple material builds. These allow for rapid prototype production, which makes FDM a useful tool in any manufacturing field. However, FDM has a number of drawbacks is limited by the material. The material needs to be in a filament form in order to enter the nozzle, and the material needs to be thermoplastic with a high enough viscosity for deposition, and a low enough viscosity to push through the extruder [1]. FDM printers are a perfect tool for low cost manufacturing. Once a demand for more strength appears, the optimal printers are metal based.

1.1.1.2 Metal 3D Printers

1.1.1.2.1 Laser Powder Bed Fusion

In LPBF, there are two reservoirs, one containing the metal powder, also known as the supply, and the other containing the build plate or substrate. The process consists of a layer of metal powder coated over the build plate by a roller or recoater. Located above the substrate is a scan head that will use a laser to melt the powder in the shape of the part. The laser melts the powder based on the part design. The build plate lowers in small increments,

typically 20-50 µm, the reservoir containing the powder raises and the recoater scrapes another layer of powder over the previous layer. This layer-by-layer process continues until the part is finished. The advantages of LPBF printers are the high accuracy and resolution that comes from the laser, the capability for complex designs, and the dimensional control over the process [3].

1.1.1.2.2 Direct Energy Deposition

The final 3D printing techniques is Direct Laser Deposition (DLD). This technique is similar to LPBF because it uses metal powder and a laser to create a part. The difference is that a nonreactive gas sprays the powder in front of the laser. The laser then melts the powder that lands in front of the laser nozzle. The two main ways DLD utilizes this technique is either by keeping the build plate stationary while the laser head and powder spray move to draw the part, or the laser head is stationary while the build plate moves to draw the part [3]. Figure 1.2 illustrates the DLD process.

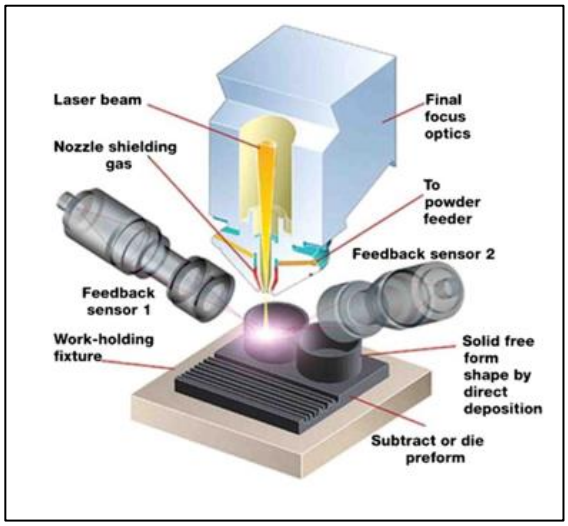

Figure 1.2: Illustration of DLD 3D Printer [4]

The advantages of using DLD include the ability to have a moving laser head enabling the repair of existing metal parts, build sizes can be much larger than LPBF, a

small heat affected zone, and the utilization of both powder and feed stock [5]. These make DLD a versatile 3D printer. All of the previous metal printers have the capability to use different metal powder to produce parts. In this research, Alloy 718 will be the main material used for all experiments.

1.2 Alloy 718

1.2.1 History

Alloy 718 is a superalloy that consists of many different elements that collectively produce the vast composition. This superalloy began in the 1920's when there was a need for high strength material that could withstand elevated temperatures. The main advancement in superalloys became apparent when turbine engines became a leading participant. In a turbine engine there are many factors contributing to a materials deformation, the most important being temperature. The typical steels and irons could not withstand high temperatures and maintain their strength. This limited the types of materials usable in turbine engines. This exploded the superalloys race that continues today. Now, cobalt-nickel-iron alloys are the main superalloys used specifically for their elevated working temperature range and corrosion resistance. The nickel and cobalt-based superalloys became increasingly expensive to use so the nickel-iron-based superalloys became a leading superalloy in the industry. Figure 1.3 displays the composition for one commercially available alloy 718 product [6].

Element	Typical Composition
Aluminum (Al)	0.03 - 0.70
Bismuth (Bi)	0.00005 max
Boron (B)	0.006 max
Calcium (Ca)	0.01 max
Carbon (C)	0.02 - 0.08
Chromium (Cr)	17.00 - 21.00
Cobalt (Co)	1.00 max
Copper (Cu)	0.30 max
Iron (Fe)	15.00 - 21.00
Magnesium (Mg)	0.01 max
Manganese (Mn)	0.35 max
Molybdenum (Mo)	2.80 - 3.30
Nickel (Ni)	50.00 - 55.00
Niobium (Nb) + Tantalum (Ta)	4.75 - 5.50
Phosphorus (P)	0.015 max
Selenium (Se)	0.005 max
Silicon (Si)	0.35 max
Sulfur (S)	0.015 max
Tantalum (Ta)	0.50 max
Titanium (Ti)	0.75 - 1.15

Figure 1.3: Alloy 718 Composition [7].

1.2.2 Background/Creation/Evolution

The composition of alloy 718 has many elements that give slight advantages. The nickel, iron, and chromium are responsible for the oxidation resistance. Later titanium, aluminum, and niobium increased the composition to give the material the phase gamma prime, which gives the benefit of creep resistance. However, if too much of these elements combine, the material will become significantly more brittle. Aluminum provides the gamma prime structure that reduces the oxidation of the material. Iron decreased from the composition in favor of cobalt and nickel. The addition of materials that are refractory increased the strength retention at high temperature. These materials consist of molybdenum, tantalum, tungsten, and rhenium. Molybdenum creates solid solution and carbides, which produces a significant strength increase [8].

Chromium produces the main corrosion resistance in the composition, but due to the increase of other elements, the chromium needed to decrease specifically as the aluminum percent increased. This led to an increase in the high temperature strengthening.

However, as the percent of chromium decreased quickly, “hot corrosion” increased which led to more careful reduction of chromium [8].

Solid-state reactions are responsible for the carbide forming at the grain boundaries. This is a positive impact of carbon because it creates point strengtheners that reduce the chance of recrystallization. The materials consist of carbon, zirconium, and boron. However, as better process developed the composition changed again to create better stronger material [8].

1.2.3 Microstructure

The microstructure of alloy 718 is a complex arrangement of multiple phases that can both add to the strength of the material, or lead to a reduction in other important properties, such as creep rupture. Alloy 718 has a variety of phases through the material and each phase can have its own crystal structure. A crystal structure is an identifiable orientation of atoms arranged into a known and common orientation. It is not important to cover all of the crystal structures seen in alloy 718 because not all of them are present in LPBF AM. Five important crystal structures appear in alloy 718: Face-centered cubic (FCC), Body-Centered Cubic (BCC), Hexagonal Close-Packed (HCP), Geometrically Close-Packed (GCP), and Body-Centered Tetragonal (BCT) [6]. Figure 1.4 illustrates these structures. Each phase in alloy 718 will be made of one of these crystal structures not including sigma (σ), and delta (δ). There are many phases in alloy 718, each one introduce benefits and possible drawbacks.

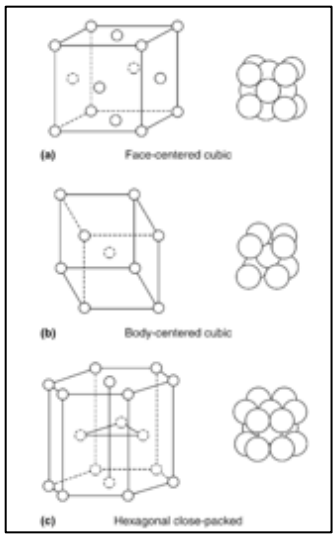

Figure 1.4: Line Drawings of a) FCC, b) BCC, c) HCP [6].

1.2.3.1 Phases

The main phase that makes up a majority of the composition in alloy 718 is the austenitic FCC matrix gamma (γ) phase. The matrix phase is full of secondary phases that contribute to the material strength. Some of the secondary phases that contribute well to the material are the carbides with FCC crystal structures. These consist of MC, $M_{23}C_6$, M_6C, and M_7C_3. In addition to this, the secondary phases that contribute to the materials strength are: FCC ordered gamma prime (γ'), the FCC ordered gamma double prime (γ"), the hexagonal eta (η), and finally the orthorhombic delta (δ) phase. More phases that contribute to the microstructure these however, are the main strengthening phases in alloy 718. With the manipulation of these phases, and grain size control, it is possible to maintain a material that meets the characteristics of a superalloy [6].

Superalloys gain their strength when these phases combined in various ways that creates solid solution strengthening and precipitate strengthening. Strengthening can also occur at the grain boundaries with the help of carbides as previously mentions. The carbides

form along the grain boundaries, which increases the shear resistance because the carbides act as point defect and hardeners [6]. From these solid solutions and precipitates, other materials form the gamma prime and carbides. These elements can be boron, zirconium, and hafnium. These elements add the chemical properties of the superalloys.

Not all phases in superalloys are desirable; some are harmful to the properties of superalloys. These phases are the sigma (σ), mew (μ), and laves. These phases are Topologically Close-Packed (TCP) and are not harmful in small amounts, but once the amount increases, it is harmful to the superalloy [6]. The elements that contribute to these phases are cobalt, molybdenum, tungsten, rhenium, and chromium. All elements originally added for beneficial characteristics, but when too much accumulates, it creates detrimental phases.

The major elements that contribute the superalloys strengths can be broken down into physical properties. Some of the elements produce solid solution strengthening such as molybdenum, tantalum, tungsten, and rhenium. Other elements that contribute to the oxidation resistance are chromium, and aluminum. Titanium and nickel contribute to the hot corrosion resistance and phase stability. Precipitate hardeners such as gamma prime come from aluminum and titanium. In addition to this, niobium creates gamma double prime. Other elements contribute to grain boundary strengthening, such as carbon and boron, producing carbides and borides. Other elements that control the grain boundary come from boron, zirconium, and hafnium. As previously stated, carbides and grain boundary strengtheners create shear resistance [6].

Lastly, the detrimental elements that combined in large doses produce property reduction in superalloys. These elements consist of silicon, phosphorous, sulfur, lead,

bismuth, tellurium, selenium, and silver [6]. These elements are difficult to monitor because they do not appear in optical microscopes. Other elements are able to eliminate some of the detrimental elements. For example, magnesium can eliminate some sulfur on the grain boundary, while titanium is able to react with nitrogen to create Titanium Nitride (TiN) which allows these elements to appear in a microscope.

1.2.3.1.1 Gamma Matrix (γ)

The matrix is the primary source of material used as a building block for all other phases. The matrix combines with different types of particles that will strengthen the overall material. Gamma is a non-magnetic phase that is mostly comprised of chromium, cobalt, iron, tungsten, and molybdenum. These elements form an FCC crystal structure [6] [8] [9]. Figure 1.5 is an example of the matrix phases in an alloy 718 microstructure.

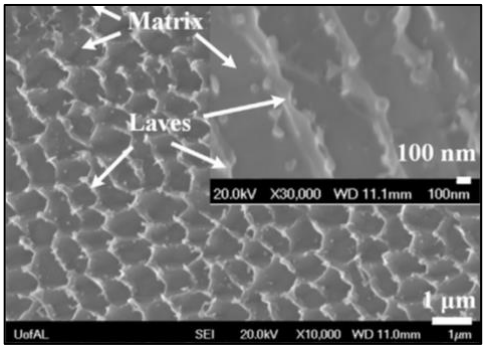

Figure 1.5: Image of Gamma Matrix [10].

Figure 1.5 shows the difference between the matrix and other secondary phases in the microstructure. The matrix appears darker based on the number of electrons in the material.

1.2.3.1.2 Gamma Prime (γ')

When created correctly, the gamma prime phase will form into spheres or cuboids that work in the gamma matrix. This creates the precipitate that is normally composed of

aluminum and titanium, but also forms with niobium, tantalum, and chromium [6]. Figure 1.6 displays cuboid and spherical gamma prime phases of nickel-based superalloy.

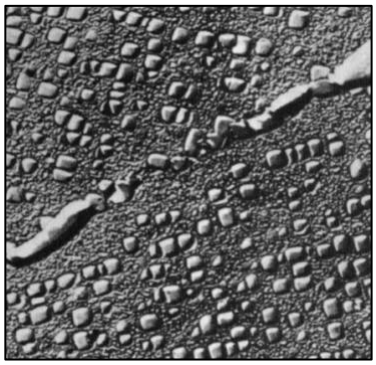

Figure 1.6: Cuboidal and spherical Gamma Prime Phase in a nickel-based superalloy [6].

Gamma prime has a crystal structure of FCC and is the primary precipitate for high temperature strengthening [6] [8]. The shape of gamma prime can change with varying levels of aluminum, titanium, and molybdenum. The shape will change the order of spherical, globular, blocky, and cuboidal. This change in shape directly relates to the mismatch between the gamma prime percentages compared to the gamma matrix. As the mismatch increases, the shape of gamma prime will change. If the change in shape occurs at an elevated temperature above 700˚ C then the secondary phases delta and eta will form and be detrimental to the strength that gamma prime is responsible for [6] [8] [9]. Based on the heat treatment of the superalloy the gamma prime phases can also form in films or rafts around the grain boundary with the capabilities to increase the creep rupture strength of the metal [6].

1.2.3.1.3 Eta (η)

Eta has an HCP crystal structure that emerges if high aluminum and titanium ratios appear in the material and are exposed to high temperatures for long periods. The formation takes an acicular shape with platelets that from in a Widmanstätten pattern [6] [8].

1.2.3.1.4 Gamma Double Prime (γ")

Gamma double prime forms in a few nickel-iron based alloys, and produces high strength in moderate temperatures. Gamma double prime is also the main strengthener of alloy 718 [11]. Gamma double prime does however, loose the strength once temperatures rises above 650C [6]. This phase creates the strength from a large mismatch between the precipitates and the matrix, which is approximately 2.9%. Gamma double prime forms with the combination of nickel and niobium and with the help of iron. This combination creates the BCT crystal structure Ni_3Nb [6] [8]. In Figure 1.7, a combination of gamma prime and gamma double prime is present. These two phases normally form together in a similar fashion.

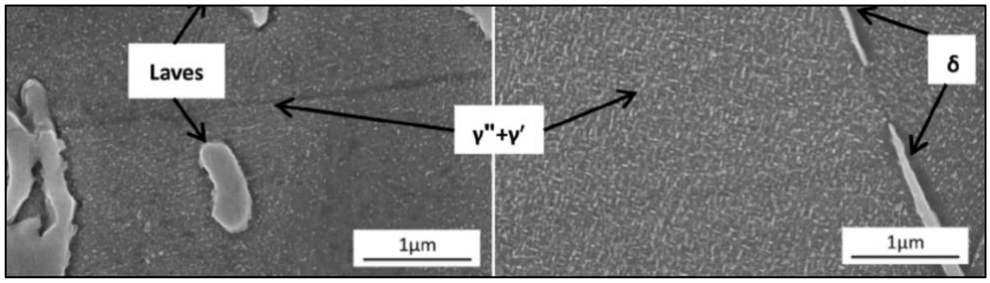

Figure 1.7: Gamma Prime and Gamma Double Prime in the Matrix phase [12].

Without iron, the formation of gamma double prime changes. Under specific conditions instead of gamma double prime forming, delta phase will form instead. Both phases have the same chemical formula, Ni_3Nb, which is why the heat treatment of the material is very delicate [6]. Delta phase can produce improved properties such as tensile strength, fatigue life, and creep rupture. However, this is only if there are very small amounts of delta phase present that help create structure along the grain boundaries, and if there is too much, it is detrimental to the strength due to the lack of gamma double prime [6] [8] [13].

1.2.3.1.5 Delta (δ)

Delta phase has an orthorhombic crystal structure with the formula Ni_3Nb, similar to gamma double prime. The formation of delta phase happens two separate ways. First, at low temperatures delta phase forms by cellular reaction and secondly, at high temperatures it forms by intergranular precipitation [6]. Delta phase can also form into a film like precipitate depending on the amount of phosphorus present, which decreases the presence of delta phase when more silicon is present [14]. Delta phase precipitates affect the ductility of the material at 650° C [15]. Although there is a loss of strength, at room temperature, there is no loss of tensile strength or hardness because of the delta phase [16]. In Figure 1.8 delta phase appears at the grain boundary with acicular shapes.

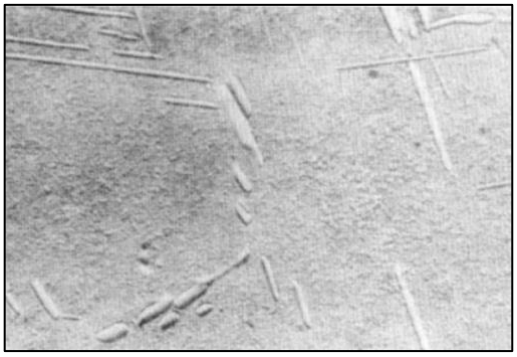

Figure 1.8: Delta Phase present at the grain boundary [6].

These needle-like shapes help few properties in small doses. The heat treatment of this superalloy needs to be extremely delicate to produce desirable results [6] [8] [9]. Delta phase produces control over grain growth, but if the delta phases does not form, the carbides are able to perform the same grain growth stability [17].

1.2.3.1.6 Carbides (MC)

Carbides come in many different forms, and the nomenclature changes depending on their location and mating species. Carbides form when 0.02-0.2% carbon is present, and reacts to various elements in the microstructure.

MC Carbides take the cubic crystal structure and form with elements such as titanium, niobium, tantalum, hafnium, thorium, and zirconium. The shape of this carbide is globular and irregular [6]. MC Carbides generally dissolve into other carbides in this list, which form at the grain boundaries. MC is known as a high temperature carbide, and the most common carbide. One drawback of carbides is the fact that immediately surrounding the carbide there are precipitation free zones that inhibit the strength and structure of alloy 718 [18].

$M_{23}C_6$ Carbides have an FCC crystal structure and usually form with the elements chromium, iron, molybdenum and tungsten. The orientations of this carbide come in many different varieties: films, globs, platelets, lamellae, and cells, which appear at the grain boundary. This carbide forms at temperatures ranging from 760-980˚ C and is mostly comprised of chromium [8].

M_6C carbides also have an FCC crystal structure that normally form with molybdenum or tungsten but can also form with chromium, nickel, niobium, tantalum, and cobalt. These carbides generally form randomly throughout the microstructure at temperatures ranging from 815-980˚ C [8]. This carbide forms as an intermediate temperature carbide [6].

M_7C_3 carbides have a hexagonal crystal structure with an irregular blocky shape. They are normally seen in cobalt based superalloys so will not be covered in-depth. This

carbide forms as a low temperature carbide. Figure 1.9 shows the different shape and orientation of two different carbides in a nickel-based superalloy.

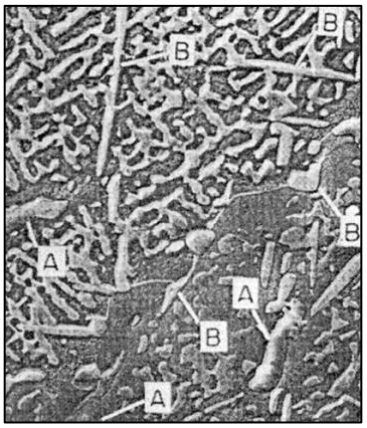

Figure 1.9: Carbide formation (A) points to MC carbides while (B) points to M_6C carbides [6].

Carbides normally form at temperatures around 800-1000˚ C but can form at 1050˚ C and facilitate three important functions. Carbides that form at the grain boundary strengthen the grain boundary by preventing sliding and allow stress relaxation. Carbides that form randomly in the matrix help strengthen the material, similar to gamma prime and gamma double prime. This is especially important for cobalt-based superalloys because of the missing gamma prime phase due to low iron [6].

1.2.3.1.7 Borides (MB)

Borides appear in nickel-based, and iron-nickel-based superalloys when there is roughly 0.03% boron present and takes the formula M_3B_2, where "M" represents elements such as molybdenum, tantalum, niobium, nickel, iron, and vanadium. Similar to carbides, borides help add strength to the superalloy; but unlike carbides, carbide etchants do not affected borides [6]. Borides form at the grain boundaries and in small amounts help

increase creep-rupture properties. Borides are half-moon, and blocky shapes that are hard particles that do not appear in the matrix like carbides [6].

1.2.3.1.8 Nitrides (MN)

Nitrides take the cubic crystal structure and form into square/rectangular shapes. Nitrides form when nitrogen reacts with elements such as titanium, niobium, and zirconium [6]. Nitrides are extremely difficult to modify at temperatures below melting [8].

1.2.3.1.9 Mew (μ)

This phase takes the rhombohedral crystal structure and forms at high temperatures into the Widmanstätten pattern [8]. Elements that form this phase are molybdenum or tungsten [6].

1.2.3.1.10 Laves

Laves has hexagonal crystal structure and forms into irregular globs, or plates at high temperature. Laves forms when iron or cobalt react with titanium, niobium, tantalum, or molybdenum [6]. Laves forms at the cost of Ni_3Nb which is detrimental to the strength of the alloy due to the reduction of gamma double prime, the main strengthener of this alloy. The cooling rate of the material also has an effect on the creation of laves phase. If the cooling rate is high, there is less time for the laves phases to accumulate in the microstructure [19].

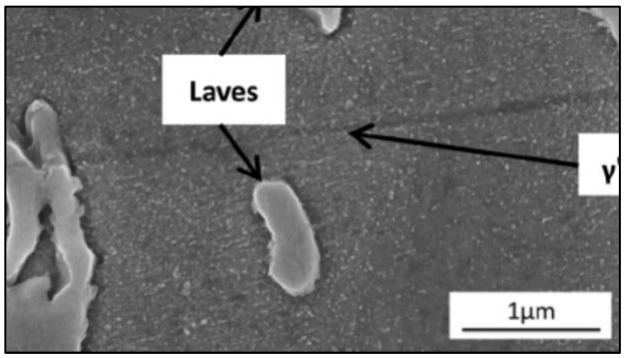

Figure 1.10: Laves Phase present in alloy 718 [12].

1.2.3.1.11 Sigma (σ)

Sigma has a tetragonal crystal structure and similar to laves, sigma forms in irregular globs at high temperature. Sigma forms at 540-980˚ C for extended amounts of time. Sigma and laves phases are not desired in the microstructure because they lower rupture strength and ductility [6]. Phases like laves and sigma can form in needle like shapes at the grain boundaries [9].

Listed were the possible microstructures phases that appear in alloy 718. Some phases are more predominate than others depending on the source or creation. Many phases appear in multiple manufacturing process. Described are all phases that appear in additively manufactured alloy 781. The stresses applied to the alloy during creation have an impact on the microstructure. For additive manufacturing, large amount of stresses appear during the printing prosses. This will have an impact on the microstructure [19]. Next, the focus will be one how these phases contribute to the strengthening of alloy 718.

1.2.3.2 Phase Hardening

1.2.3.2.1 Strengthening Mechanisms

Precipitation hardening and solid solution hardening are the main strengthening mechanisms in alloy 718. Many phases contribute to the precipitation that creates

opportunity for precipitation hardening. During the hardening process, the mismatch of precipitates and matrix must be coherent with a mismatch from zero to one percent [6]. This mismatch aligns the matrix and precipitate with a crystal structure and with similar crystal structure sizes. The order of these crystal structures and atoms also add to the strengthening effect of the metal. The ordering disrupts any dislocations that would move through the crystal adding to the strength. Lastly, the size of the precipitation directly affects the strength. If the precipitations are too small, dislocations are able to bypass them easily making the crack propagation quick. In addition to this, if the precipitates are too large, they create stresses from bowed atom bonds that also lower the strength of the material [6].

1.2.3.2.2 Precipitation strengthening

When a material is under load the deformation that takes place depends on the type of strengthening. Characteristics of precipitate strengthening are a mismatch of one percent between the gamma matrix creating a preferred precipitate. This enables a proper size and style of crystal structure allowing more precipitates in the matrix thus increasing the strength. The preferred ordering is a close packed system of an FCC crystal structure with the precipitates on the face of the structure. This ordering increases the energy needed to move dislocations, which are the main deforming mechanism [6] [8].

Having precipitates with the correct size will increase the strength. Precipitates will do little to affect the dislocation movement if they are too small, and reduce the strength if they are too large. This causes the dislocation to bow which also decreases strength. The optimal size is dependent on the property desired. Creep rupture is increased if the size is uniform, but this is only possible with single crystals and unlikely to be used in many

material applications. Having a single size of gamma prime will decrease the creep rupture while increasing the tensile strength.

More than one element can be present in the crystal structure. When this happens, the element is assigned a location and one example of this could be the secondary phase Ni_3AL. The aluminum will locate to the corners of an FCC crystal structure while the nickel will be located at the faces [6].

1.2.3.2.3 Precipitation Hardening

The small secondary phase homogenously spread throughout the matrix phases is the main strengthener. The small precipitates act as obstructions that limit the dislocation movement. The formation of precipitates undergo age hardening as displayed in Figure 1.11 [8] [20]. To create the precipitates the material needs to follow these steps:

1. Heating the material below the liquidus line but high enough to dissolve the secondary phase will ensure that the precipitates disperse evenly throughout the matrix.
2. Rapidly cooling the material so the atoms lock in place.
3. Heating the material again to allow the precipitates to form clusters. This may take long periods depending on the desired effect.

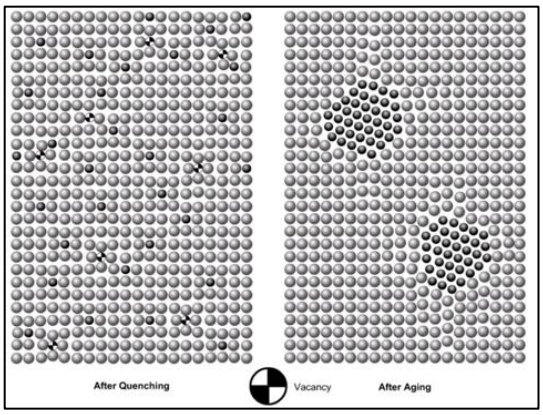

Figure 1.11: Example of Precipitate hardening through the process of age hardening [20].

1.2.3.2.4 Solid Solution Strengthening

Two types of solution strengthening are possible, substitutional and interstitial. An interstitial is a small atom that is able to fit between two normal atoms in the crystal structure. This causes the bonds to stretch in order to fit the new atom, causing stresses in the structure. When substituting, the atom may be larger or smaller than the original atom. This will cause the bond to stretch if it is smaller or compress if it is larger. The stresses added to the structure create localized points of high stress, which makes dislocation movement much harder [8] [20]. Figure 1.12 displays three types of solid solution particles.

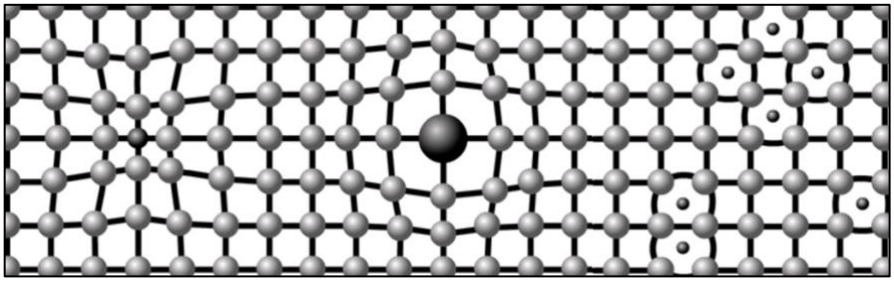

Figure 1.12: Example of Solid Solution Strengthening. Substitution on the left and middle, interstitials on the right [20].

1.2.3.2.5 Influence of grain size

The grain size influences the properties of the crystal structure in a material. Grain boundaries in close proximity usually have different slip planes and orientations. The grain boundary creates a dislocation barrier. Dislocations moving through a crystal will have to alter their direction to accommodate the changing slip planes and orientation of the surrounding grains. This disorder of grain boundaries ensures a stronger material. The smaller the grain size the stronger the material based on the increased orientations and direction a dislocation would have to move. Coarse grains generally have less strength and hardness when compared to smaller grain material [6] [8].

1.3 Defect Detection

1.3.1 History

Additive manufacturing has been advancing rapidly due to its versatile capabilities, and complex designs possible. This surge of 3D printing systems has advanced beyond its monitoring capabilities. When metal additive manufacturing emerged in the 1980s the known defects were porosity, cracking, delamination, etc. [21]. These defects are still present in today's additive manufacturing. The lack of process monitoring is responsible for the remaining defects. For many of the known defects in additive manufacturing there have been studies reflecting work that utilizes techniques to minimize the defects as much as possible, even to the point of elimination [21]. The in-situ monitoring of an additive manufacturing build is the primary focus for process monitoring because this creates the possibility for closed-loop applications. The purpose of closed-loop applications if to identify a defect on the current layer and adjust the parameters or printing process to fix the error. If this is not possible, aborting the print will save time, money, and resources.

1.3.1.1 Defects

An understanding of the possible defects is beneficial when developing systems and proceses that will eventually eliminate these defects. For each defect, there can be a number of different sensors available to monitor the creation of the defect during a 3D build. A review of defect formation, and ways to monitor defects in-situ improves the capturing capability. Defects will fall in one or more of the categories listed. Each category is a preliminary starting point for a defect.

1.3.1.2 Pores

Pores can form in different ways that will alter the size and shape of the pore. The first type of pore forms when trapped gas solidifies within the metal. This can cause pores to form in the 5-20 μm range [21]. Hot Isostatic Pressure (HIP) eliminates the pore in the post processing of the parts. This uses high pressure to annihilate the pores. These pores are difficult to monitor because of the small sizes. High-speed cameras have the capability to track these pores on the current layer and the subsequent layers. The second type of pore forms from a lack of fusion during the melting process. Faster laser speeds or lower power levels create these pores. The size of these pores can range from 50-500 μm depending on the parameters [21]. Possible sensors such as high-speed cameras, thermal cameras, and photodiodes have the capability to detect these defects. In Figure 1.13, there is a representation of the two different types of pores found in AM.

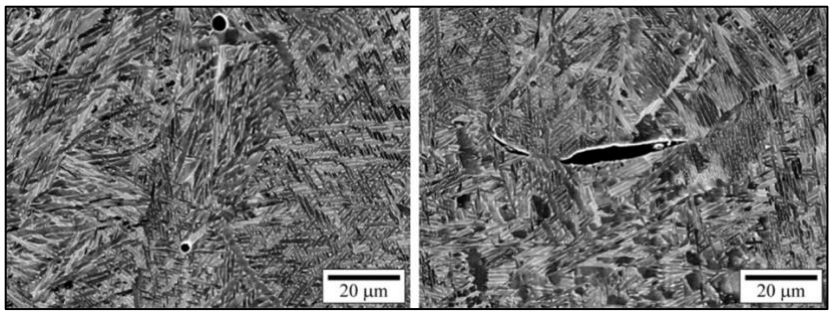

Figure 1.13: Left: Entrapped gas ~5 µm, Right: Lack of fusion ~50 µm [22].

The pores created during the AM process are removable through post processing, as are most of the defects. This is why parameter selection is vital. Many of the smaller pores are removable, however the larger pores are the main problem leading to fatigue and part failure.

1.3.1.3 Balling

The next defect is balling. This defect appears when speed and power are set to high, or when the speed and power is set to low. This happens because the laser has enough energy to melt a large area that causes the surrounding powder particles to attract to the heat source, yet the laser speed is so fast that there is discontinuity of the laser line. Proper parameter selection will eliminate this defect. Optical sensors and photodiodes monitor this effect due to the high intensity of the spherical metal beads left behind. Figure 1.14 shows the balling effect for different parameters.

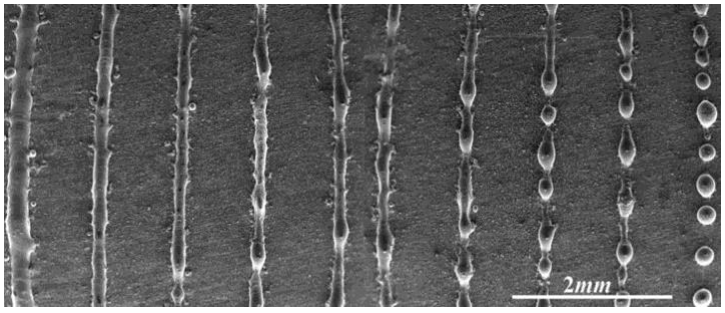

Figure 1.14: Balling effect for different parameters [23].

Proper parameters selection easily eliminates any balling. However, AM proper parameters are not always selected so the ability to detect this defect with the mentioned sensors becomes relevant. While monitoring, opportunities to fix parts mid-build becomes possible.

1.3.1.4 Cracking or Delamination

The last category of defect is cracking. This comes in many different forms such as residual stress, delamination, and post processing errors [21]. Residual stress causes the majority of cracking in parts during AM. Residual stress builds up in each layer from the material wanting to shrink. For parts with a large amount of surface area, the residual stress can be massive due to the large area of metal that is trying to recede to the center. Residual stress is at its maximum close to the build plate and reduces as the part grow higher. Other types of cracking are delamination. This is common when the laser power is low which leads to the melt pool not being large enough to penetrate the previous layer [21]. The last form of cracking is from post processing. Post processing can cause cracks through HIP and heat treating the part. The cracking emerges as a side effect of the defects created mid-build due to poor parameter selection. Types of sensors that are able to capture this cracking in-situ are visible cameras, thermal cameras, and profilometers. In Figure 1.15 residual stress is present that causes the part to crack and to curl away or delaminate from the substrate.

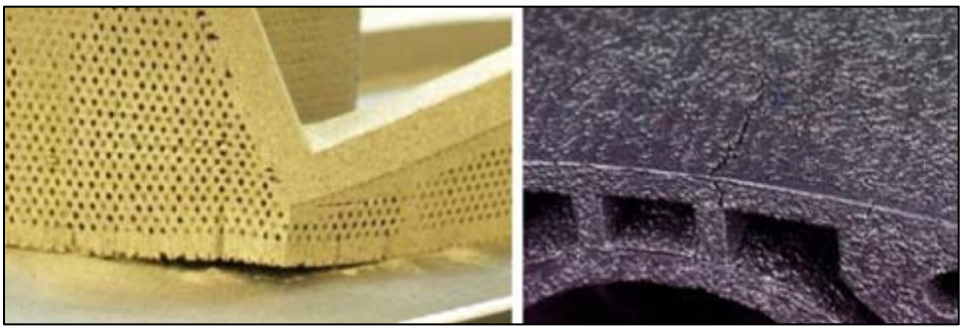

Figure 1.15: Cracking and delamination in an AM part due to residual stress [24].

As stated earlier, these three categories include many of the known defects that appear in AM. These defects result from many of the parts and processes of AM to be lacking much of the process monitoring techniques. By adding different sensors to monitor the process of AM, it will eliminate the need for destructive testing to confirm that a part is indeed defect-free. By evaluating previous work on process monitoring, it is possible to use the correct sensors to evaluate a build in real time.

1.4 Previous Work

1.4.1 Alloy 718

In AM, variability that can affect the microstructure of the as-build part. During the process of Laser Powder Bed Fusion (LPBF), many parameters can have an effect on the overall microstructure. As discussed previously, the phases that contribute to the strength of alloy 718 depend on time and temperature. In LPBF, the melt times are incredibly small which leads to extremely fast solidification of molten metal. This fast solidification alters the microstructure making it different from traditional means such as cast or forging. Other ways that LPBF process effects the microstructure is through laser scan strategy, and energy density. These two processes are similar in that the scan strategy can change the energy density. The scan strategy is the path that the laser will take to melt each layer.

Changing the speed, width, design, direction etc. will have a lasting effect on the part quality. The strategy used to melt a LPBF part has an effect on the microstructure. The energy density depends on the hatch spacing, layer thickness, speed, and laser power. An increase in laser power and a decrease in laser speed would result in an increase in energy density. A decrease in laser power and an increase laser speed would results in a decrease of energy density. The next factor that affects the microstructure is the post processing. This can be heat treatment, Hot Isostatic Pressure (HIP), age hardening etc.

1.4.1.1 Energy Density

One of the main reasons why LPBF results in a slightly altered microstructure when compared to cast or forging is because of the complex nature of a laser beam. This nature creates a non-equilibrium between the chemical reactions in the material [25]. Energy Density is the power of the laser divided by the speed of the laser, hatch spacing, and layer thickness. With the energy density being very low, the metal powder absorbs enough energy to melt partially. This creates the balling effect, where there is a discontinuous line of melted metal. Figure 1.16 shows the increase in energy density can have an effect on the microstructure.

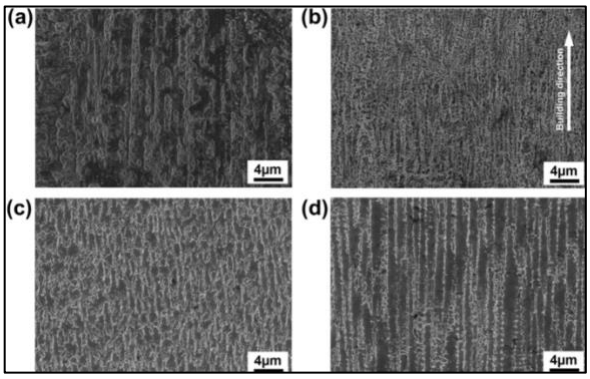

Figure 1.16: Microstructure based on energy density. A) 110W, 600mm/s B) 110W, 400mm/s C) 120W 400mm/s D) 130W 400mm/s [25].

In Figure 1.16 it is clear that an increase in energy density affects microstructure. In A and B, there is a difference in scanning speed, but the power remains the same. With a faster scan speed there is less time spent in one spot leading to faster heat dissipation. This heat dissipation is responsible for change the microstructure [25]. In the remaining tiles, the powder is the only changing parameter. With an increase in powder and no change in scan speed, results in a larger melt pool and longer solidification times. A longer solidification time means that the molten metal has a longer amount of time to solidify, leading to larger dendritic growth perpendicular to the build direction. As the energy density increases the microstructure changes in the order of coarse columnar dendrites, clustered dendrites, to slender and uniform dendrites [25].

Similarly, the direction of the scan strategy has an effect on microstructure. In a simple study of a single direction and a cross-direction scan strategy, it was shown that depending on the laser scanning style, the grain size changes. The grain size has a major effect on the mechanical properties of the material. In the single direction scan strategy, the grain size appeared to be less uniform when compared to the cross directional strategy. This change in grain size can alter the ductility of the part, although it does not affect the ultimate yield strength [26].

Another way to control the outcome of metal additive manufacturing is by changing the design of the laser scan strategy. As previously noted, there are many different designs possible, such as lines, stripes, contours, island, circle, cross, etc. Of these designs, an evaluation of the island strategy and its effect on microstructure and mechanical properties is shown. The island strategy creates small squares where the laser will melt the metal, and

to eliminate stress the squares are melted in a random order. An example of the island strategy is in Figure 1.17.

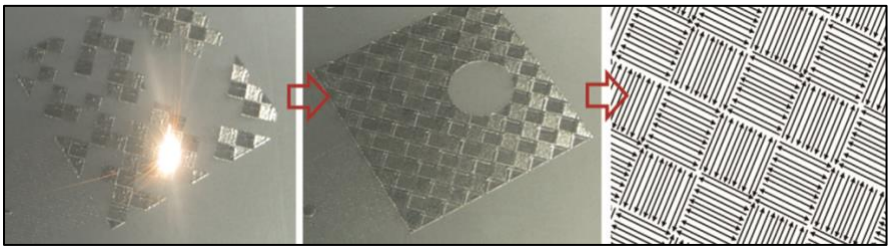

Figure 1.17: Example of Island laser scan strategy [27].

Similar to the single and cross direction laser strategy experiment, the island scan strategy also has an effect on the microstructure. In the experiment, different island sizes created specimens for material analysis and mechanical testing. The study shows that although there are density differences between the specimens, the ultimate tensile strength stayed relatively the same [27]. The results also show that based on the experiment of four different specimens, (2 x 2 mm, 3 x 3 mm, 5 x 5 mm, and 7 x 7 mm;), the 5 x 5 mm, and 7 x 7 mm specimens have the lowest residual stress [27]. The 2 x 2 mm specimen had the lowest recorded residual stress but this is only because the specimen had cracking throughout. This experiment suggests that based on the scan strategy, an optimal design for the laser scan strategy exists depending on the specimen's purpose.

1.4.1.2 Residual Stress

Residual stress is a difficult problem to consider with additively manufactured parts because of the many different parameters to consider. As previously stated, the parameters selected for a part or experiments affect the melt pool. Various forces and chemical reactions affect the melt pool. The laser melt pool is also extremely small leading to rapid melting and solidification continuously for the duration of the build. This rapid melting

and solidifying leads to high residual stress in a part. The common microstructure for alloy 718 in LPBF is columnar dendrites growing perpendicular to the build direction [28]. This microstructure growth will eventually evolve into uneven grains solidifying at elevated temperatures. The microstructure of a printed part shows signs of residual stress because of the melting process. Residual stress is relatively low during a long single laser line pass and grows as the time between passes increases and in areas of many overlapping layers [28]. The residual stress for high overlapping areas creates uneven grains in the microstructure [28]. Based on the orientation the residual stress appears in the build direction similar to the microstructure growth [29]. Therefore, by controlling residual stress in a manageable way, the microstructure and part health overall can improve. Various post processing procedures exist to eliminate residual stress, such as heat treatment, hot isostatic pressure (HIP), etc.

Heat treatment is one of the many forms used to alleviate some of the high stress points in a LPBF printed part. Depending on the elemental make-up of the metal powder, alloy 718 can be susceptible to high niobium and molybdenum, which, combined with the fast cooling rates of LPBF result in the formation of laves phases. Previously mentioned, laves phase is detrimental to the strength of alloy 718 and should be modified. Heat treatment offers a solution by placing the specimen in an oven at elevated temperatures, approximately 1100˚ C, for a known amount of time so that the laves phase can dissolve back into the microstructure removing the detrimental phase. During this process the grains sizes will not alter significantly due to the carbides present at the grain boundary, prohibiting their movement [30]. The heat treatment process eliminates the laves phase and

returns the strength of alloy 718 to the point where the tensile strength, yield strength, and hardness values all are slightly better than wrought material [30].

A similar study showed that the uneven grain structure that corresponds to the as-built alloy 718 specimens can be a result from the competitive nature of the dendritic arms in the overlapping melt pools. The cooling rate cannot be calculated by measuring the size of the dendritic structures, instead the cooling rate should be compared to other 718 welds for a more accurate measurement [31]. One drawback of heat treatment depends on the treatment type. Some heat treatments can eliminate laves phase but simultaneously creating the needle like delta phases. This can be beneficial in some aspects but as the delta phase becomes more prominent it will start to have negative effects [32].

The microstructure of alloy 718 has many phases that lead to complex analysis of the process parameters for LPBD AM. With detailed experiments, the microstructure can be optimally produced and with post-process heat treatment, the mechanical properties can resemble wrought and cast alloy 718, if not better. Of the experiments listed, many used destructive tests in order to gain an insight into the microstructure of the printed part. Due to this need for destructive testing it is essential that monitoring capabilities be created to eliminate wasted time and resources. Process monitoring is a common way of monitoring a build to record information that can eliminate the need for destructive testing.

1.4.2 Process Monitoring

The main cause for defects in AM is sub optimal parameter selection. Numerous variables contribute to the creation of defects, and many can vary from day to day. Most of the variables are consistent with the laser capabilities and the powder selected. Other variables emerge from the way powder is stored and the rate it is used. All of these, and

many more, affect the quality of an AM build. Table 1 lists all the possible ways a defect can emerge.

	Parameter	Description	Controlled or predefined
Laser and scanning parameters			
1.	Average power (P_l)	Measure of total energy output of a laser	Controlled
2.	Mode	Continuous wave or pulsed	Predefined
3.	Peak power (P_{peak})	Maximum power in a laser pulse	Predefined
4.	Pulse width (PW)	Length of a laser pulse when operating in pulsed mode	Predefined
5.	Frequency (f)	Pulses per unit time	Predefined
6.	Wavelength (λ)	Distance between crests in laser electromagnetic waves	Predefined
7.	Polarization	Orientation of electromagnetic waves in laser beam	Predefined
8.	Beam quality (M^2)	Related to intensity profile and used to predict how well beam can be focused and determine minimum theoretical spot size (equal to 1 for a Gaussian) [18]	Predefined
9.	Intensity profile I (x,y,t)	Determines how much energy added at a specific location	Predefined
10.	Spot size (d_x and d_y)	Length and width of elliptical spot (equal for circular spots)	Controlled
11.	Scan velocity (v)	Velocity at which laser moves across build surface	Controlled
12.	Scan spacing (S_s)	Distance between neighboring laser passes	Controlled
13.[a]	Scan strategy	Pattern in which the laser is scanned across the build surface (hatches, zig-zags, spirals, etc.) and associated parameters	Controlled
Powder material properties			
14.	Bulk density (ρ_b)	Material density, limits maximum density of final component	Predefined
15.	Thermal conductivity (k_b)	Measure of material's ability to conduct heat	Predefined
16.	Heat capacity ($c_{p,b}$)	Measure of energy required to raise the temperature of the material	Predefined
17.	Latent heat of fusion (L_f)	Energy required for solid-liquid and liquid-solid phase change	Predefined
18	Melting temperature (T_m)	Temperature at which material melts; for alloys the difference between the liquidus and solidus temperature is typically of greater interest	Predefined
19.	Boiling temperature (T_b)	Temperature at which material vaporizes; may only be important in certain process conditions	Predefined
20.	Melt pool viscosity (μ)	Measure of resistance of melt to flow	Predefined
21.	Coefficient of thermal expansion (α)	Measure of volume change of material on heating or cooling	Predefined
22.	Surface free energy (γ_{sl})	Free energy required to form new unit area of solid-liquid interfacial surface	Predefined
23.	Vapor pressure (p_v)	Measure of the tendency of material to vaporize	Predefined
24.	Heat (enthalpy) of reaction (H_r)	Energy associated with a chemical reaction of the material (e.g., oxide formation), not always relevant	Predefined
25.	Material absorptivity ($A_{b,m}$)	Measure of laser energy absorbed by the material, as opposed to that which is transmitted or reflected	Predefined
26.	Diffusivity (D)	Important for solid state sintering, not as critical for melting	Predefined
27.	Solubility (S)	Solubility of solid material in liquid melt, unlikely to be significant	Predefined
28.[a]	Particle morphology (A_R, f_{circ}, f_{elong}, etc.)	Measures of shape of individual particles and their distributions, e.g., aspect ratio, circularity, and elongation	Predefined
29.	Surface roughness (R_A)	Arithmetic mean of the surface profile	Predefined
30.	Particle size distribution	Distribution of particle sizes, usually diameter, is a powder sample	Predefined
31.[a]	Pollution	Ill-defined factor describing change in properties of powder due to reuse as dust and other particles added to powder	Predefined

Table 1: Possible variables that can contribute to defect creation [33].

Powder bed properties and recoat parameters			
32.	Density (ρ_p)	Measure of packing density of powder particles, influence heat balance	Predefined
33.	Thermal conductivity (k_p)	Measure of powder bed's ability to conduct heat	Predefined
34.	Heat capacity ($c_{p,p}$)	Measure of energy required to raise the temperature of the powder bed	Predefined
35.	Absorptivity (A_p)	Measure of laser energy absorbed, dependent on A_b and state of powder bed	Predefined
36.	Emissivity (ϵ)	Ratio of energy radiated to that of black body.	Predefined
37.[a]	Deposition system parameters	Recoater velocity, pressure, recoater type, dosing [30]	Controlled
38.	Layer thickness (L)	Height of a single powder layer, limiting resolution and impacting process speed	Controlled
39.	Powder bed temperature (T_p)	Bulk temperature of the powder bed	Controlled
Build environment parameters			
40.	Shield Gas	Usually Ar or N_2, but may also be He, or something else	Predefined
41.	Oxygen level ($\%O_2$)	Probably most important environmental parameter; oxygen can lead to oxide formation in metal, change wettability, energy required for welding	Controlled
42.	Shield gas molecular weight (MW_g)	Influences heat balance, diffusivity into and out of part	Predefined
43.	Shield gas viscosity (μ_g)	May influence free surface activity of melt pool, convective heat balance	Predefined
44.	Thermal conductivity ($k_{c,g}$)	Term in heat balance	Predefined
45.	Heat capacity of gas ($C_{p,g}$)	Term in heat balance	Predefined
46.	Pressure (p)	Influence vaporization of metal as well as oxygen content	Controlled
47.	Gas flow velocity (v_g)	Influences convective cooling, removal of condensate	Controlled
48.	Convective heat transfer coefficient (h_c)	Convective cooling of just melted part by gas flowing over the surface	Predefined
49.	Ambient temperature (T_∞)	Appears in heat balance, may impact powder preheat and residual stress	Controlled
50.	Surface free energy (γ_{gl})	Between liquid and surround gas influence melt pool shape	Predefined

Table 2: Continuation of Table 1 [33].

Table 1 and 2 display many of the mentioned variables that contribute to the formation of defects. It is important to note that even though the variables are controllable there is a possibility that they can still induce defects [33].

1.4.2.1 Sensors

Due to the large number of defects that can cause a failed AM build, it is necessary to monitor these builds with multiple sensors to eliminate defect formation as much as possible. Typical sensors that are used for defect detection can vary for each different AM process, LPBF sensors will be the focus. The typical sensors that used in LPBF are optical, visible, acoustic, pyrometers, infrared cameras, photodiodes, and spectrometers. Many of these sensors have the capability to collect data on more than one defect type. Some of the sensors focus on the melt pool while others focus on the entire build area, or just the melt plume [34]. The three main types of sensors that will be focus on are the visible and thermal cameras, high-speed cameras, and photodiodes. Each sensor will have its own research and examination.

1.4.2.1.1 Visible Camera

The visible camera definition is straightforward. One or more cameras use light in the visible spectrum to illuminate a part in-situ. This likely will reveal possible defects in the powder before the laser strikes, and it can show defects in the part after the laser has melted the current layer. This is the most used type of sensors due to its ease of use and ability to collect pre and post images of a layer. In Figure 1.18, visible images detect defects throughout the part layer-by-layer. This give a fully encompassing visual of where the defects are and how they affect the part.

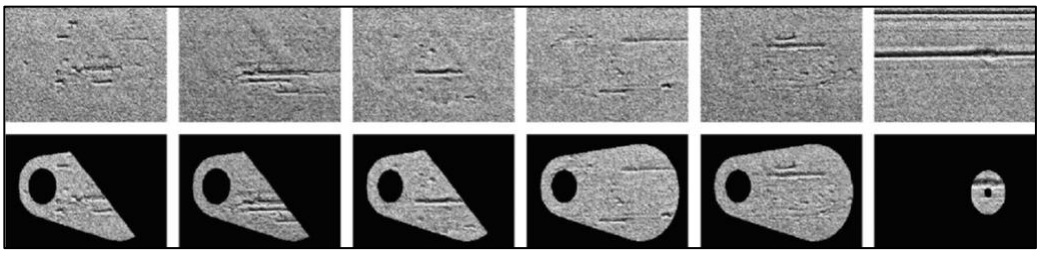

Figure 1.18: Top row: before imaged taken of the powder. Lower row: powder anomalies [35].

Collecting data each layer, and using a software to accumulate all the defect locations creates a map of the full part for evaluation. Figure 1.19 shows the full part with every defect found throughout the layer-by-layer process.

Figure 1.19: Defect map showing every defect captured earlier in the build [35].

This encompassing view gives insight for proper post treatment and possible failure points. A similar approach to defect detection through optical imaging uses inline coherent imaging position coaxial with the laser beam. This approach allows identification of the melt pool. Being able to identify the melt pool and its geometry, and then verifying with visible camera data, increases the possibility of identifying defects and part abnormalities. Figure 1.20 compares the inline imager to the visible data.

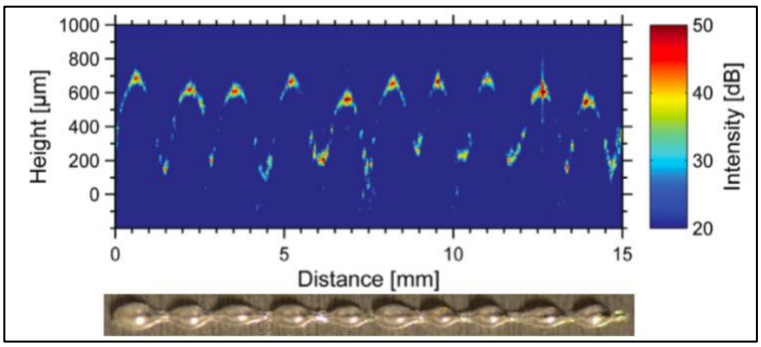

Figure 1.20: Inline coherent image with visible camera data [36].

Defect identification increases using this method due to the high reactivity the imagery can used based on process parameters and substrate wetting [36]. Many of the data taken is for single line. This is because it is necessary to learn how to analyze data based off a single laser line to understand the fundamental physics that are taking place. Understanding basic laser behavior will be critical for understanding the processes of an entire part with multiple line and multiple layers. Similar sensors that collect slightly different information on the melt pool are infrared cameras.

1.4.2.1.2 Infrared Camera

Infrared cameras are similar to visible cameras with one main difference. The spectrum of light changes for a visible camera and for an infrared camera. A visible camera will focus on light in the 380 – 780 nm wavelength range while an infrared camera will focus on light from the edge of the red visible light, 700nm to 1 mm. In this range, temperature can be monitored due to the radiation that thermal wave gives off. Using this information can shed light on many different melt pool behaviors. The melt pool is strictly responsible for the formation of molten metal and the solidification of the microstructure. The types of defects detected with a thermal camera are lack of fusion, key holing, bulging, etc. Figure 1.21 shows examples of environmental effects on IR camera images.

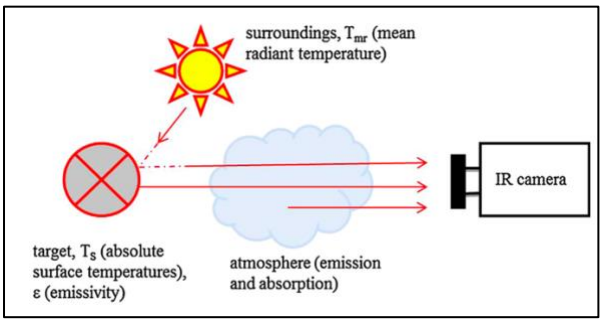

Figure 1.21: Types of radiation captured by infrared cameras [37].

Figure 1.21 shows the types of radiation the infrared (IR) camera can receive. The radiations included the emission and absorption from the surroundings, the object of interest, and the surrounding temperature. All of these sources can add to the signal received from the target. Other signals received are not beneficial. These include the emissivity of the target, the atmosphere, and any reflective surface in the proximity of the sensor's view [37].

Due to the many influences surrounding an IR camera, it is important to create a system that will eliminate these interferences and collect unaltered data of the target. By calibrating the IR camera for high temperatures, interferences do not affect the accuracy. Calibrating the IR cameras via blackbody radiation ensures a steady baseline to compare results later. A black body is a known heat source with an emissivity of 0.99 [37]. For the calibration, it is imperative to have the set-up be as close to the desired experiment. For example, due to the rough environment that LPBF has, the sensors reside outside of the box containing the system. For this reason, special glass replaces the normal viewing window for better signal. These windows are included during the calibration for a proper baseline.

IR cameras are useful for identifying the temperature of a build in-situ. However, there are factors that interfere with the signal. The first is that the emissivity of the target effects the analysis of the melt pool. This is difficult due to the evolving nature of the melt pool. The emissivity of molten metal changes, therefore an exact number for the emissivity of a LPBF part in-situ is unknown. Extensive experiments and comparative testing to find average emissivity eliminates the problem. The next problem with IR cameras is the resolution of the lenses. LPBF has microscopic melt pools that can cause inaccurate readings when compared to the background temperature. With a melt pool in the range of 20-100 µm, the resolution on a camera needs to be precise. If the size is not considered, then the calculation for thermal temperature will be inaccurate due to the averaging of pixels in a microscopic scale. Increasing camera resolution helps to resolve this problem, but also increase the camera's cost. When the camera captures a layer's thermal behavior, a map of the part displaying the thermal gradients throughout the layer appears. Over multiple layers, the thermal behavior can be consistent based on defect behavior and part surface roughness. Figure 1.22 displays the multi-layer capture of the thermal gradients.

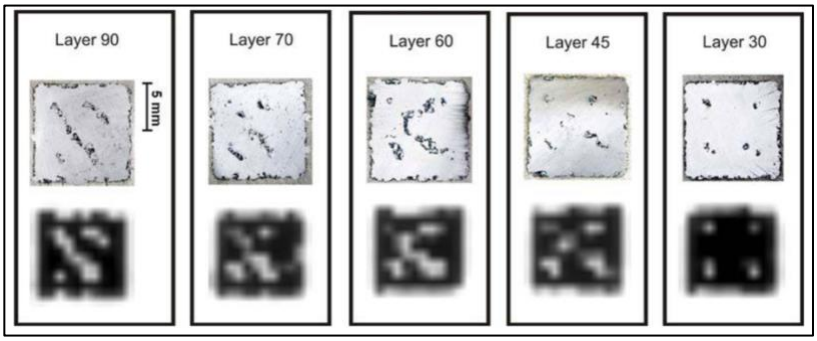

Figure 1.22: IR images taken at different layers showing thermal activity [38].

The goal of thermal imagery is to allow the part to be repairable during a build. Detecting a defect early in a build will reduce the time needed to find the defects in post

processing and will eliminate builds due to defects for increased productivity. In this research, the IR camera is able to identify the layers with flaws. Powder covers layers containing flaws for the next layer, which produces an overly large layer for the part. This creates a transition of flaws from one layer to the next. IR cameras eliminate this defect by detecting it early and repairing the part [38].

Another major issue with AM parts is the porosity level based on the parts geometry and parameter selection. Due to the complexity of parts created via AM, it is inevitable that many parts have large overhangs. This is one of the leading causes of porosity. Overhangs appear with the same parameters as the bulk parts. This creates issues when the goal of the bulk is to melt into the previous layer. When creating an overhang, the melt pool is penetrating into the previous layer where there is not previously melted metal underneath. This causes the laser to over penetrate and melt powder particles that are unsupported, causing nonuniform part edges and porosity. One way to detect these is with IR cameras. By monitoring the reflected light, IR cameras collect the porosity in overhanging structures. Figure 1.23 shows the change in porosity as layer height and overhang depth changes.

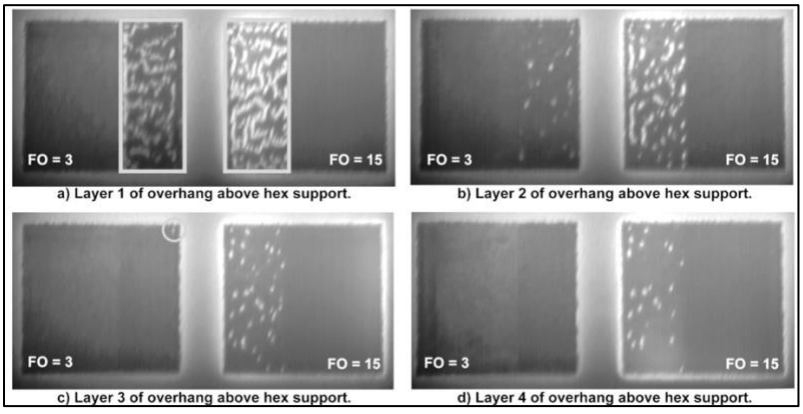

Figure 1.23: Porosity imagery for IR camera for overhang structures [39].

IR cameras are able to evaluate the microstructure of an AM part by tracking the thermal history. By comparing different scan strategies to change the thermal history, different microstructures appear. A typical line scan strategy creates columnar dendrites that grow epitaxially. Comparing this to the point melt scan strategy, which creates isotropic properties, this eliminates grain boundaries producing a stronger part in the build direction. The IR camera is also able to detect defects based on the emissivity of the surface. As the emissivity changes the IR signal changes as well. Powder being porous will have an emissivity of 0.68. As this surface changes to melted material and then to a solidified part, the emissivity with change to 0.37 at 800˚ C and 0.46 at 1275˚ C. This distinction in emissivity makes IR cameras capable of detecting defects. Figure 1.24 illustrates how the change in emissivity affects the IR camera image [40].

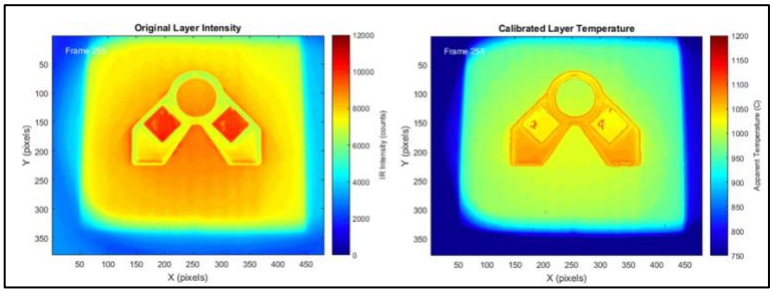

Figure 1.24: Right: the IR output for the first few layers. Left: the final IR output [40].

As the AM build continues, the temperature will naturally rise. Figure 1.24 displays the change in thermal gradient throughout the part. The point scan-strategy results in a cool build, as one point begins to cool other areas melt. The line scan-strategy results in larger thermal gradients, including areas where the line strategy increases the temperate of the point scan-strategy. Due to the lower temperature of the point scan-strategy, the thermal gradient decreases, resulting in the equiaxed microstructure. This ensure the microstructure

grows in all directions resulting in better mechanical properties [40]. Figure 1.25 shows a comparison of these strategies.

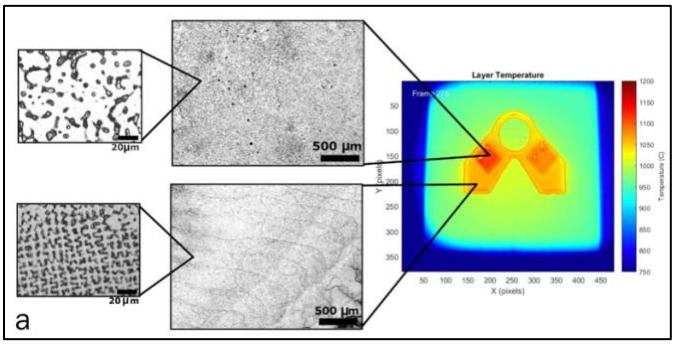

Figure 1.25: Different scan strategies result in different microstructure. Hotter temperatures result from line scan strategy while cooler temperatures from point scan strategy [40].

The productivity of IR cameras is useful in detecting defects as well as predicting the microstructure of the AM part. This does however have its limits. Due to the exposure time and the time required to accurately save and load data files, the IR camera often does not capture the entire surface area of a layer or cannot capture every single layer. This is a result of the resolution needed to capture good data. As the resolution increases, the data files increase proportionally. This hinders the ability to capture all of the necessary data. An investigation of the proper temporal and special resolution that is needed concerning the data file sizes and information acquired is given in [40].

Another attribute that the IR cameras are capable of monitoring is the melt pool behavior. This parameter is indicative of the laser power and speed. The speed is a parameter that might seem to have a large effect on the melt pool length and thus the temperature; however, the speed may have less of an effect on the melt pool behavior as does laser power. A study comparing the change in laser speed and the analysis of the melt

pool through IR camera imagery shows that the speed has little effect on the melt pool length. With an increase in laser speed and a consistent laser power, the melt pools remain similar. The length does, however, increase slightly with the slower speeds. This can be the response to high energy density leading to larger melt pools in general. This monitoring of melt pool behavior sheds light on the laser behavior based on parameter selection. Figure 1.26 compares the change in speed with the melt pool length [41].

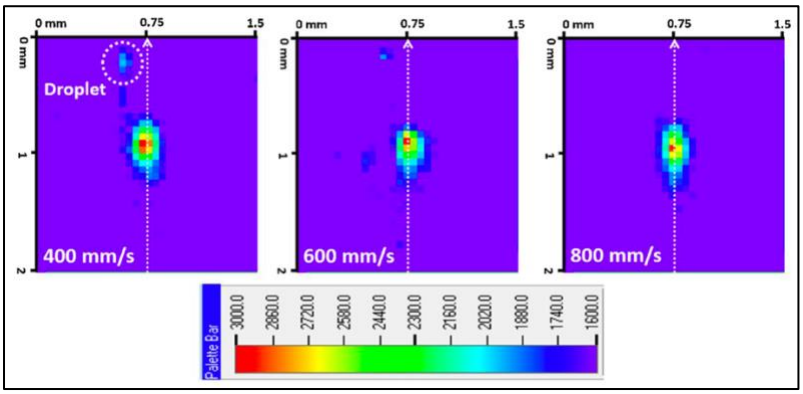

Figure 1.26: Melt pool length monitoring with IR camera. Changes in speed have little effect on the melt pool lengths [41].

One of the reasons the slower laser speed can increase the melt pool length is due to the response of the cameras having an effect on the frame rate. As the speed increases, the width of the melt pool does decrease. The decreasing width is understandable due to the effect of powder on the heated melt pool. With higher speeds, a wider melt pool is not sustainable. Using an IR camera to monitor the melt pool, the probability of monitoring defects in and AM build increases [41].

1.4.2.1.3 Spectroscopy

Spectroscopy is a sensor that also uses photons to collect signals and evaluate the AM build in-situ. Spectroscopy differs from visible and IR cameras in that it focuses on

the species of photon instead of the light reflecting or absorbing from the target. This changes many calculations and the defects that the sensor monitors through spectral response. The Methods section explores the physics and background of the spectrometer. Figure 1.27 displays a typical signal, which is the primary factor that allows defect detection.

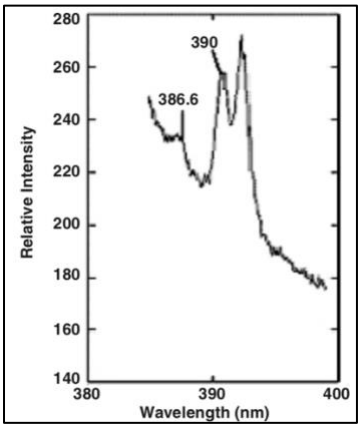

Figure 1.27: Spectroscopy signal for aluminum [42].

Figure 1.27 shows the relative intensity for an aluminum part in AM. The relative intensities are conditions for the surroundings of the experiment. As time, distance, geometry, and power change the signal will fluctuate. The fluctuation in variables is present in the relative intensity of the aluminum part. This sensor is able to collect sensitive data based on the environment of the AM build. When the intensity is collected, numerous calculations about electron temperature are enabled, thus verifying the build parameters and defect creation [42].

Due to the sensitivity of the spectroscopy sensor, an understanding of laser behavior is necessary. The pulse lasers that are used for LPBF have a periodic nature with a set magnitude. The pulse of the laser is represented as a square wave; however, there is a small

amount of ramping that happens when the laser is turned on. Figure 1.28 displays the ramping that occurs when the laser pulses.

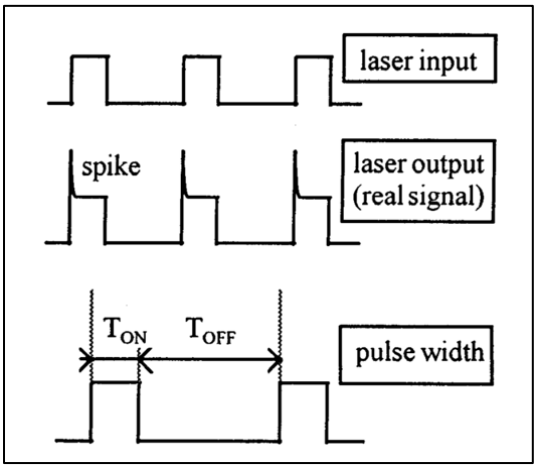

Figure 1.28: Illustration of pulse laser behavior [43].

The change in signal seen in Figure 1.28 is an indication of laser complexity and is an example of how the relative intensity collected by the spectrometer is affected. Laser behavior affects the relative intensity of the spectrometer; however, the spectrometers ability to collect electron temperature does not change.

The main use of spectroscopy is for weld quality. With AM being a collection of many single weld beads that form a more complex part, understanding the nature and behavior of a weld bead with spectroscopy is crucial. Spectroscopy is sensitive enough to allow the visible confirmation that there is a defect in the part based on many factors such as weld defect, shielding gas flow rate, fluctuation, layer anomalies, and spreader defects [44]. Figure 1.29 shows the possible signal feedback spectroscopy can give for weld defects in AM.

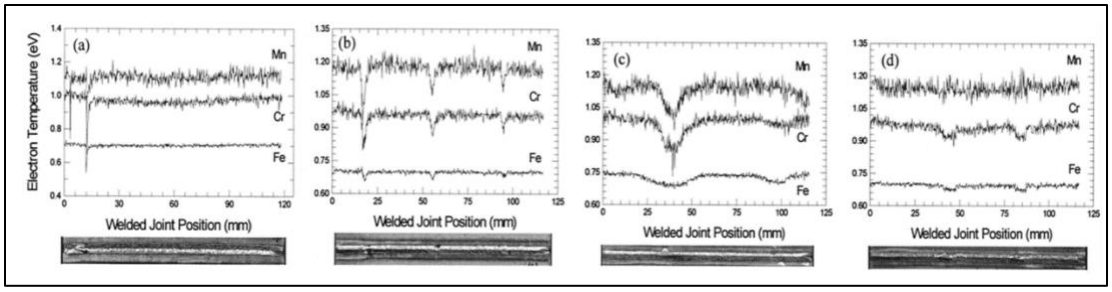

Figure 1.29: Different signals for different defects in laser welds [44].

Taking this data and developing statistical analysis for defects detection, concerning location, geometry, or parameter selection will allow for close loop application. A system that can run fully automated and will detect defects and understand if parts need repair or otherwise be scraped, would have an impact on the AM field. Figure 1.30 displays the analysis tool and confidence interval used to determine defects. A confidence interval conducted for various experiments shows the possibility for closed loop applications [45].

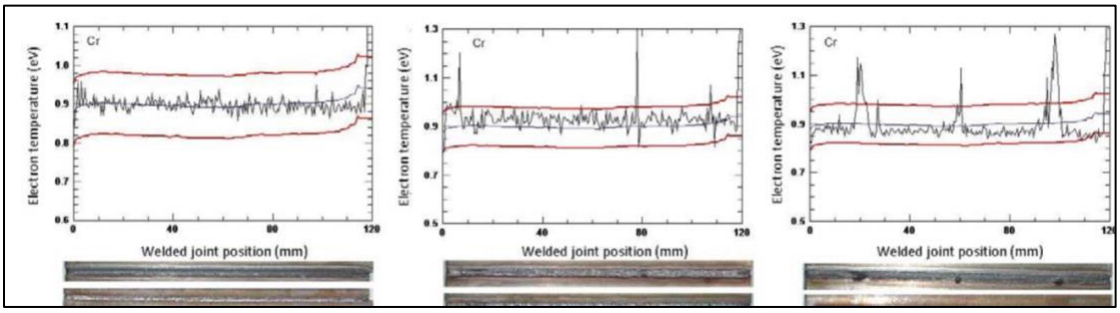

Figure 1.30: Confidence interval for weld defects [45].

A similar and more mathematical approach to spectroscopy is the line-to-continuum. As a way to monitor lack of fusion in parts, spectroscopy evaluates the gas that is in an excited state above the melt pool. This excited gas reveals special species of wavelengths, allowing material characterization. This excited gas can be influenced by many variables. The most influential are the molecular make-up of the material, the concentration of the material, the thickness of the optical plume, and the electrons [46].

One important contribution regarding the laser power and the effects on the plume is counter intuitive. As the laser power decreases, the electron temperature and penetration depth both increase [47]. Physically this is true, due to higher energy into the system the electron temperature absolutely will increase and thus the penetration depth. However, as the spectrometer collects data, and because of the high laser powder, the plume will seep into to melt pool causing the capillary effect during high laser power. The capillary effect causes the hotter potion of the plume to sink into the part while the spectrometer collects data on the colder outer shell of the plume [47]. Figure 1.31 illustrates this phenomenon.

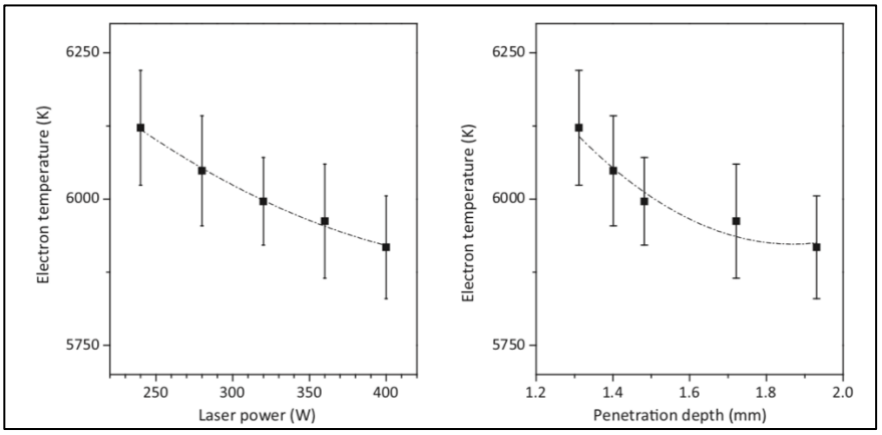

Figure 1.31: Left: laser power with respect to election temperature. Right: Penetration depth with respect to electron temperature [47].

This experiment verifies that high laser power and low penetration depth is conducive in both static, and dynamic environments. The spectrometer was located perpendicular to the laser path for this experiment. This ensures that the melt pool was not interfering with the signal.

The effect of the melt pool has an impact on the part quality. When compared to other methods the penetration and area of effect for laser AM is drastic. In Figure 1.32,

there is an example of the impact lasers have on the penetration depth compared to arch welding.

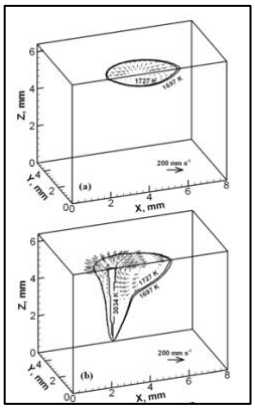

Figure 1.32: Top: Melt pool and penetration for arch welding. Bottom: Melt pool and penetration for Laser welding [48].

This penetration depth is what causes the plasma plume to sink into the cavity during high power welding. Figure 1.32 is also an example of a keyhole melt pool. Depending on the location of the laser this oversizing of the melt pool will affect many variables such as the overhang angle, width of melt pool, laser accuracy etc. taking this information into consideration for material applications is essential. Figure 1.33, provides cross section measurements of the melt pools illustrated in Figure 1.32.

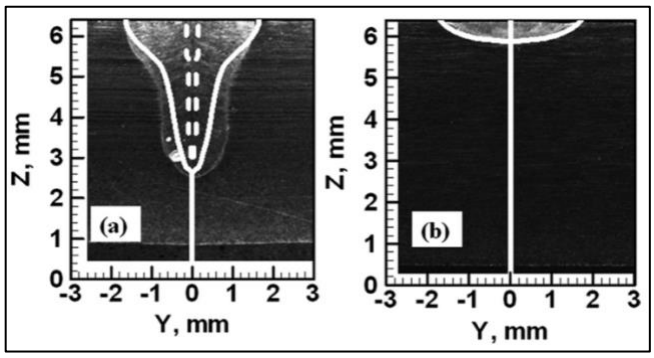

Figure 1.33: Cross section of melt pool. Left: Laser keyhole melt pool penetration. Right: Arch welding melt pool penetration [48].

The penetration seen in Figure 1.33 on the left shows the penetration power of the laser. This penetration pierces more than one layer, which gives the 3D printed part the strength between layers that is needed. Over penetration however can lead to keyholes and swelling of the part. This will reduce accuracy at an increasing rate depending on the part size [48].

Combining these two methods, arch and laser welding, to create a hybrid welding system can create a much larger melt pool due to the added heat and farther penetration. This is useful for larger parts and industrial application [48]. However, this hybrid approach would be detrimental to the laser welding process because LPBF utilizes small melt pools for accuracy in part dimensions and high complexity of parts.

Finally, after articulating the benefits of sensor usages, it is optimal to combine many sensors to form a more comprehensive view for all defects that can arise from the LPBF AM process. The photodiodes are able to collect the light emitted from the target and create a signal representing the melt pool area. This gives an indication of the temperature of the melt pool. A lager area represents a larger signal collected by the photodiodes [49]. Also included are the visible and thermal cameras. These give an estimation of the melt pool geometry and temperature. By comparing the sensors and using them in a computer algorithm, a digital representation of the melt pool effect on the part can be displayed. In Figure 1.34 computerized melt pool imagery determines defects in LPBF build.

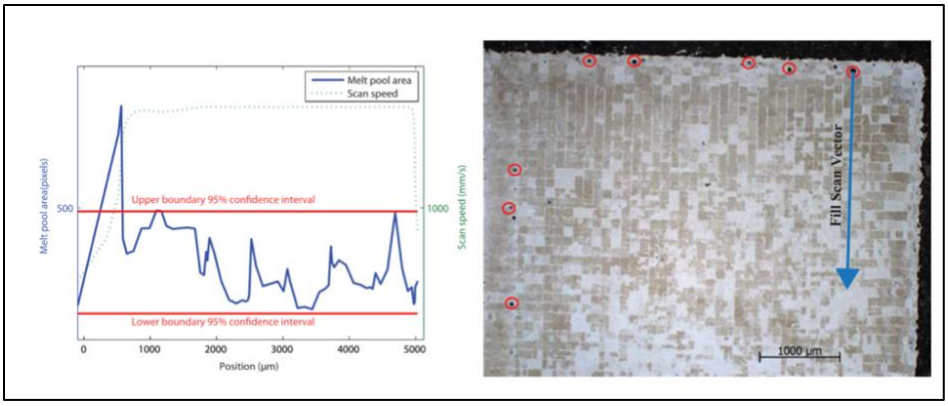

Figure 1.34: Left: Confidence interval for melt pool area. Right: Computerized scan of the photodiode and thermal camera data aligned by position [49].

Figure 1.34 shows on the left the confidence interval used to determine if the melt pool is outside an ordinary intensity. This reflects a larger melt pool size for that instance in time. Larger melt pools indicate larger thermal behaviors in the part and could create defects. By monitoring the melt pool behavior, localized defects can be identified based on the laser behavior and the sensors response to that behavior.

1.5 Summary and Contributions

Many different sensors can monitor defects in a LPBF AM build. Based on the sensor the defect that can be identified changes. Three sensor types will be the focus of this work. Visible cameras are versatile and relatively cheap. Visible cameras evaluate the melt pool geometry. The melt pool geometry provides information on the surface roughness of the part. When the geometry of the melt pool changes abruptly, this indicates a thicker or thinner layer of powder, or a raised defect on the surface. The thermal cameras are valuable in that they can detect the temperature of the melt pool. Knowing the melt pool temperature is valuable to determine the correct laser behavior and indicate laser power. The thermal camera also sheds light on the behavior of the

microstructure. Larger temperature indicates high power and larger microstructure solidification. Finally, the photodiodes are sensors that collect the emitted species of the melted metal, alloy 718. Determining the type of metal that is melting and evaporating in the plasma plume gives useful data on the melt pool area and the penetration depth. The relative intensities that the photodiodes collect can also have implications on the microstructure. As the melt pool area increases or the intensity decreases, this indicates a change in the laser power thus having an effect on the microstructure. By using all three sensors in unison, a large comprehensive view of the LPBF process, and defect identification becomes possible.

1.6 Thesis Contributions

In this research, a multi-sensor approach is used to determine the influence of part geometry and the effect on microstructure development of alloy 718. The contributions are as follows:

1. Determined the effect geometry has on thermal conditions using multi-sensor in-situ monitoring.
2. Identified the effects of processing parameters and geometry on alloy 718 microstructure and melt pool geometry.
3. Experimentally identified the effects of thermal conditions in alloy 718 microstructure and melt pools.
4. Validated a 3-color spectroscopy approach through multi-sensor experimental comparison.
5. Identified the laser plume orientation via 3-color spectroscopy.

Chapter 2: Methods

2.1 Multi-Sensor Approach

Use of AM increased rapidly due to its versatile capabilities and potential for complex part geometries. These geometries are only possible through AM because of the layer-by-layer process building the part at the same time as the material. The layer-by-layer process, however, has inconsistencies that are possible. These inconsistencies are a result from the changing melt pool behavior due to process parameters on each layer, which creates defects periodically in the build as it continues. A high level of confidence in part quality is required to determine if parts are viable for functional applications. Increased confidence comes from material characterization and destructive testing of specimens built parallel to the working part. This requires a significant investment in time and money, an inconvenience especially when AM was founded on waste reduction. Sensors like infrared cameras, visible cameras, and photodiodes are capable of detecting defects in-situ without the need for destructive material testing.

The approach to detecting defects in-situ will be to set up sensors around the building part and monitor each layer in real time. These sensors will have different locations that best reflect the sensor's needs. The sensors used are one visible camera, one high speed phantom camera, one infrared camera, and three photodiodes. These sensors are used in parallel for each experiment and the data is cross analyzed for comprehensive defect detection.

2.1.1 3-Color Spectroscopy Physics and Background

The field of spectroscopy studies the behavior of light. Traditional welding applications use spectroscopy to analyze the weld quality based on plasma emissions. Understanding how light creates the signal output for spectrometers and photodiodes is required when analyzing the results from in-situ inspected builds. The basics of spectroscopy begin with the analysis of the plasma plume located directly above the working surface of an LPBF AM build. This plasma plume consists of evaporated metal. The vapor dilutes with the surrounding inert argon gas creating the plume [50]. The plasma plume is the main source of light leading to the identification of certain metallic elements species in the plume that have evaporated. The light emitted from the plume will give off specific wavelengths based on the energy absorbed by the material. The wavelength of light is directly affected by the energy of the system, and the material accepting the energy. Equation 2.1.1 represents the relationship between energy and wavelength.

Equation 2.1.1

$$E = \frac{hc}{\lambda}$$

In Equation 2.1.1, E represents energy, h represents Planks constant, and λ represents wavelength. Spectrometers are powerful instruments that are able to determine a large range of wavelengths, however they are very expensive; less expensive sensors can be used to acquire similar information of the LPBF build and evaluate key quality factors. Photodiodes function similarly to spectrometers without the need of a dedicated spectrometer. This is especially useful when only a few wavelengths are of interest.

2.1.1.1 Behavior of Light

Understanding how light behaves is essential for analyzing photodiode data and selecting proper filters to collect meaningful results. The spectrum of visible light ranges from 400 to 700 nm, from violet to red. These wavelengths are a result of the energy in the system. Equation 2.1.1 determine the energy or wavelength and then known wavelengths of light are used to calculate the energy. This approach creates a magnificent identification tool for unknown species of elements on the periodic table. Each element on the periodic table has a certain number of orbits surrounding the nucleus. Each orbital will house a given number of electrons depending on the element. When an electron is excited due to the addition of energy into the system, the electron jumps to a higher orbital in order to accept the energy. When the energy releases, it is in the form of a photon, or light. This photon will have a known wavelength determined by the distance the electron travels when returning to the ground state. This creates a fingerprint for each element because all elements will have a different number of electrons leading to different wavelengths emitted when a photon releases. The photodiodes used in this approach are equipped with a filter at the identified wavelength of interest and thus collect the light emitted from the plasma plume during a LPBF build at this wavelength.

2.1.1.2 Photodiode Detection Process

A photodiode, or diode, is a light detector connected to a fiber optic positioned close to the LPBF build substrate. Diodes collect the photons emitted from the plasma plume during the laser material interaction. Photodiodes are similar to cameras in that they capture light intensity; however, cameras collect intensities with a spatial location. The intensities from a photodiode are calculated based on the photon species targeted and the

density of photons are collected for the entire viewing area at one time. This creates a relative intensity for each collection period. Diodes, also unlike cameras, do not need to record and save larger amounts of data. A camera collects data based on intensity and location leading to larger files and longer saving times. A diode is only collecting light intensity for one species, which allows for a significant reduction in the time it takes to save data. This is the main reason diodes are considered for process monitoring of LPBF. Diodes are able to collect data at rates approaching 10 KHz. This allows for a comprehensive view of the plasma plume behavior. Once the data is collected for each layer of a build, the data can then be used to evaluate each layer and identify possible defects. Figure 2.1 gives an example of relative intensities during an LPBF build. The relative intensity is located on the y-axis and time on the x-axis.

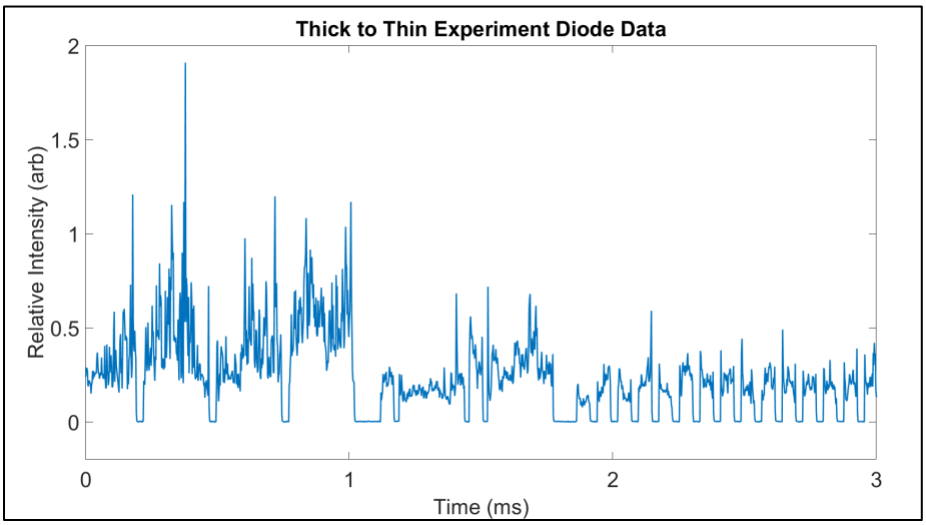

Figure 2.1: Photodiode sensor output of the laser strikes during LPBF.

Photodiode data is collected with respect to time. Longer periods with the laser on will result in wider segments of relative intensity. Figure 2.1 demonstrates that when the laser is off the photodiodes collect zero photons leading to zero for the signal. Therefore, the longer the laser is on the wider the segments in the photodiode data. The middle of the

graph represents the contour for the thin section. The dimensions of the thin section are 10 mm x 2 mm. The photodiode will visualize longer periods with the laser on during the 10 mm section and shorter periods during the 2 mm section. This is one way to identify the geometry of the part without the need for a camera.

2.1.1.3 Filter Selection

As stated in Section 2.1.1.1, the photodiode will detect the light in the visible range. Preliminary experiments are used to modify the diode with a filter at the identified wavelength to detect the specific material elements in alloy 718. Knowing the wavelength of light emitted by alloy 718 is crucial in understanding the behavior of the plasma plume. The first experiment to determining the specific material elements in the plasma plume involves data collection with an Acton Grading Spectrometer. The grading spectrometer is able to collect all wavelengths of light during an experiment. Wavelength data is collected in a 60 nm window and then a monochromator is rotated to a new 60 nm window until the wavelengths of the entire visible spectrum are collected. The LPBF part used is a simple cube that processes each layer while the Acton spectrometer is collecting data. This data is spliced together in overlapping regions of wavelengths to create a full visible spectrum wavelength response. This data accurately represents the wavelengths visible during an LPBF build of alloy 718. With this data, the wavelengths are then cross referenced with the National Institute of Standards and Technology (NIST) database for spectral lines. Here, a complete list of elements is cataloged indicating wavelengths and relative intensities based on material. When selecting wavelengths to analyze it is important to select wavelengths that have strong intensities when viewing with the grading spectrometer, guaranteeing that these appear with less sophisticated instruments. For the

approach used in this work, the highest intensity wavelengths are selected for the photodiode filters.

Ion	Observed Wavelength Air (nm)	Unc. (nm)	Ritz Wavelength Air (nm)	Unc. (nm)	Rel. Int. (?)	A_{ki} (s^{-1})	Acc.	E_i (cm^{-1})		E_k (cm^{-1})
Cr I	515.18267	0.00013	515.18265	0.00003	13			8 095.1842	-	27 500.3699
Cr II	515.1913	0.0002	515.19173	0.00011	2			54 868.497	-	74 273.3409
Cr II	515.34974	0.00006	515.349758	0.000024	11			30 307.3672	-	49 706.2607
Cr I	516.0465	0.0003	516.046501	0.000021	3			7 927.4410	-	27 300.1433
Cr I	516.077	0.003	516.0751	0.0016	5			46 637.2307	-	66 008.86

Figure 2.2: Data collected from the National Institute of Standards and Technology (NIST) [51].

The filters of the photodiodes are very important in order to collect meaningful data. An initial experiment was performed by UTC to determine the filters to use for this work. After analyzing the Acton spectrometer wavelength intensities, filters were selected based on the values obtained. For alloy 718, the strongest intensity wavelengths are 422 nm, 455 nm, 520 nm, and 530 nm. Data collected from the Acton spectrometer in Figure 2.3 shows the response from 470 nm to 530 nm, indicating a strong signal at 520 nm. These lines correspond to chromium lines based on the information in the NIST database. Once the filters are attached to the photodiodes, only light ± 5 nm will be detected. For this research 520 nm, 530 nm, and 640 nm filters create the 3-color spectrometer. The 3-color spectrometer earns its nomenclature by focusing on three wavelengths, or colors, on the visible spectrum.

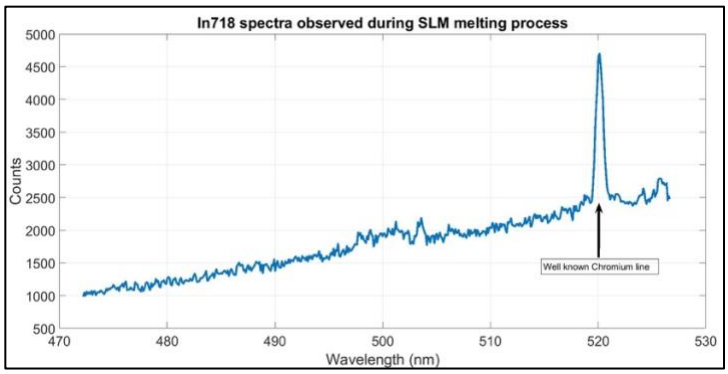

Figure 2.3: Acton spectrometer data collected to find strong spectral features in alloy 718 [52].

The 520 nm wavelengths correspond to the strong chromium lines, the 530 nm correspond to the strong chromium and strong iron lines, and the 640 nm wavelength corresponds to zero spectral line but is selected for noise cancellation. After collecting data with the 520 and 530 nm photodiodes, the noise is removed using the 640 nm signal. Determining changes in temperature during a LPBF build is theoretically possible by taking the ratio of 520 nm and 530 nm wavelengths based on the Boltzmann method [44]. This change in temperature would create a useful metric for part quality determination and parameter development.

2.1.1.4 Plasma Plume Behavior

The plasma plume is a phenomenon that occurs when a laser interacts with material, and common for many different types of laser AM systems. Vast amounts of energy are added in the form of heat to the metal powder, resulting in melting and evaporation which produces plasma. It is expected that the behavior of the metal vapor that is present above the melting material is important to understand for three reasons. First, changes in process parameters affect the plasma plume. Second, the plume will behave differently in the wake of a defect. Third the plasma plume behavior correlates to the microstructure via

temperature analysis and species identification. When the metal melts and enters the molten state, black body radiation is present in the system. This blackbody radiation is also measurable using the photodiodes. The radiation from the melt pool appears from the electron temperature and is not consistent depending on the distance from the center of the melt pool. Naturally, as the distance increases the radiation will fall off. Figure 2.4 illustrates the distribution of electron temperature of a CO2 laser.

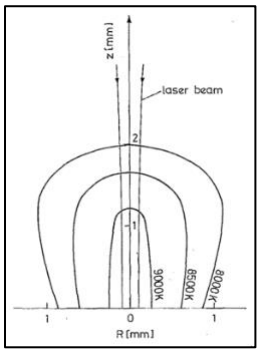

Figure 2.4: Schematic of the plasma plume behavior and blackbody radiation distribution [53].

The distribution of electron temperature through the plasma plume does not create new challenges. The only necessary element needed for the plasma plume behavior is that the energy density is sufficiently high to be able to see the selected signatures in alloy 718. In other forms of laser AM such as Direct Energy Deposition (DED), the minimum power needed is 2 kilowatts [54]. For smaller, faster systems like LPBF, much less power is needed to perform the melting process.

2.1.1.5 Temperature Calculation

The temperature of a melt pool in-situ holds information related to the quality of the part. There are several sensor techniques that can determine this number; however, the photodiodes used in the 3-color spectrometer approach have multiple ways to determine

the temperature and can process the data at faster speeds. Photodiodes can determine the temperature of a melt pool in three ways: the Boltzmann equation and Boltzmann plot, the Saha-Boltzmann equation, and the line-to-continuum intensity ratio [55]. Figure 2.5 demonstrates the Boltzmann plot for titanium, where multiple spontaneous rates of titanium are used with a best-fit line to determine the uncertainty in plasma plume temperatures. The slop of the lines represents the inverse temperature multiplied by the gas constant R.

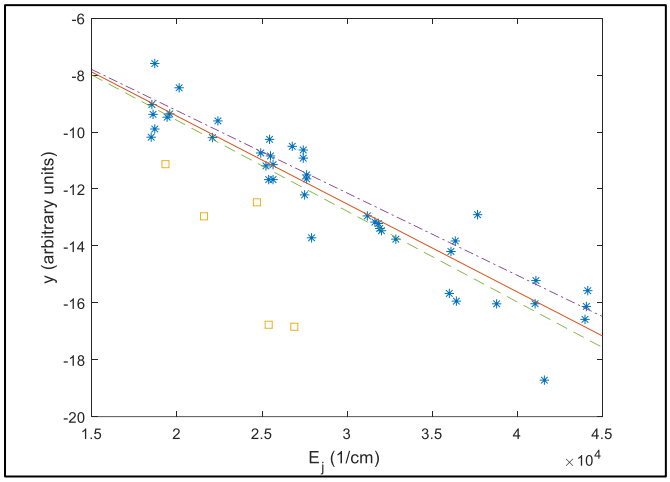

Figure 2.5: Boltzmann plot for titanium [52].

The most common temperature calculations used in spectroscopy are the Boltzmann equation and Boltzmann plot, the Saha-Boltzmann equation, and the line-to-continuum intensity ratio. For these temperature calculations to work there needs to be either an assumption or a confirmation that the system is an optically thin spectral line emission and that there is local thermal equilibrium. In the case of an optically thin spectral line, this condition must be true. If the optically thin spectral lines are not true, then the spectral line will self-absorb, creating inaccurate line widths and incorrect representation of temperature and electron density. The line widths refer to the emission spectrum of

elements. Each element has a known line or band in the emission spectrum, and these line widths will increase causing inaccurate data if the plume is not optically thin. The second constraint is a local thermal equilibrium. This would suggest the Boltzmann and Saha equations match the distribution of free electrons from the Maxwell-Boltzmann distribution, describing how ideal gasses affect speeds. The line-to-continuum assumes that there is a local thermal equilibrium; however, the line-to-continuum does not assume an optically thin spectral line [55].

Unfortunately, due to the low power used in LPBF the typical ways of measuring temperature in-situ for a larger range of processing parameters cannot apply. For this reason, a multi-sensor approach is investigated. In low power LPBF builds, there are not enough strong spectral lines for alloy 718 for an Acton grading spectrometer to detect. For this reason, the Boltzmann equation and Saha equation are not viable [56]. The line-to-continuum uses wavelength comparison to evaluate the quality of the build. A similar approach focuses on minimal wavelengths using a 3-color spectrometer and then temperature verification through multiple sensors to validate the 3-color spectrometer.

2.1.1.6 3-Color Spectrometer Detectivity and Calibration

The results of the 3-color spectrometer data require proper calibrations prior to data collection. The light source that spectroscopy uses to determine intensity is dependent on six factors: wavelength, distance, interference, responsivity, transmittance, and spectral radiance. Section 2.1.1.3 discusses the dependence of wavelength on the spectral response. The wavelengths of interest were determined through experimental study and spectral response of the material. However, additional factors such as distance, responsivity, and interference are the main concern. Distance determines the intensity of the signal due to

Planks Law. Blackbody radiation coming from the plasma plume drops off with distance. Therefore, high intensity is recorded when the sensors are closer to the plume. This factor remains constant to eliminate any fluctuation in signal intensity during experiments. Interference appears in many forms. Interference may come from the light located above the lab, the noise that is associated with the spectrometer signal, and the change in signal due to light traveling through a different index of refraction such as Plexiglas that houses the LPBF system.

Responsivity changes for the detectors, fiber optic, and filters. Responsivity is the measurement of electrical signals based on light intensity. Light waves appear on a spectrum, and as the light waves increase in wavelength the responsivity will increase based on Planks Law of blackbody radiation. This indicates that wavelengths in the red region (700 nm) will appear stronger than the violet region of light (400 nm). The 3-color spectrometer focuses on three different wavelengths meaning the responsivity will increase as the wavelength increases. The ratio of two wavelengths skews if responsivity is not considered. Figure 2.6 demonstrates the change in responsivity based on wavelength of the detectors.

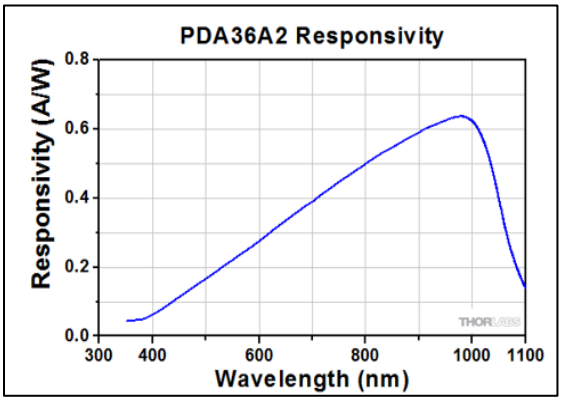

Figure 2.6: Responsivity curve for the photodiodes given from the product specifications [57].

Similar to responsivity, the fiber optic cable, detectors, and filter do not transmit light equally. The fiber optic cable is truncated and divided into three sections, each leading to a different photodiode. Each section of the fiber optic cable does not transmit the same amount of light, nor do the photodiodes detect the same amount of light. Manufacturing variation is responsible for the difference in transmittance for both the fiber optic and the photodiodes. Filters transmit different percentages of light due to the blackbody curve phenomenon; meaning higher transmittance at higher wavelengths.

Spectral radiance is the final influence on photodiode data. Spectral radiance is the phenomenon where high radiation is located at higher wavelengths. This is intuitive because as the wavelength of light increases through the visible region and enters the near infrared, humans are able to detect this radiation in the form of heat. Planks equation for spectral radiance is with respect to wavelength and temperature as described in Equation 2.1.2 [58].

Equation 2.1.2

$$L_\lambda = \frac{2\pi hc^2}{\lambda^5} \frac{1}{\left(e^{hc/\lambda kT} - 1\right)}$$

The equation for spectral radiance calculates the photon density at any given wavelength and temperature. The implications of this equation connect the wavelength of light to the temperature. This begins to open the possibilities of determining temperature through 3-color spectroscopy. In Equation 2.1.2, *h* represents Planks constant, *c* represents the speed of light, λ represents the wavelength, *k* represents Boltzmann's constant, *T* represents temperature in Kelvins, and L_λ represents the spectral radiance. Five factors combine into one variable known as Detectivity. The Detectivity is responsible for

acquiring all the known (and unknown) factors that determine the response intensity. The five factors that contribute to the Detectivity are wavelength, distance, interference, responsivity, and transmittance. Notice all factors are constant and stay consistent during experimentation. The principle of Detectivity allows the comparison of different diode outputs without the need for overly complicated calculations. Equation 2.1.3 is the relationship of Detectivity and spectral radiance with respect to the voltage output that is the photodiode signal.

Equation 2.1.3

$$V_D - V_B = DL_\lambda$$

In Equation 2.1.3, V_D represents the voltage collected by the detector (photodiodes), V_B represents the voltage collected from the blackbody, L_λ represents the spectral radiance, and D is the Detectivity of the system. All the factors contributing to the Detectivity are values determined experimentally with a blackbody. A blackbody is a known temperature source with an emissivity of one. For this experiment, the blackbody was set to three different temperatures: 900°Celsius, 1000°Celsius, and 1200°Celsius. Each temperature has a known wavelength, leading to accurate spectral response calculations. The photodiode data is accurate and respectable after calibrations are complete.

2.1.2 Visible Camera Physics and Background

In this research, two different types of visible cameras were used to collect detailed data on the LPBF process. The first camera is a high-speed camera that collects details of each melt pool, and the second is a low-cost visible camera that is able to collect melt pool data with low exposure time and surface data with high exposure time. The function of the

visible camera is to collect light intensities over a spatial region. This happens when a photon of light is collected by the visible camera. The camera has a focal plane array that is 1 cm x 1 cm as shown in Figure 2.7. This focal plane array represents the resolution and pixel values. As the photon enters the camera the photon strikes this focal plane, gaining an X and Y location as well as intensity. This happens repeatedly, creating larger intensities and a more densely populated focal plane. The intensities are saved in their X and Y location, which is then turned into the image seen.

Figure 2.7: Focal plane array shown. The area of the pad represents the area of the image [59].

This happens every layer and increasing the exposure time will increase the density of photons on the focal plane, resulting in a bright image. Visible cameras are used for process monitoring because they are easy to understand and use, and they collect useful data regarding the surface and melt pool behaviors. The two different visible cameras will be disused to show their relevance and processes.

2.1.2.1 High-Speed Camera

During the LPBF process, a high-energy laser strikes metal powder causing a transfer of energy, often violently. The majority of the energy is channeled into melting the

metal powder, however not all of the powder particles conform into the desired part. Few of the particles receive the energy and eject into the environment. This phenomenon is called particle ejection. The particle ejections give information on the process parameters that helps conclude if the parameters are adequate. One way of capturing these ejections is through a visible camera. The first concept of using a visible camera came by high-speed cameras. A Phantom V9.1 high-speed camera is able to capture events at extremely high speed. High-speed cameras are widely used due to high capture rates resulting in as much information and detail as possible. Typical frame rates are in the thousands per second, depending on the camera. In this research, the Phantom camera collects data at 10,000 frames per second. This results in one-two frames in every melt pool.

With high speeds, many different nuances can be detected. For example, as the particle ejections fly into the surrounding atmosphere, the high-speed camera is able to determine their speed This is done by measuring the length the particle streaks over the course of a few frames. The downside to the larger amounts of detail collected through the high-speed camera is the files sizes and saving times. The saving times are on the scale of minutes, and during an LPBF minutes relates to multiple layers. This is not conducive to comprehensive defect detection, nor is it viable for closed loop applications. The files sizes are also cumbersome to deal with, causing many storage devices to become full quickly. One alternative to this is to find the ratio of frames per seconds to saving times that could lead to closed loop applications.

2.1.2.2 Low Cost Visible Camera

Low cost cameras have much slower frame rates resulting in lower cost. It is important to determine the adequate frame rate. If the frame rate is to slow then not enough

data is collected to have any confidence in the inspection, and if the frame rate is too long it leads to larger files and longer saving times similar to the high-speed camera. The low-cost camera that is used in this research is a Basler acA1920-155 um. The Basler camera has a frame rate of 75 frames per second with a resolution of 1928x1208. The meaningful data collected with the high-speed camera is possible to detect with the low-cost camera. The information gained by using a visible camera relates to the physical set up of the experiment. The visible camera is responsible for detection of small changes that other sensors cannot detect. For example, during an LPBF build occasionally powder will not cover the entire part. This will not be extremely evident in the 3-color spectrometer data but will stick out brightly in the visible camera data. This cross reference of data emphasizes the strength of the multi-sensor approach.

2.1.2.3 Visible Camera Approach

There are two main approaches for using the visible camera. The first is collecting melt pool information with low exposure time. Exposure time is the variable that controls how long the aperture of the camera remains open to collect photon data per frame. Collecting melt pool information by analyzing the melt pool geometry and determining if the melt pool is interacting with or creating a defect is mainly determined visually. The second approach is using high exposure times to evaluate the surface and melt pool behavior. With high exposure time, the camera is collecting data for nearly the entire layer. Figure 2.8 is an example of the data collected using the long exposure technique. The result is a long streak representing the laser. The light collected is much brighter and as a result, the signal saturates. This can be avoided by introducing neutral density filters to block the intensity of the light. The neutral density filters do not block information from reaching the

sensor but merely dampen the intensity to show more detail. Collecting data in this way is very useful because it allows the capture of the entire layer, to be later stitched together for a comprehensive view of each layer. This data collection approach used in unison with the other sensors generates useful information. A similar approach to this uses layer imaging to map out the entire part and analyses where defects occurred from lack of powder and spreader defects, which enables the tracking and locating of defects in an LPBF part [60].

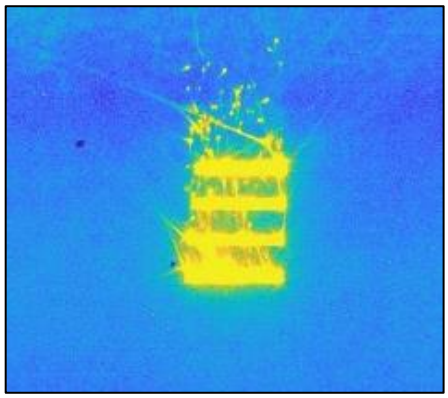

Figure 2.8: Long exposure technique for low cost visible camera.

The long exposure time is useful in that it helps to recover some of the data that is lost when the frame rate drops. In both cases of high and low exposure time, the data collected is valuable to identify part quality of an LPBF build. The low exposure rate creates individual information on melt pools, while the high exposure rate explores the surface of the part and is able to detect surface changes.

2.1.3 Thermal Camera Physics and Background

The most common sensor used in AM process monitoring is a thermal camera focused on the infrared (IR) region of light. The wavelength of light in the infrared region is divided into sections: near IR (NIR), short-wavelength IR (SWIR), mid-wavelength IR (MWIR), long-wavelength IR (LWIR), and far IR (FIR). In each IR region, the temperature

values change due to decreasing radiation. The range of temperature for NIR is 3500 to 1700°C, SWIR 1700 to 700°C, MWIR 700 to 89°C, LWIR 89 to -80°C, and FIR -80 to -270°C. For LPBF NIR is used [61].

The temperature for LPBF is greater than 1800°Celsius. This is determined from the large amount of radiation coming from the melt pool. In this temperature range, great thermal imaging is possible. The thermal camera used is the same Basler acA1920-155 um; however, there are added filters to eliminate the visible light and to eliminate any laser light from reaching the camera. There are two filters, a bypass filter set to eliminate the visible light below the IR region, and a notch filter designed to eliminate the 1040 nm wavelength coming from the laser.

2.1.3.1 Thermal Calibration

The calibration of the thermal camera is incredibly important. This step ensures that all temperature calculations in the future are grounded in existing data. To calibrate the thermal camera (and all sensors) a blackbody is used. A blackbody is a thermal source that has a known emissivity of one. For this research, a blackbody set to three temperatures is used. Three temperatures are necessary in order to create an arch used for predicting temperature later. The three temperatures used for the blackbody were 900°C, 1000°C, and 1200°C. Hotter temperatures would have been preferred due to the hot temperature in AM, however the max temperature of the blackbody was 1200°C. This ensured that the data was accurate in elevated temperatures above 1200°Celsius. Once the calibration data was collected, a computer software created by UTC used the information as well as emissivity information to create a temperature calculator for analyzing the thermal camera data.

Figure 2.9 illustrates the data collected from the thermal camera. Each frame goes through temperature calculations to determine the temperature of the melt pool.

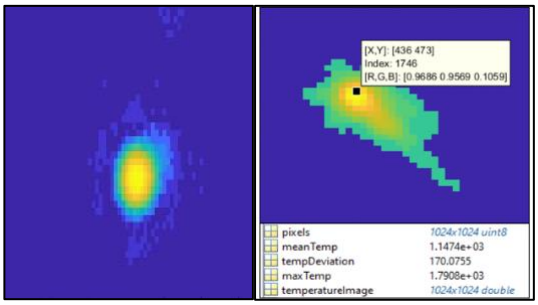

Figure 2.9: One frame from the thermal camera in-situ with temperature calculations.

The thermal camera is very important for the multi-sensor approach. The thermal camera is able to collect reasonable temperature values for melt pools during an LPBF build. The thermal data is able to identify the relationship between thermal behavior and certain outcomes such as microstructure, part delamination, and residual stress. These values collected in unison with the visible camera data help determine the effects of the photodiode data. By collecting many forms of data and using them to verify the photodiode response, accurate information for the part quality, temperature, surface topology, and microstructure are determined [62].

2.2 Equipment

2.2.1 Universal Technology Corporation PDC Capabilities

Universal Technology Cooperation (UTC) specializes in AM through LPBF. This research began on one Product Development Cell (PDC) for all experiments. The PCD capabilities and points of strength are displayed. The dimensions of the PDC are for smaller AM builds with a max build volume of 4 in. x 4 in. x 2 in, with a supply volume slightly larger since there is no need for a build substrate. The main strength of this PDC is the

ability to apply and set up any sensor in any location. Figure 2.10 is an image of the PDC used and the linear motion of the two chambers.

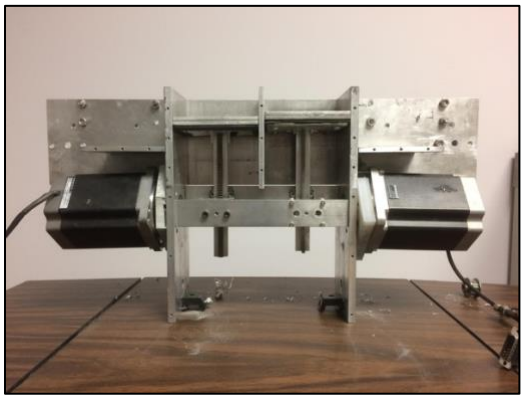

Figure 2.10: UTC's PDC displaying the build chamber (right) and the supply chamber (left).

Strong stepper motors control the linear motion of the supply chamber and the build chamber. The supply chamber fully retracts to provide space for the powder to reside. The build chamber had an alloy 718 substrate on top and was leveled.

2.2.2 Sensor Location

There were four sensors used for process monitoring of alloy 718 in the LPBF test bed. The four sensors are two visible cameras, one low cost and one high-speed, one thermal camera, and three diodes, which share one fiber optic cable. Figure 2.11 exhibits the locations of all sensors.

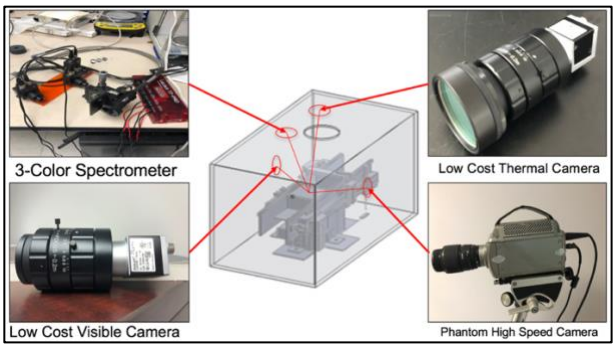

Figure 2.11: The UTC PDC and the location of each sensor.

For the first two experiment the sensors were located in the same positions shown in Figure 2.11, however for the last experiment the thermal and visible camera were both located at the front of the test bed. The positioning of the sensor is very important because each one focuses on a different parameter. The thermal camera focuses on the melt pool; therefore, the cameras location is above the substrate which provides a better view of the melt pool. The diodes are located above the substrate as well, but at an angle. This allows the diodes to collect data on the plasma plume. The plume appears best at an angle because it will rise vertically when the laser is on. The visible cameras collect surface topology and particle ejections; therefore, they are located on the front and back of the test bed where other elements of the system do not obstruct the particle ejections.

Chapter 3: Preliminary Sensor Collection

3.1 Design of Experiment

A single layer within a part fabricated with LPBF can consist of hundreds of laser passes depending on the geometry. To comprehend the solidification and thermal gradients of a part, a firm understanding of how the laser affects the molten metal in alloy 718 must be obtained. A preliminary experiment used in this work to explore the laser behavior is through single beads. Single beads are individual laser lines drawn on an alloy 718 plate. All the sensors are used to collect data for each line, determining the proper set-up and sensitivity scale of the sensors before fabrication of larger parts. This first experiment explores two important variables, processing parameters and the addition of powder. The experiment is divided into two experiments, constant parameters and variable parameters. The constant parameter experiment consists of 15 lines of nominal alloy 718 parameters. The second experiment changes the parameters to create a matrix of parameters. Three speed and five power levels are used, and the results acquired help determine the sensor's accuracy. The addition of powder has the potential to create variation in the sensor data because the size distribution creates a varying layer thickness and spread through the bead width. In order to reduce variation, preliminary experiments did not use powder. Each experiment sheds light on the process monitoring capabilities for the multi-sensor approach.

3.2 Single Beads Constant Parameters

The constant parameter experiment is used to explore if fluctuation in the sensor data relates to the noise in the system. For the constant parameter experiment, all sensors

collected data for each line. The sensors included high-speed camera, visible camera, thermal camera, and three photodiodes focused on the 520 nm, 530 nm, and 640 nm wavelengths. Constant laser power and speed settings were used to melt a 718 plate and gain insight on how the 3-color spectrometer behaves without added variation caused by changing parameters or the addition of powder. The parameters were set to the nominal power and speed for LPBF of alloy 718. The parameters were 1000 mm/s and 300 W (60% power of the laser). Figure 3.1 illustrates the experiment set up and location of the 15 lines. The lines were divided into three groups of different speeds, five lines at 500 mm/s, 1000 mm/s, and 1500 mm/s shot in the order of slowest to fastest.

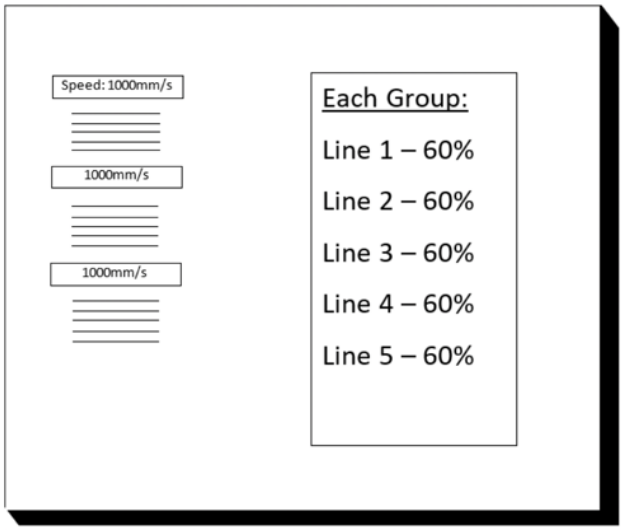

Figure 3.1: Schematic for the constant parameter experiment.

The experiment was performed twice including a change in direction. The constant parameter lines were created with the laser strikes going from left to right and then from right to left.

3.2.1 Data Analysis

The data from all sensors is analyzed in this section. Of these sensors, more focus was on the 3-color spectrometer due to the unknown effects the experiment would have on the data. In Figure 3.2, all sensor data for the single beads is displayed. The thermal camera displays one melt pool towards the end of the line and determines the temperature of the melt pool. This is calculated by taking the unsaturated pixel values to determine temperature when referenced with the calibration data of the blackbody. The temperature calibration procedure was developed by UTC and is implemented through a MATLAB script. The script takes the known values from the blackbody calibration and processes the pixel values through and equation for blackbody curves to predict the temperature. The visible camera displays four melt pools from the single beads. Due to the frame rate of the camera, only two frames from each line were captured. However, the visible camera does display the direction the melt pool was traveling and the location of the plasma plume. The high-speed camera data is compiled to show the entire line. The photodiode data is graphed to show each line and the relative intensity. The left to right experiment displays an overall higher relative intensity than the right to left experiment.

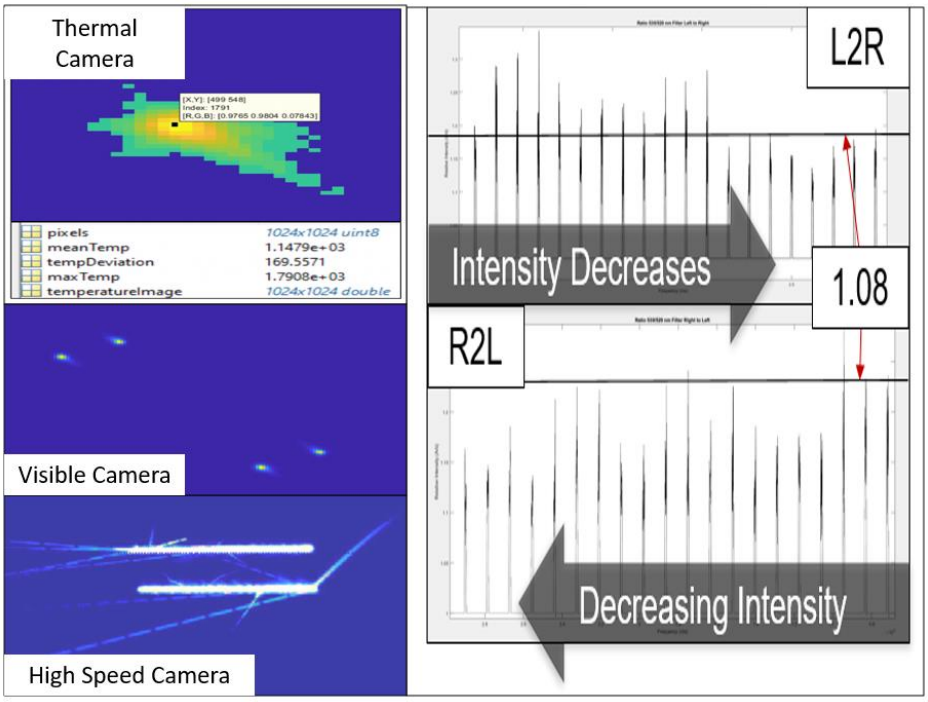

Figure 3.2: Constant parameter sensor package.

Based on the sensor data, there was no significant change in the cameras and temperature reading, which is as expected because the same processing parameters on each line should achieve similar thermal behavior. The visible camera and high-speed camera both show the melt pool, but due to the resolution of the high-speed camera and the frame rate of the visible camera, it is difficult to find new information that the thermal camera and photodiodes do not already show.

3.2.1.1 Thermal Camera

The thermal camera captured temperatures approximately 1791°Celsius, which is within the melting region of alloy 718 and even close to the evaporation point. Figure 4.3 gives a closer inspection of the thermal camera image and temperature calculations.

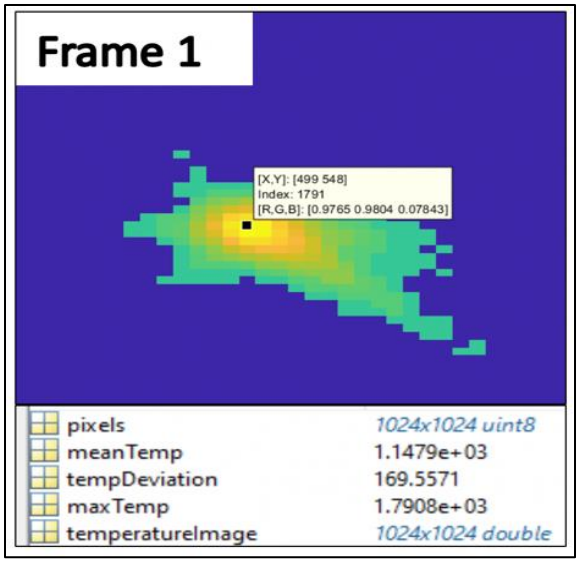

Figure 3.3: Thermal camera data estimates the temperature of each melt pool. This melt pool represents 1791°Celsius.

The thermal script calculates more than just temperature in the temperature calculations. The software is able to evaluate all frames of a build, depict the quality of the melt pool as well, and tail length, max temperature, mean temperature, which is visible in Figure 3.3.

3.2.1.2 Visible Camera

The visible camera was able to capture the direction and orientation of the plasma plume. This is referenced with the photodiode data to make sure the relative intensity is captured correctly. Figure 3.4 displays the four frames captured by the visible camera. The low frame rate of the camera is maxed at 75 frames per second, leading to a capture rate of only 10% of all melt pools. This is not ideal because so much of the area is not visualized. However, even though the camera does not capture a majority of the melt pool information, it does display the melt pool geometry and plasma plume direction. This information is

eliminated in the thermal camera due to the low exposure time needed to capture the melt pool only.

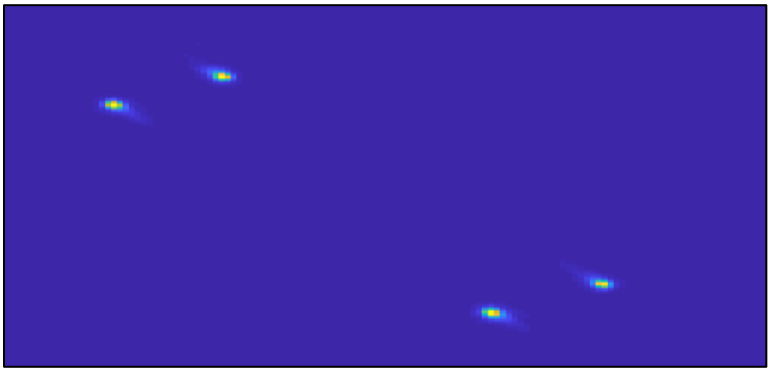

Figure 3.4: Visible data of four frames during the constant parameter experiment.

When comparing the visible camera to the photodiode data it is difficult to match the data exactly. This is due to how the data is collected by the different sensors. One frame from the visible camera with a low exposure time of 700 µs will correlate with 6.5 data points of the diode data. This is calculated from the data collection rate of the photodiodes, 9280 data points per second, and the exposure time of the camera.

3.2.1.3 High-Speed Camera

The high-speed camera normally appears as video evidence for the melt pool behavior. However, a compiled image of all frames can also be used to represent the data. The compiled images create a map of the entire line, which is useful because it can find particle ejections or abnormally wide melt pool widths. The primary use of the high-speed camera is to create video evidence of every melt pool that correlates with the photodiode data. A side-by-side graph can represent each frame from the high-speed camera and the intensities from the photodiode data, displaying the relative intensity of the melt pool and the visual representation of the melt pool.

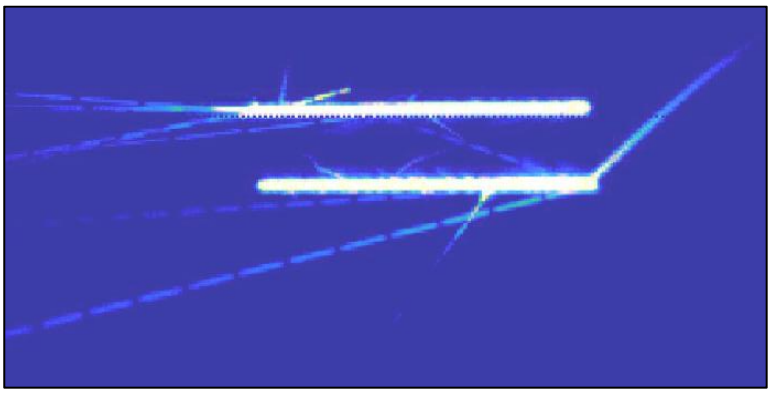

Figure 3.5: High-speed data compiled for the entire lines during the constant parameter experiment.

This becomes useful when the high-speed camera determines if there is a problem in the current layer, which can appear as thick or no powder over the part surface, and as particle ejections. All of these problems will cause a fluctuation in the diode data, and it is important to understand why the fluctuations are happening to help determine the type of defect that would appear.

3.2.1.4 Spectroscopy Photodiodes

Finally, the photodiode data taken during the experiment is represented in the right to left direction and in the left to right direction. It should be noted that the airflow in the argon atmosphere was flowing from right to left. With this knowledge a greater understanding of the sensitivity of the laser is developed. A great understanding of the melt pool facilitates a better understanding of the plasma plume and thus the photodiode data. When comparing the two different directions, the diode data determined that the left to right direction has a larger average relative intensity, which is represented in Figure 3.6.

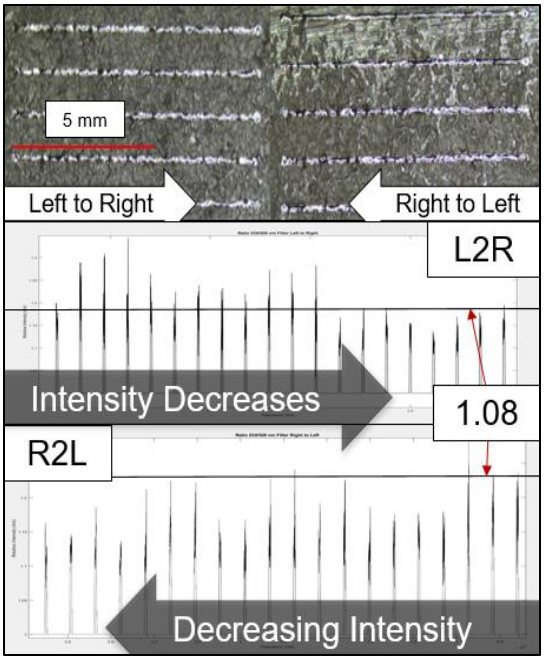

Figure 3.6: Diode data for the left to right and the right to left constant parameter experiment.

As the line is drawn from left to right, the plasma plume is trailing the laser, and adding the velocity of the airflow in the chamber (which moves in the opposite direction), stretching the plasma plume. This changes the orientation of the plasma plume, increasing the area and relative intensity. However, as the line is drawn from right to left the plasma plume is still trailing the laser, but the airflow is also traveling right to left, compacting the plasma plume and creating a lower relative intensity.

3.2.1.5 Multi-Sensor Analysis

The multi-sensor approach displayed significant information in the constant parameter experiment. The thermal camera is able to capture temperature data of the melt pool which helps in the identification of possible microstructures and well as correct process parameters. The visible camera is able to capture the melt pool geometry and plasma plume orientation. This becomes useful when correlating the images with the

photodiode data to help the photodiodes determine if a fluctuation was due to particle ejections, or an improper powder spread. The high-speed camera gives extremely detailed data of the melt pool behavior, with complete coverage of every single melt pool. This is extremely useful because each melt pool can be viewed and matched with diode data, creating a better evaluation of the part quality and process parameters. Finally, the photodiodes capture the subtle fluctuation in the LPBF process with high accuracy. This data collection is more precise when each sensor is cross-analyzed to determine the specific reason why the photodiode data has fluctuations.

3.3 Single Beads Variable Parameters

After completing the constant parameter experiment, the next experiment includes variation of the processing parameters, further increasing the knowledge of the spectrometer response. The variable parameter experiment created a base line for sensor data for different parameter selections. A design of experiments was used to determine the selection of the laser speed and power. Three levels of speeds and five levels of power were used. The lines were in the order from highest power to lowest, regardless of speed. Figure 3.7 demonstrates the location and laser parameters for each line. The parameters range selected in Figure 4.4 was determined based on prior experience to create both optimal parts and parts with defects. By understanding the sensor response from the single bead experiments at the varied parameters, an experimental baseline can be formed to determine the identification of a defect.

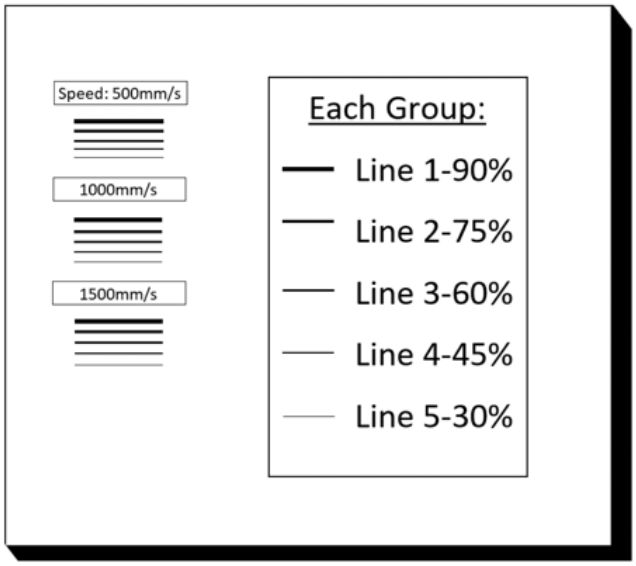

Figure 3.7: Schematic for the variable parameter experiment.

The variable parameter experiment used the same sensors as the constant parameter experiment. The first version of the variable parameter experiment had zero powder on the substrate. This eliminated any fluctuation that variable layer thickness or particle ejections would have on the data. The second version of the variable parameter experiment included powder. This would represent what would happen during a normal build. It is also important to know that there are larger blackbody signals with powder because the particle ejections add to the signal and the powder creates stronger signals in the diode data due to the addition of more blackbody information.

3.3.1 Data Analysis

The same collection standards used in the constant parameter experiment were applied to the variable parameter experiment for consistent and comparable data collection. The variable parameter experiment was designed to show what different process parameters look like in the sensor data. This creates a base line for the senor data, which will help indicate if the process parameters are changing during a LPBF build. A snapshot

of all the sensor data is compiled in Figure 3.8. The visible and thermal cameras show similar data to the constant parameter experiment while the photodiode data changes wildly.

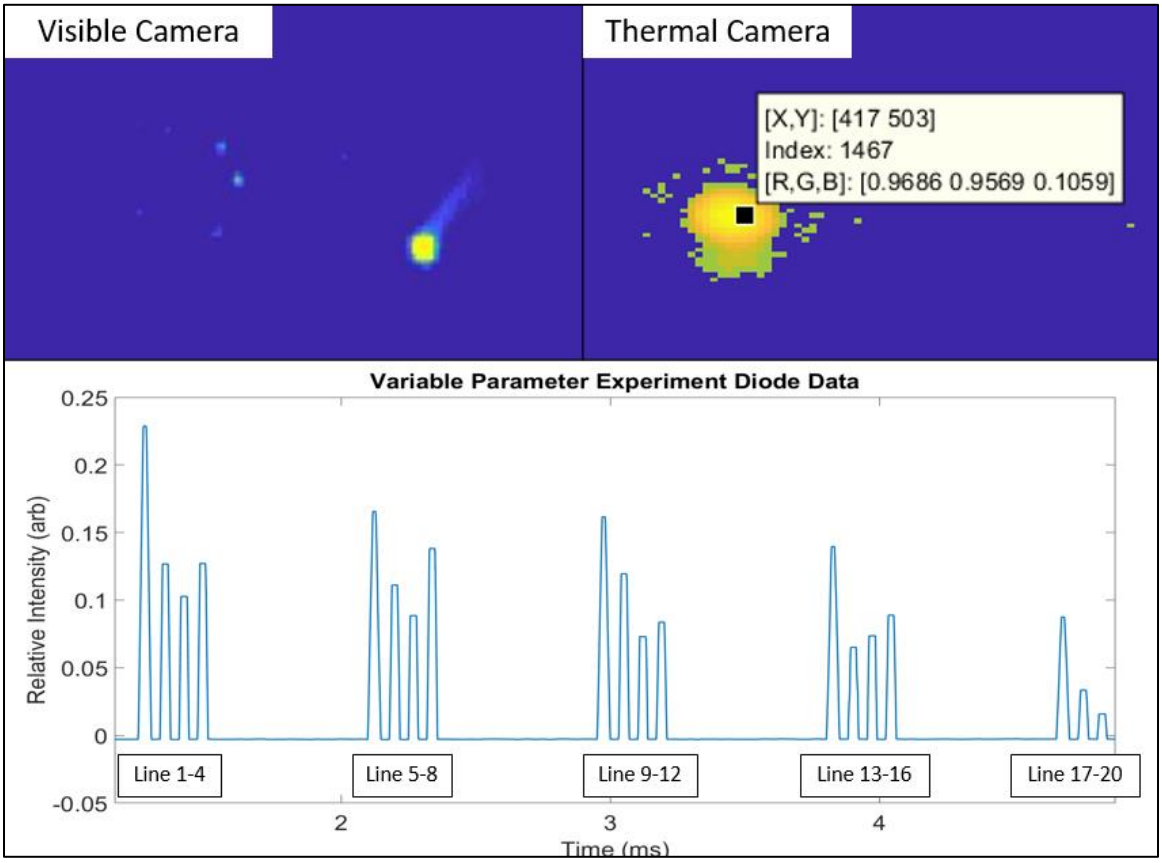

Figure 3.8: Variable parameter sensor package. The visible camera, thermal camera and photodiode data is represented.

The visible camera still displays the melt pool geometry and the direction of the plasma plume. This again is useful when analyzing the photodiode data. The thermal camera is focused on a lower power line resulting in a lower temperature. The photodiodes are graphed with an average to eliminate single points that are extremely high in intensity. This eliminates the outliers from the diode data, allowing the parameters to be seen accurately.

3.3.1.1 Visible Camera

Similar to other experiments, the visible camera displays the plume and melt pool behavior. The image in Figure 3.9 demonstrates the direction the laser is traveling. The visible camera was located on the back of the LPBF machine. The constant parameter experiment already determined that if the laser is traveling in the left to right direction, a slightly high relative intensity is found. This displays the ability the visible camera has to determine visual features that the photodiodes would not be able to make.

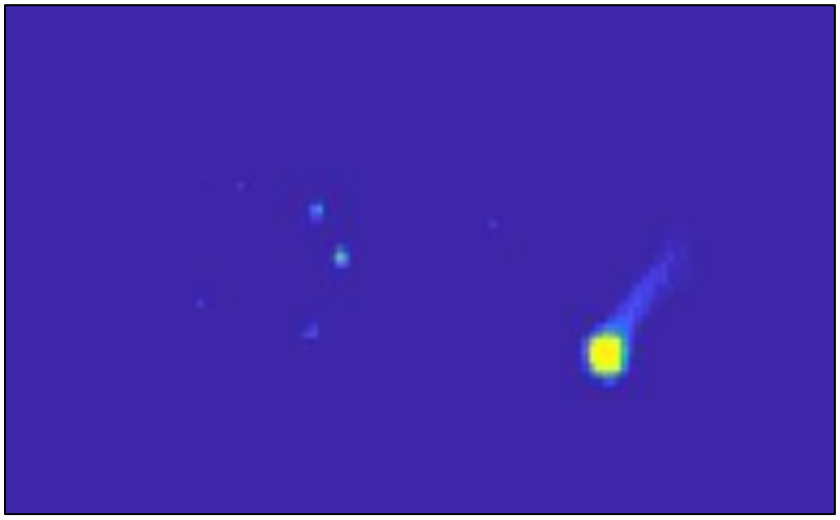

Figure 3.9: One frame of the visible data during the variable parameter experiment.

The visible camera frame in Figure 3.9 also shows the particle ejections that can happen. This is due to the powder particles receiving energy and spontaneously releasing that energy. The particle ejections also appear in the photodiode data as fluctuations due to their added blackbody signatures.

3.3.1.2 Thermal Camera

The thermal camera captured the melt pool temperature, although noticeably lower than the no powder constant parameter experiment. The temperature in Figure 3.10 is

represented by the 'index' of the data point. One important distinction for the thermal camera when compared to the constant parameter thermal data is that this melt pool was collected for the lower power levels. What appears to be a difference in temperature, (with the addition of powder), is actually the change in parameters, which seems intuitive.

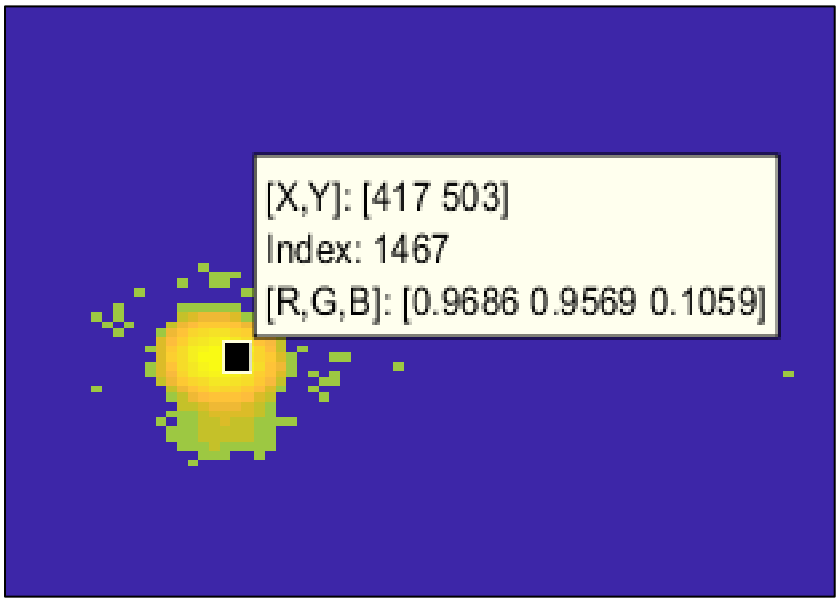

Figure 3.10: Thermal data collected during the variable parameter experiment.

3.3.1.3 Spectroscopy Photodiode

The photodiode data collected in the variable parameter experiment is manipulated to illustrate the effect of distance and power during the variable experiment. The photodiode data shown in Figure 3.11 was averaged based on the intensity of each line. This creates a smoother graph, eliminating single points with very high relative intensity. To view each line and the parameters used, reference Table 3.

Line	1	2	3	4	5	6	7	8	9	10
Power (watts)	450	450	450	450	375	375	375	375	300	300
Speed (mm/s)	500	1000	1500	1000	500	1000	1500	1000	500	1000
Line	11	12	13	14	15	16	17	18	19	20
Power (watts)	300	300	225	225	225	225	150	150	150	150
Speed (mm/s)	1500	1000	500	1000	1500	1000	500	1000	1500	1000

Table 3: Power and speed for each line in Figure 3.11

Table 3 shows that the first group of lines are all set to 450 W. Each group thereafter decreases in power. Each group also displays the three speeds used. After viewing the table and the graph, a trend begins to appear. In each group the highest relative intensity is displayed in the very first line. This line represents 500 mm/s, which would have the highest energy density for each power.

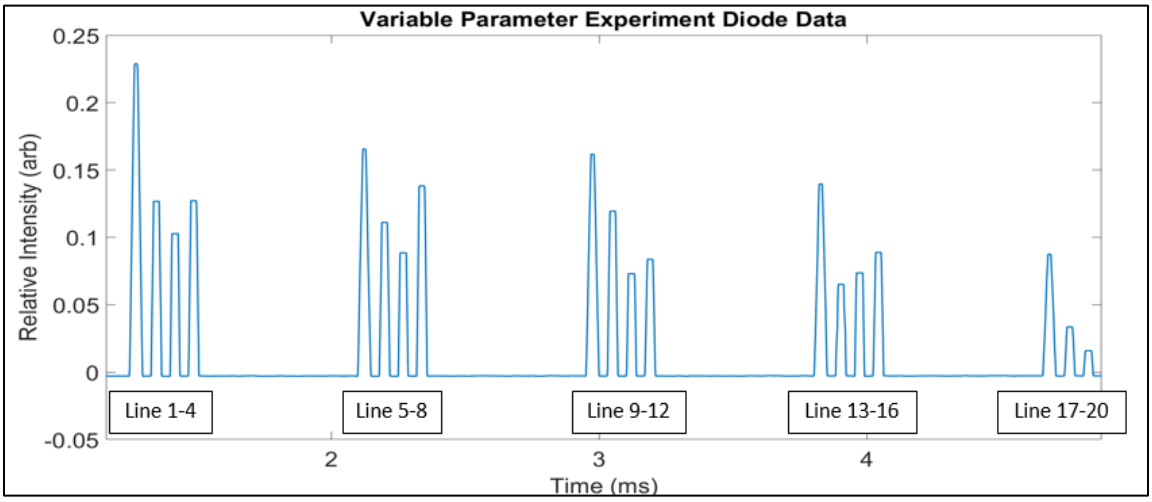

Figure 3.11: 520 nm wavelength diode data collected during the variable parameter experiment.

As the energy density increases, this causes the penetration depth of the laser to increase. This increased penetration creates a spatial difference between the bottom and top of the melt pool. This discrepancy creates a capillary effect on the plume, causing the plume to

penetrate deeper as well. The result of this on the sensor output is a decrease in relative intensity even though there is higher power. This indicates that laser parameters monitored by the photodiodes can increase the accuracy of process monitoring. Another significant element of the diode data is the effect power has on the spectral signal of the material. Figure 3.12 shows the drastic difference between the relative intensities based on power level.

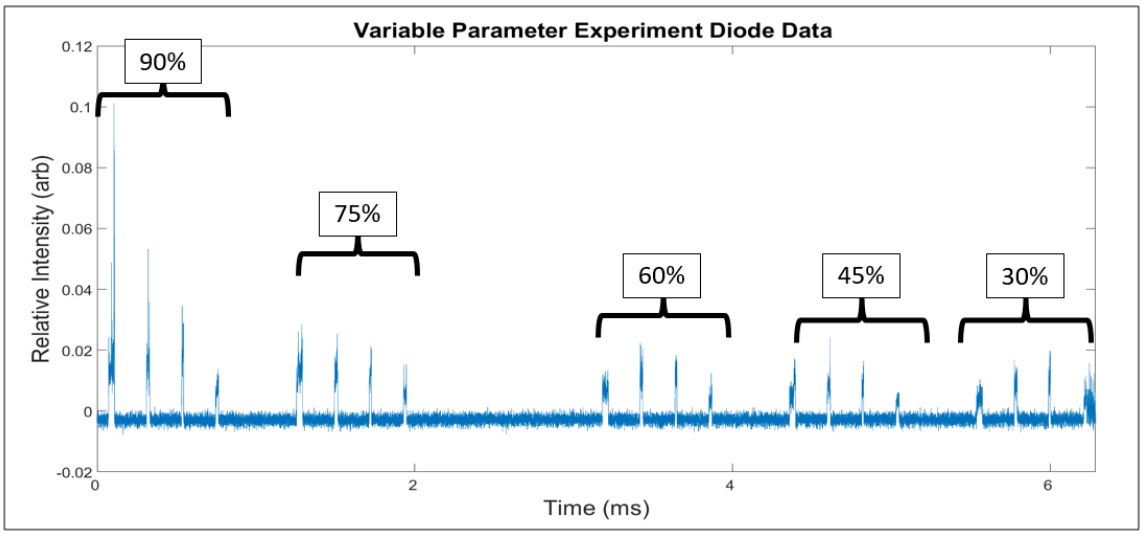

Figure 3.12: 520 nm wavelength diode data for the variable parameter experiment.

After comparing Figure 3.12 with Figure 3.7 with the knowledge that the photodiodes are located at the back of the plate (as in the top of the figure), a change in the data is seen because of the location of the line. The line closest to the diodes captured a stronger signal while the lines farther away resulted in a lover intensity. This, however, is unaffected after the 75% power lines. This is because of one major factor. In future experiments it is determined that the minimum power level should be set no lower than 60% (300 W), because there is not enough spectral signal to see chromium below this threshold.

3.4 Conclusion

The single bead test exposed many of the nuances to process monitoring. The first result came from the photodiodes. Due to the changing direction in the constant parameter experiment, small notifications appear in the visible data as well as the diode data. This data indicated that depending on the direction the laser is traveling, the sensor output changes. This occurs because the plasma plume located directly above the laser on the parts' surface will change in density and orientation, resulting in a lower output signal. The photodiodes also indicate that when a change in energy density of the system can result in a lower relative intensity. The visible camera captures the melt pool behavior and indicates if there are anomalies that the photodiodes cannot see. These anomalies can be particle ejections that each carry their own blackbody radiation. These particles, if large enough, can create inaccuracies in the photodiode output. The thermal camera can indicate the temperature of the melt pool, which changes depending on the process parameters.

Chapter 4: In-situ Detection of the Influence of Geometry and Processing Parameters on Microstructure

4.1 Design of Experiment

The first experiment that included a full part was the thick-to-thin experiment. The design of the experiment was to highlight the changing geometry of AM parts, and demonstrate the effects thermal behavior has on microstructure. The AM part has a large bulky section used for steady state analysis, and a thin section one-fifth the size of the bulk. The hatch strategy was rotated 90° every layer. In AM, parts often have a bulk infill section that leads to smaller extremities. This change in geometry affects the thermal behavior. Typically, the laser parameters are set to one speed and power regardless of part geometry, which appears in a build plan that lays out the laser path. In areas of smaller features, the part builds up heat rapidly because the time in between laser passes decreases. This causes parts to solidify at different rates due to the added thermal effect. Three different samples are fabricated at three different laser power settings of 225, 150, and 113 W, with a laser speed of 750 mm/s. This experiment assessed the ability of the sensors to detect changing thermal conditions initiated by different mechanisms: processing parameters and geometry. For this experiment, sensor data was analyzed and paired with material characterization to create a complete guide for understanding how LPBF behaves.

4.2 Physical Data

Multiple thick-to-thin experiments were performed to create a range of output values for the sensors, as well as material characterization. Figure 5.1 shows the design set up as well as the finished part. The design for the thick-to-thin was to create three different

samples with changing laser power, where it was expected they would contain different solidification rates. As a higher power is used, more thermal energy is added into the system which will affect the solidification rates as well as part quality.

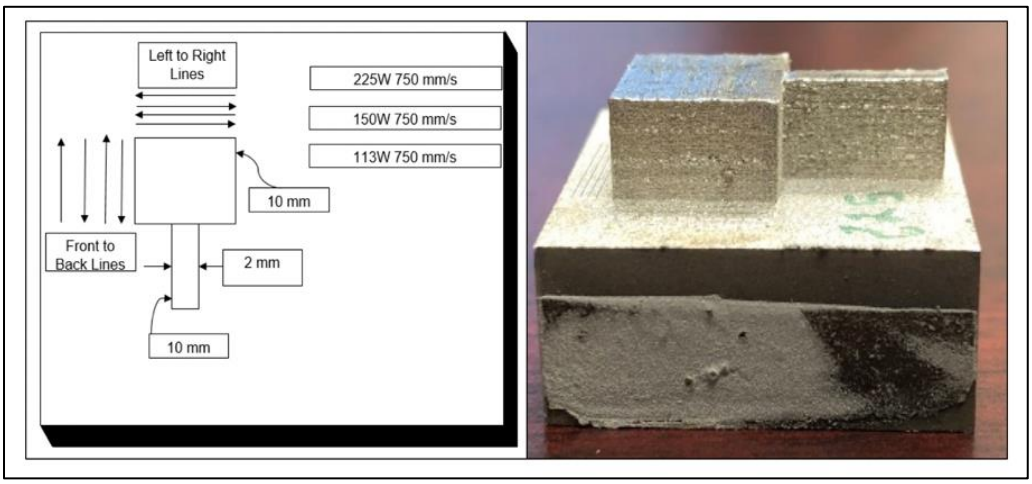

Figure 4.1: Left: Thick-to-thin schematic. Right: As build part for 225 W (45% power).

The three parameters used for this thick-to-thin experiment are seen in Figure 5.1, 225, 150, and 113 W, with a laser speed of 750 mm/s. These relatively low power levels help eliminate particle ejection. The layer thickness was also lowered to 30 µm. The smaller layer thickness ensured less powder on the substrate, increasing the consistency of the sensor readings. The speed of the experiment remained constant for all specimens to eliminate one variable for more consistent sensor data, and to see the effect on microstructure. Data was collected using the low-cost visible camera, high-speed camera, the spectroscopy photodiodes and the low-cost thermal camera.

The last variable eliminated for this experiment was the degree of rotation for the hatch strategy. Normally, LPBF uses a 67° hatch rotation to create higher quality parts because the laser never overlaps the same lines which can create rough surfaces. This was set to a 90° rotation instead because this creates much easier calculations when analyzing

the data. Figure 4.2 demonstrates the hatch strategy for the thick-to-thin experiment. During vertical scans the thick and thin sections experienced the same amount of time between laser passes. During horizontal scans, the thin section experiences a significantly lower amount of time between laser passes, while the thick section remains constant.

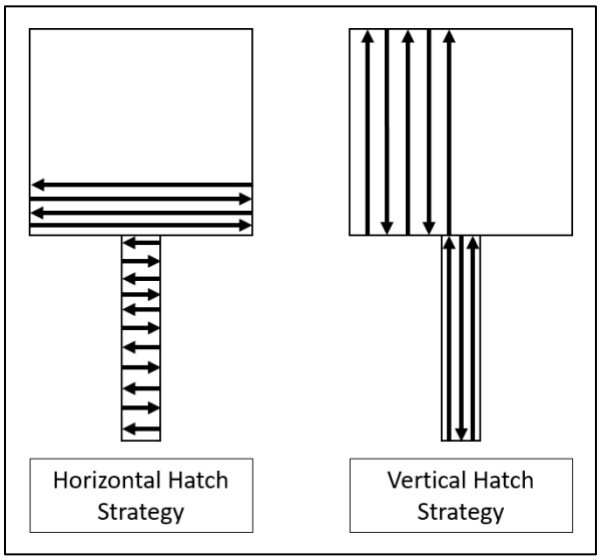

Figure 4.2: Example of horizontal and vertical hatching in the thick-to-thin experiment.

The hatch strategy also separates the two sections as if they were a separate part. This creates consistent data when the thick section is hatched completely followed by the thin section. The contour is the outline of the part that the laser will draw prior to the hatch, creating smoother part walls.

4.3 Results

4.3.1 Visible Camera

After conducting the thick-to-thin experiment, analysis of the sensors began with the visible camera. The preliminary results from the line experiments showed that the thermal and visible camera frame rate might be too low to collect meaningful data. Figure 4.3 represents the compiled data for the visible camera for all layers of the part. After quick

consideration, it was found that the visible camera would not be fast enough to represent the behavior of the part and melt pool. The only useful information collected by the visible camera was that it still shows the direction the laser is moving, and the orientation of the plasma plume as described in Section 3.3.1.1. Because of the lack of information shown by the visible camera, a different approach for using the sensor was applied in the future experiments, as described in Section 6.2.

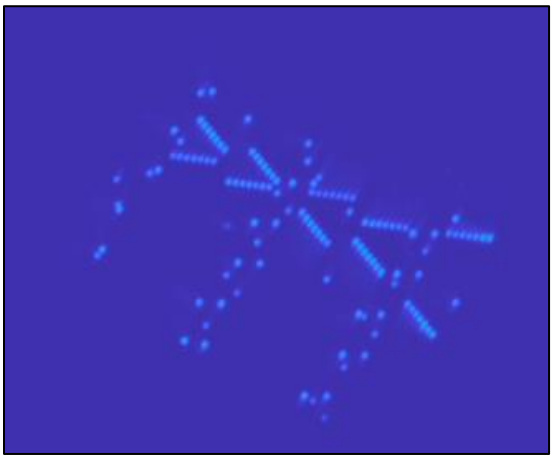

Figure 4.3: Visible camera frames compiled into one image demonstrating the low frames per second.

4.3.2 High-Speed Camera

The high-speed camera is only able to collect one layer at a time, and depending on the length of the layer, may not capture the entire layer. Data can only be collected for three seconds. After the data is collected, the writing of the data to a saved file takes approximately 6 minutes. One useful way to manipulate and analyze the data for the high-speed camera is to turn the pixel values into a broadband intensity graph. A broadband graph can be created by taking the total image information of each frame and converting the image into an intensity value, which takes the max value and area of the melt pool and

converts them into a number, then plotting the results as seen in Figure 5.3. This allows the high-speed camera to function similarly to the photodiodes. Collecting data over the broadband spectrum is beneficial because it captures all signatures.

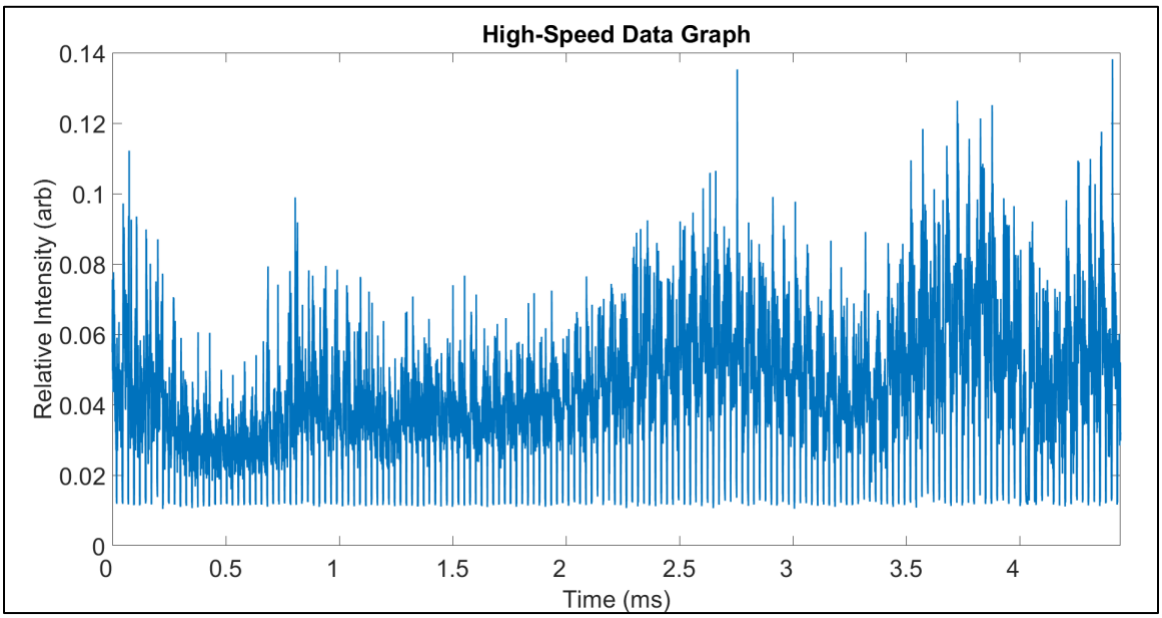

Figure 4.4: High-speed footage transformed into broadband intensity for layer 1 of the 225 W specimen in the thick-to-thin experiment.

The data collated by the high-speed camera normally appears as thousands of frames compiled into a video. These frames can be isolated and evaluated individually. The max value and area of the melt pool taken from the frames displays a reading that represents all wavelengths. This creates stronger signals because the entire visible spectrum is analyzed. The values taken from each frame are then combined in an array that allows them to be displayed in graphical form. Similar responses appear in the photodiode data with overall lower intensities because the photodiodes were focused on lower wavelengths.

4.3.3 Spectroscopy Photodiodes

The diode data collected for single beads is relatively simplistic because the time in between each laser line is one second, making the data easy to read. For the parts fabricated in this experiment, the diodes collected data over the hatching of the part as well as the contour. The contour is the outline of the part that the laser draws before the laser begins the hatch. The contour behaves similar to the single beads in that there is a single line drawn, while the hatch is more complicated. The hatching of the part is many lines drawn next to each other with little time in between. Therefore, dissecting the data to analyze the behavior of the plasma plume is difficult.

4.3.3.1 Variation in the Photodiode Data

Figure 4.5 represents several challenges associated with the diode data for a part. The first noticeable challenge is the different direction the laser travels to produce the hatch results in different intensity output, even though the thermal behavior of each hatch is theoretically the same. This is represented in the diode data as a shift in relative intensity, creating highs and lows depending on the laser direction. As the laser move towards or away from the sensor, the relative intensity shifts. This shift happens because the laser and melt pool potentially block some of the plasma plume data. These fluctuations potentially obscure the presence of a defect. The most accurate way to analyze the data would be to analyze each laser line strike and find the average intensity, then evaluate each line with the same average to determine if there are spikes due to defects. Figure 4.5 also illustrates the fluctuations, which are created when the area of the melt pool has increased. The melt pool area increases when process parameters are not optimal, such as variation in layer thickness, or an increase in energy density.

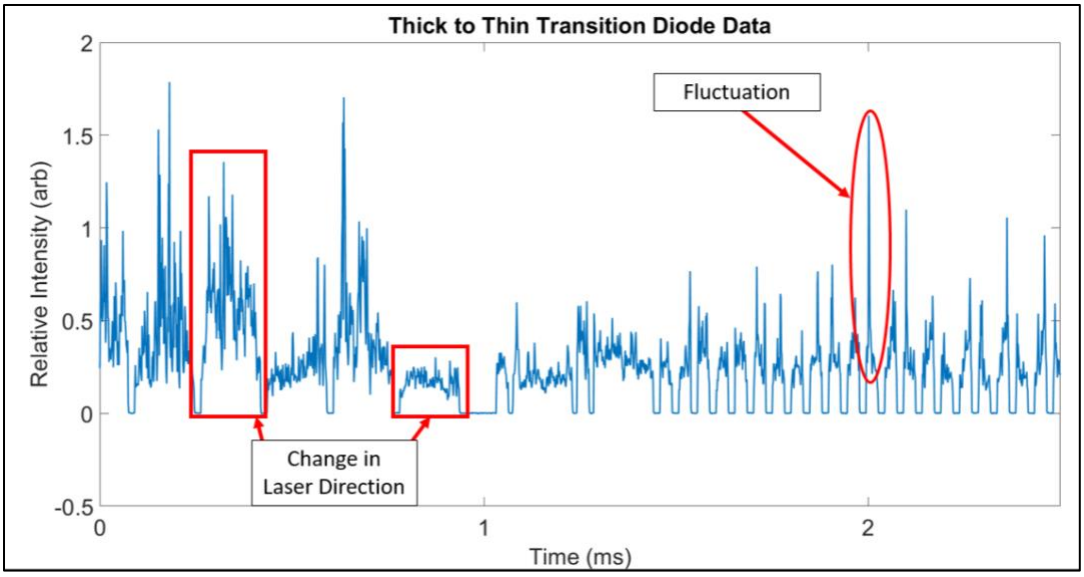

Figure 4.5: Analysis of photodiode behavior based on proximity to sensor and direction.

Creating a part is very different from the single beads because of the sheer amount of data that is collected. When collecting constant data over multiple layers, the files begin to accumulate, leading to overwhelming amounts of data. This is both beneficial because there is a good representation of each instance in the process, yet counterproductive because analysis and processing of the data becomes onerous. One simple yet powerful way to evaluate large amounts of diode data is to calculate relative maximums for each layer throughout the part. This will identify layers that have powder variation because the melt pool will increase in area when large amounts of powder is present. This approach does not identify defects that could appear due to key holing, because as stated in Section 1.4.2.1.3, larger energy density will appear lower in relative intensity in the diode data.

Figure 4.6 represents the dissection of the thick-to-thin specimens. The specimens were first cut along the vertical center line for a cross-section of the entire length. The next cuts were 3 mm away from the edge of the part. These cuts represent the cross-section of the thick and thin sections. Each part was then polished to 0.5 µm to be viewed for light

microscopy. The parts were then etched to reveal the microstructure, and viewed in a Scanning Electron Microscope (SEM) using Back Scatter (BS).

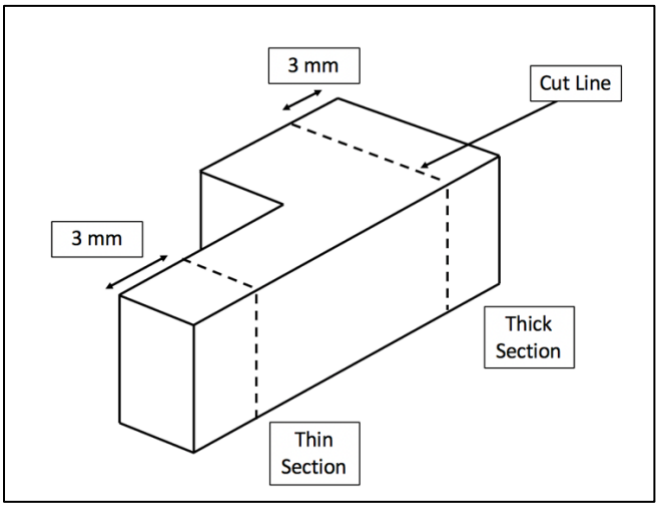

Figure 4.6: Cross-section of the thick-to-thin specimens.

Once images from the SEM and light microscopy are finished, then the comparison of the part quality and sensor data can be evaluated. Figure 5.5 evaluates the maximum values for each layer for the 113 W specimen. Accompanying the diode data is the cross section of the thick and thin parts. The thick section is represented on the left, while the

thin section is on the right. The specimen was cut horizontally in the thick section and in the thin section, 3 mm away from the edge.

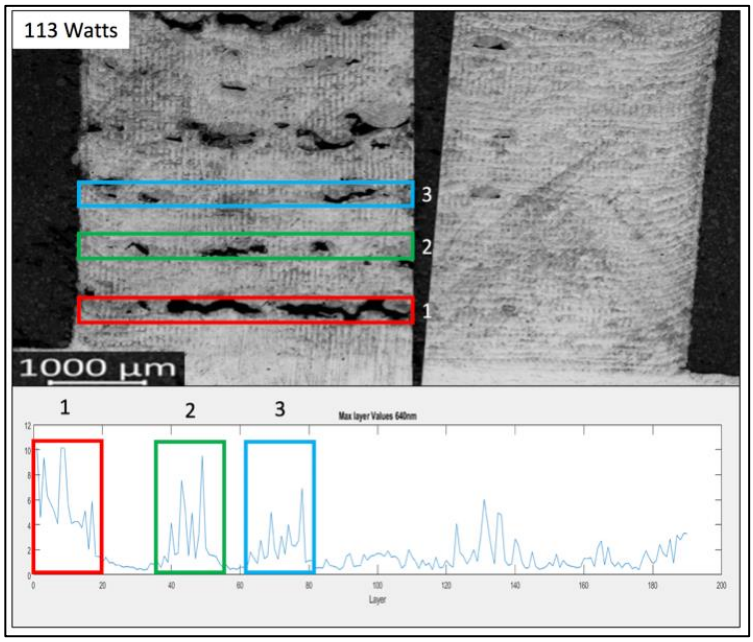

Figure 4.7: Defect analysis of the 113 W (25%) through photodiode data.

After viewing the cross section for the 113 W specimen, it is clear that the process parameters were not optimal. The areas in the part that appear black are pores in the part which are not ideal for LPBF parts. This leads to two major findings. The first is comparing the diode data to the cross section. In the cross section, every layer is accounted for meaning every layer has its corresponding diode data. After accumulating the max values for every layer and representing them in graphical form, it is clear to see that the diode data can accurately detect defects on every layer throughout the build.

Analyzing the max values gives an overview of layers that could have the potential for a defect. Figure 4.8 displays the diode data for layer ten of the 225 W thick-to-thin specimen. The data appears to behave similar to other layers except the large spikes that approach a relative intensity of ten. This high intensity is not normal during the build and

is an indication that the layer is potentially too thick. The diode data displays a thick layer because of the extremely high intensity that appears throughout the layer.

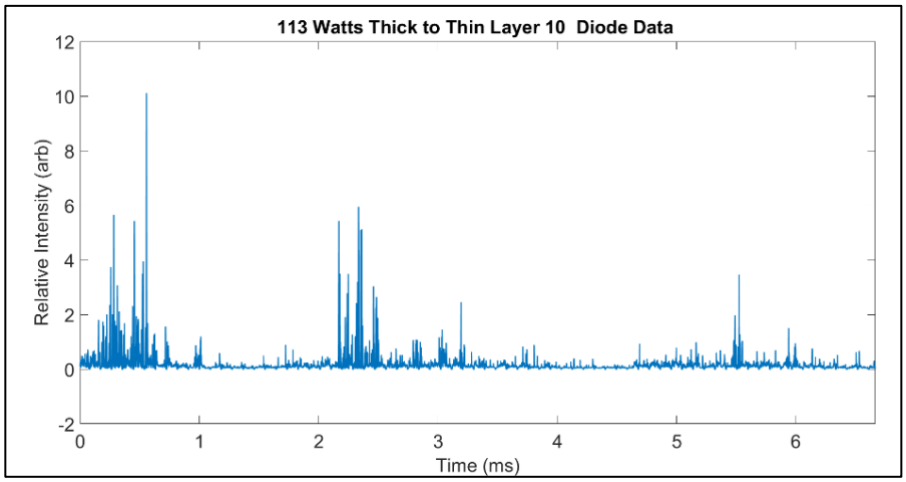

Figure 4.8: Diode data collected during layer 10 of the 113 W specimen.

The second major finding it that the thin section is relatively pore free. This result is due to the added thermal effect from geometry. The hatch strategy was rotated 90° every layer. This means that every vertical layer the thin section had the same thermal behavior, and every horizontal layer the thin section had increased thermal behavior due to a smaller hatch. In the layer where the hatch was horizontal, the thick section had 10 mm for the laser to travel before turning around a continuing the hatch, while the thin section only had 2 mm of travel before returning. With the speed of the laser at 750 mm/s, it would take 13 ms to travel 10 mm and 26 ms to travel back to the starting point, but for the thin section it would take 2.6 ms for the laser to travel 2 mm and 5.3 ms to return to the starting point. The time between laser overlap is significantly lower for the thin section leading to larger melt pools and longer solidification times.

Figure 4.9 continues the narrative that the parameters selected for the thick-to-thin specimens were subpar. However, the thin section appears less affected by the lower power

levels due to longer solidification times. As the power is increased from the 113 W case, pores appear less often throughout the build, without any large pores appearing in the thin section. This is a direct indication that there are high temperatures in the thin section.

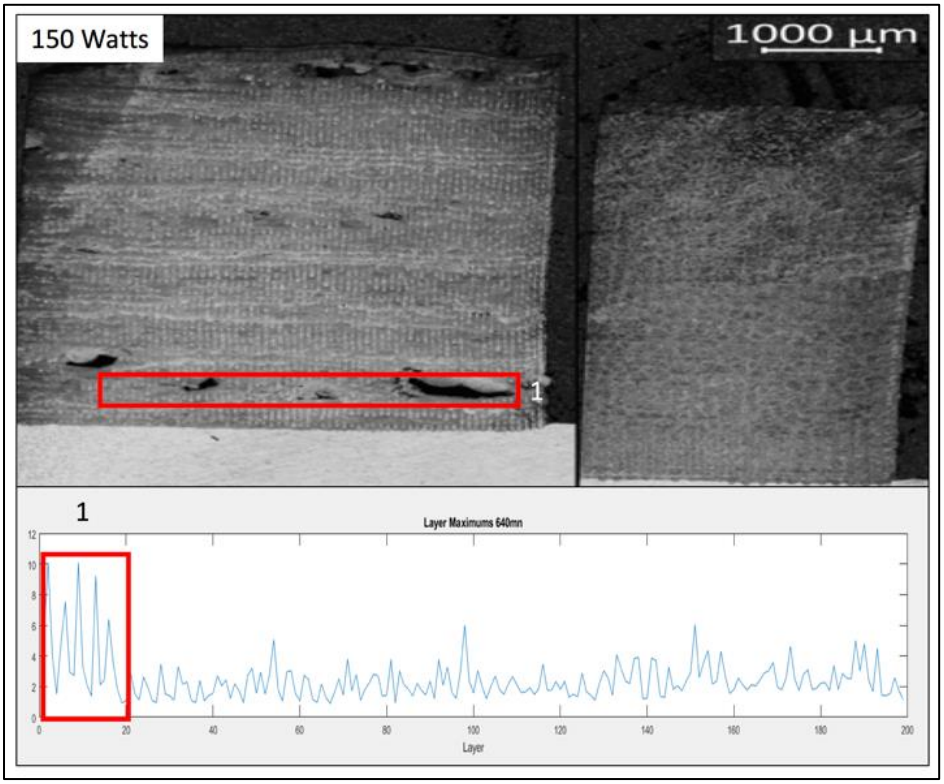

Figure 4.9: Defect analysis of the 150 W (30%) through photodiode data.

Again, the maximum values are a good indication of layers that need to be evaluated. Figure 4.10 analyses layer 10 of the 150 W specimen, which shows a similar result to layer 10 in the 113 W specimen. A majority of the layer appears to have a consistent spectral response, except for areas with extremely high relative intensities. The high intensities represent the melt pool growing rapidly, because the data is collected very fast and the high intensity is only a few points. The larger melt pool could be a layer defect or possibly a large particle ejection.

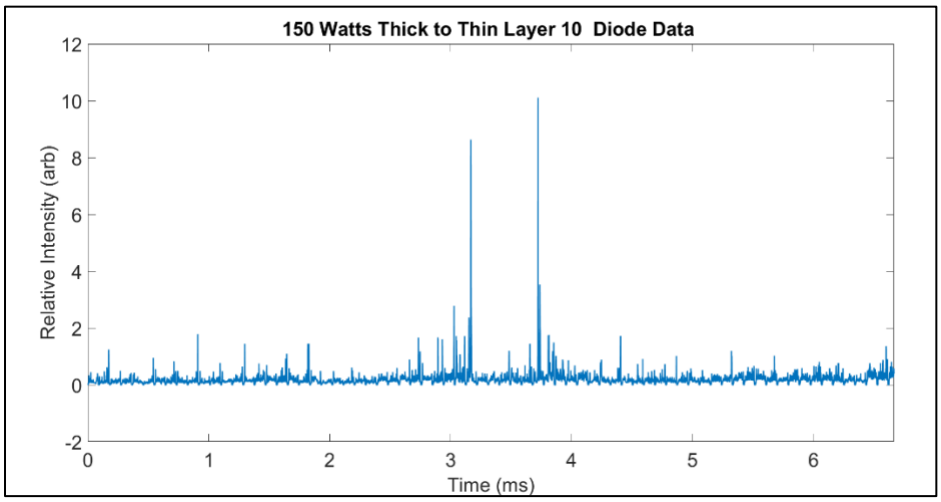

Figure 4.10: Diode data collected during layer 10 of the 150 W specimen.

The final specimen of the thick-to-thin experiment at a laser power of 225 W displays little to no pores in the thick section, illustrated by Figure 4.11. The diode data also suggests that there are few layers that have major defects. Once the clear identification of pores is no longer possible by the diode maximums, an evaluation of each layer is necessary.

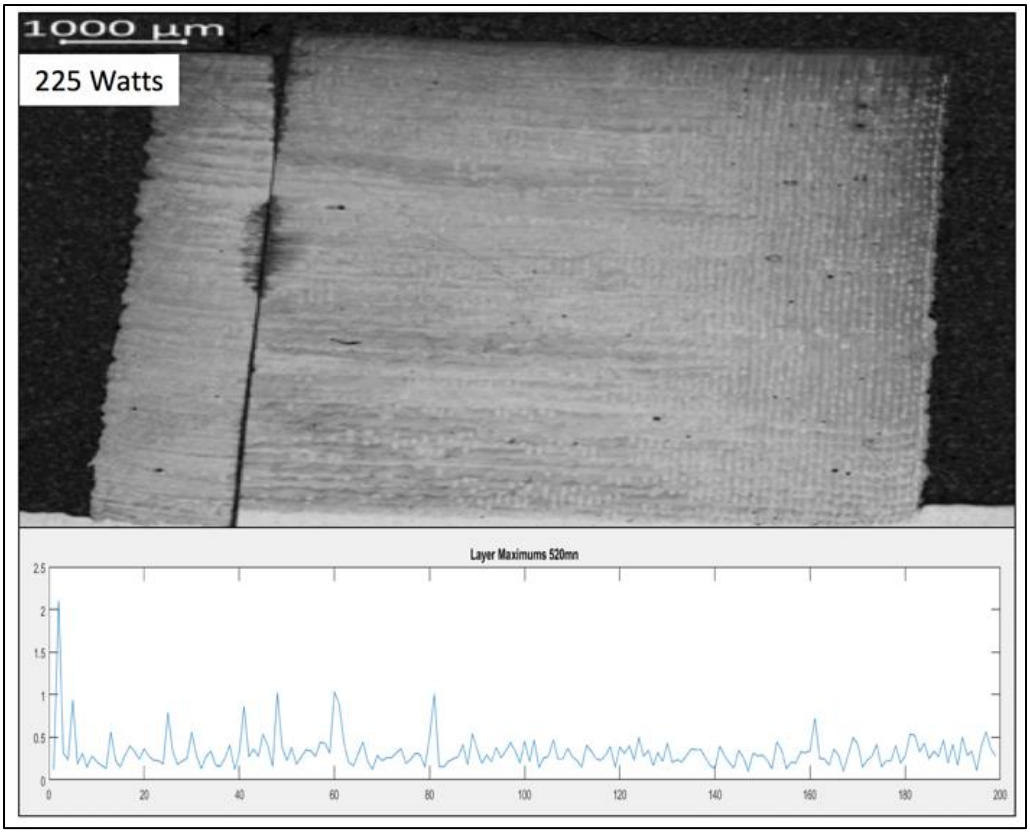

Figure 4.11: Defect analysis of the 225 W (45%) through photodiode data.

Continuing to analyze the diode data for the specimen, layer 10 of the 225 W specimen appears in Figure 4.12. The average relative intensity of this layer is drastically smaller than the other specimens. The relative intensity approaches four units while the other two specimens, 113 W and 150 W, approached ten units. This significant difference is a representation of proper parameters and optimal layer thickness.

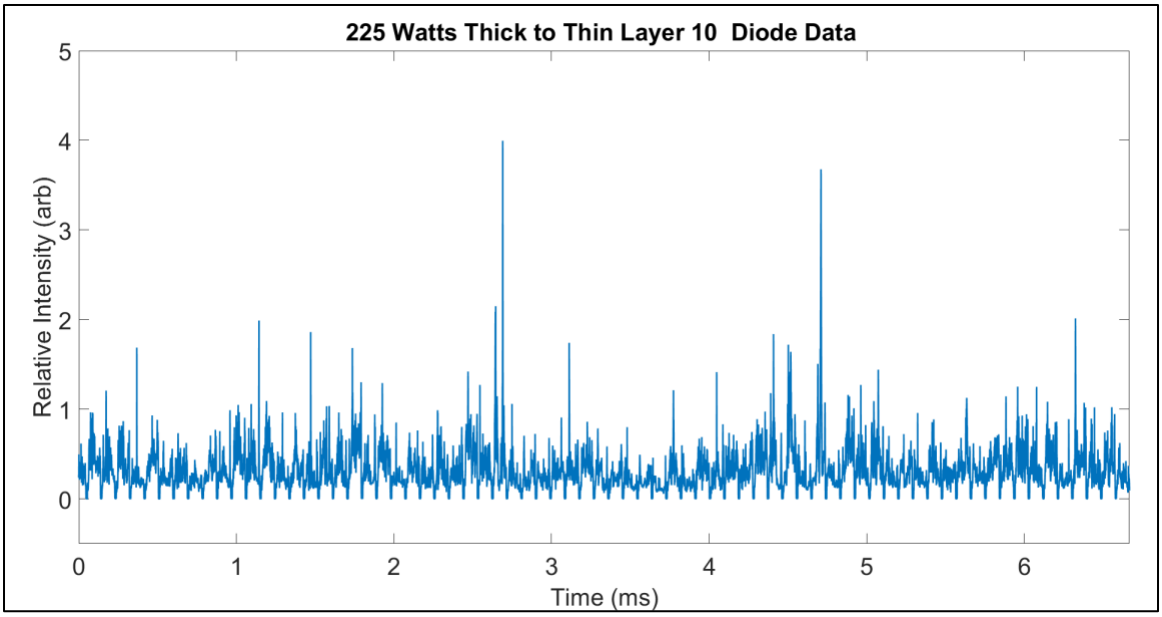

Figure 4.12: Diode data collected during layer 10 of the 225 W specimen.

The 225 W specimen appeared to have the best results for build quality; for this reason, the 225 W specimen underwent further material characterization.

4.3.4 Material characterization

After the completion of all thick-to-thin experiments, the specimens were cut and polished at the metallography facilities of the Air Force Research Laboratory. The 225 W specimen had the best results in terms of process parameters; therefore the 225 W specimen was further analyzed through material characterization. The 225 W specimen was analyzed at three different levels of magnitudes in a Scanning Electron Microscope (SEM) to view

the different grain orientations and microstructural growth. Figure 5.8 illustrates the first magnification of 500x.

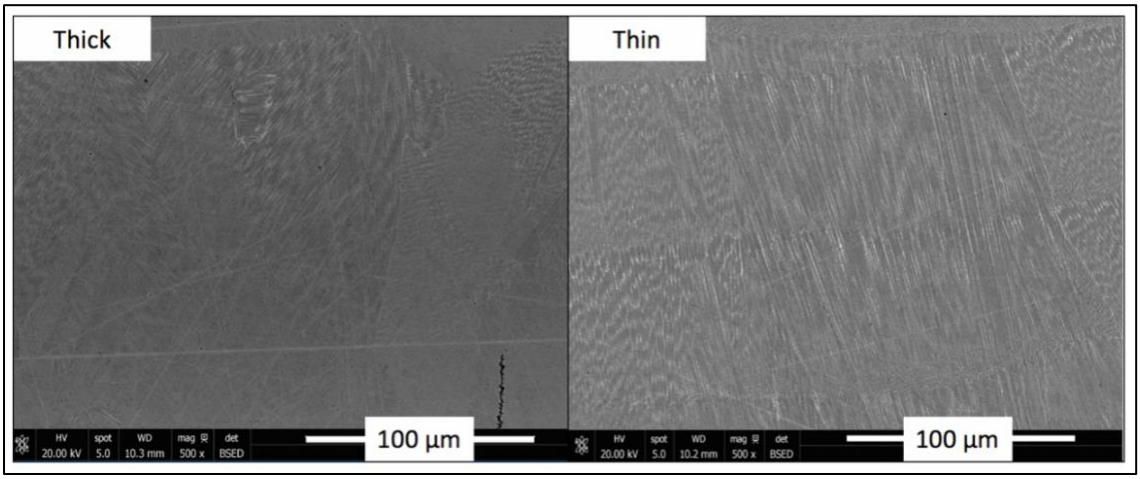

Figure 4.13: 100 µm scale image of the thick-to-thin experiment at 225 W.

The grain growth of the thick section appears to have many different orientations and grain shapes. The shapes of the grains are dependent on the location of the cutting and polishing. The dendritic structure is represented in both the thick and the thin sections. However, as the location of the cut changes, the orientation and shape of the grains will change to accommodate the change in location. The thin section shows a consistent orientation and grain shape. This is due to the time between laser scans increasing, leading to longer solidification times and higher temperatures. The thin section shows typical columnar dendritic growth in the build direction, which is expected of AM. The thick section shows many different orientations showing how the dendrites will follow the path leading to the most heat. In this case, with longer times between laser scans, the orientation will change depending on the direction of the laser. To analyze the microstructure a larger magnification is necessary. Figure 4.14 represents a magnification of 1000x.

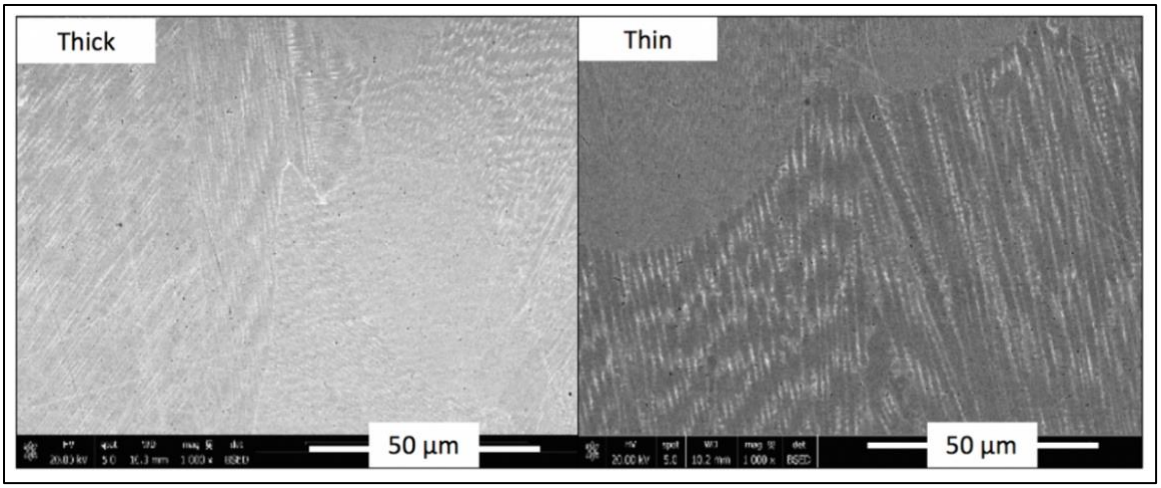

Figure 4.14: 50 µm scale image of the thick-to-thin experiment at 225 W.

Continuing the analysis of the thick section, the orientation of the dendrites is again indicative of the laser direction. The dendrite will grow in the build direction, however, due to a sectioning effect and how the part is cut and polished, the appearance of the microstructure has the dendrites going in many different directions. In Figure 4.14, the thick section shows the changing orientation of the dendrites as either vertically, growing in the direction of the build, or at an angle based on the sectioning effect. The thin section is responding to the changing time between laser scans. The time affects the amount of heat that builds in the part. For scans that are vertical, they will respond similar to the thick section because the dimension in this direction is the same as the thick section, while in the horizontal direction the dimensions are $1/5^{th}$ the size of the thick section. As the time between laser scans decreases, the melt pool size will increase, while as the time between laser scans increases the melt pool size will decrease. A larger melt pool results in longer solidification times. When dendrites have more time to solidify their growth increases in the horizontal direction, resulting in wider dendrites, the demonstrated in Figure 4.14. If the melt pool is small and the solidification time decreases the dendrites will not have as

long to grow, leading to much smaller dendrite growth. The change in solidification times and thus dendrite growth is better analyzed again, at a high magnitude.

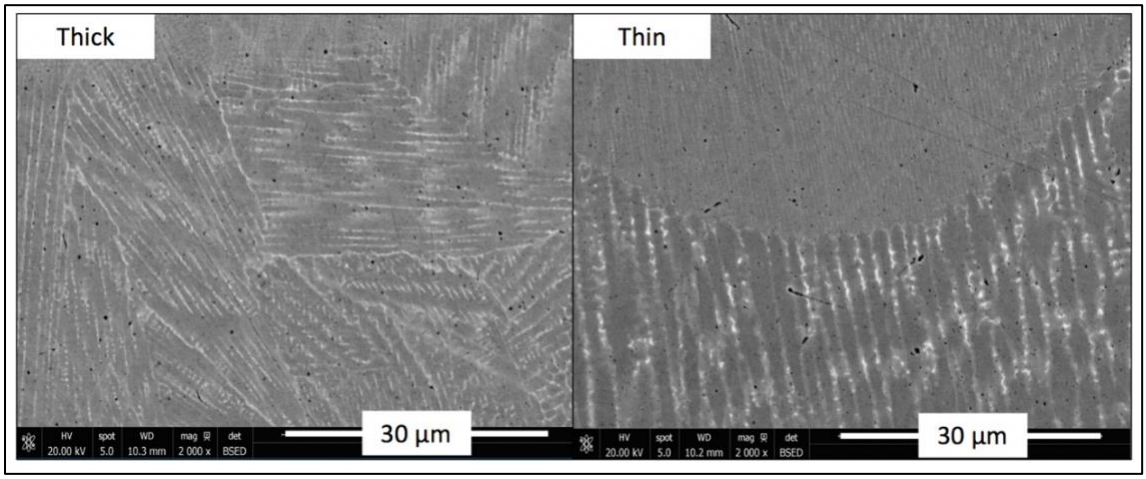

Figure 4.15: 30 µm scale image of the thick-to-thin experiment at 225 W.

Figure 5.10 strongly illustrates that changes in solidification time resulting in a change in the size of the dendrite growth. The thin section has two distinctly different dendrite sizes in close proximity. When the solidification time increases due to less time in between laser scans, the result is coarse, thick dendrites. When the solidification time decreases as a result of increased laser scan time, the dendrites solidify quickly into fine, thin dendritic growth. The thick section represents consistent microstructure and solidification times resulting on consistent dendrite growth. However, the thin section displays very fast solidification as well as slow solidification, depending on the rotation of the scanning, resulting in different size dendrites. Figure 5.11 demonstrates the change in time between laser scans with the diode data accompanied by the microstructure. The thick section is represented by a wider segment of relative intensity, while the thin section has very fast laser scans and much smaller intensity segments.

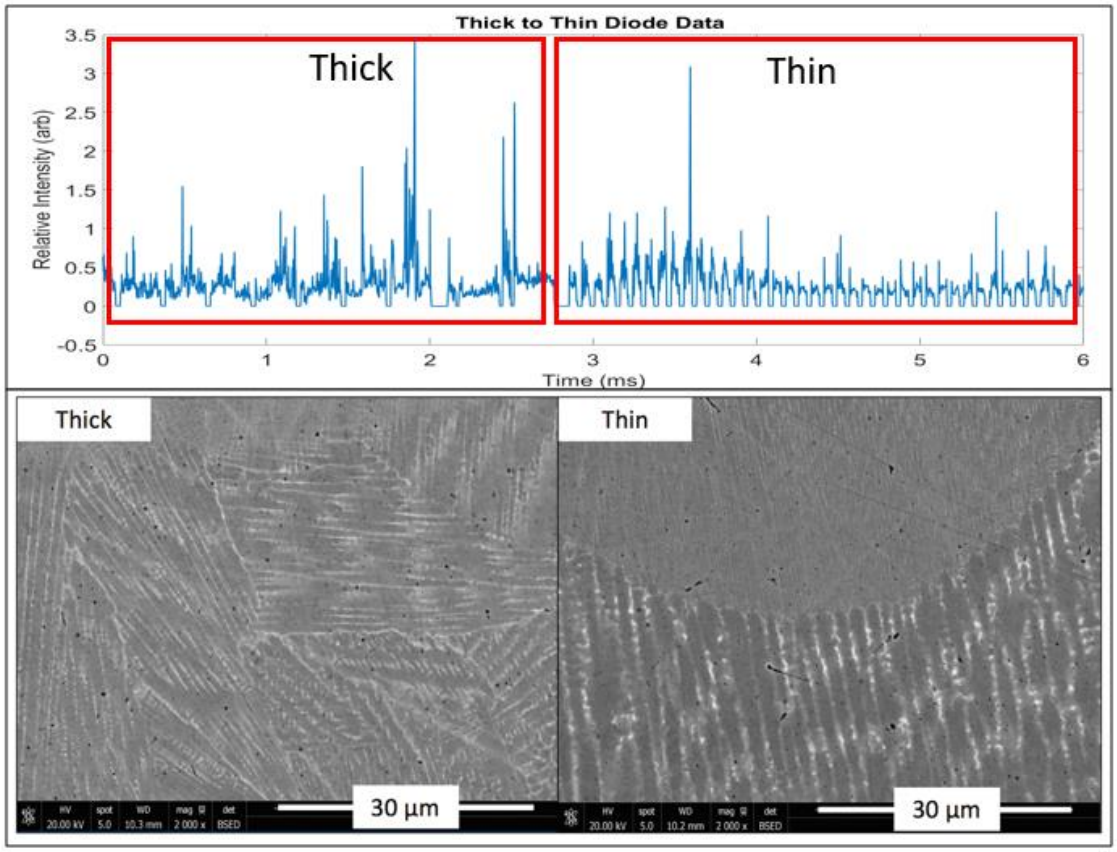

Figure 4.16: Comparison of thick-to-thin data and microstructure 225 W specimen at 2000x magnification.

The thin section of the diode data has a lower average intensity due to the deeper penetration of the melt pool. As stated in Section 3.3.1.3, as the melt pool penetrated deeper into the previous layer, the plume will also sink deeper into the part. This appears when key holing is present and is known as a capillary effect and occurs because of the melt pool pressure. With a smaller plasma plume the diode data will reduce in intensity, as shown in Figure 4.16.

4.3.5 Thermal Camera

The final significant finding and comparison is with the thermal camera temperature calculations and the microstructure of the 225 W specimen. Figure 4.17

represents the comparison between the thick and thin section's microstructure and temperature calculation. Many of the sensors are able to capture the difference in laser scan time, which is a main contributor to the solidification times of the material. Figure 4.17 displays strong evidence for the increase in temperature when comparing the thermal camera images with temperature calculations to the microstructure.

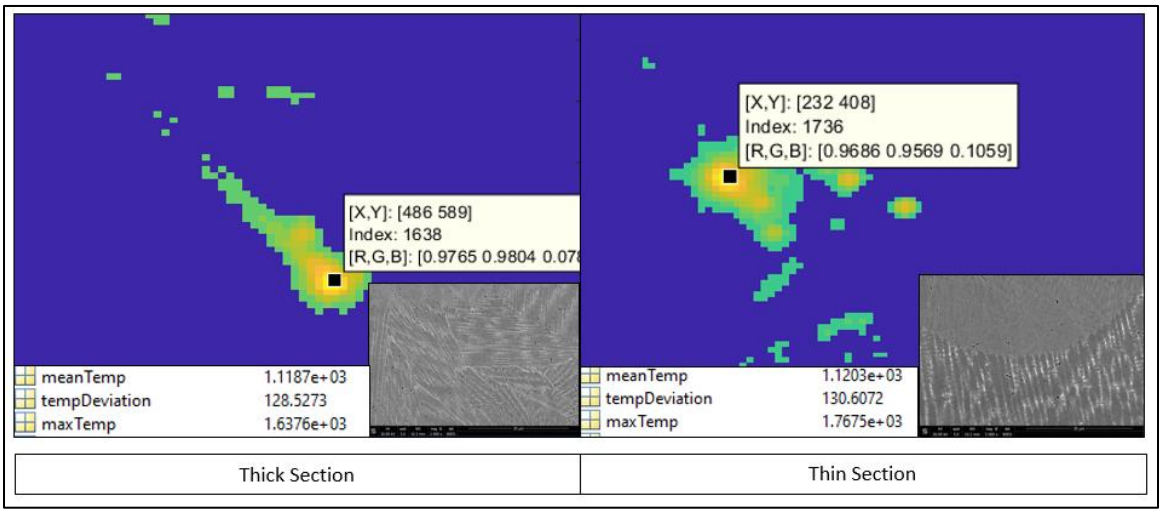

Figure 4.17: Temperature and microstructure comparison between the thick and thin sections.

The images of the melt pool were taken directly from the thermal camera images and processed through the temperature calculation software developed by UTC. The higher average temperature of the thin section results in a longer solidification time that affects how the microstructure forms. The process for acquiring the data to confirm the melt pools behavior requires and understanding of how the geometry effects the laser scan time, and how the laser scan time affects the solidification time, and finally how the solidification time affects the microstructure. Tracking these significant factors to monitor microstructure is possible through the multi-sensor approach.

4.4 Discussion

4.4.1 Effect of Part Geometry on Thermal Behavior

The geometry within a part affects the heat conduction, creating variations in the melt pool dimensions and temperature field. Depending on the process parameters and the geometry of the part, the melt pool will change. LPBF produces a part by melting the desired cross-section on every layer. To melt these areas a hatch strategy is used. A hatch strategy is the path the laser will take to melt the current layer. There are many hatch strategies that can be used, all have a different design and effect on how the layer is melted. In LPBF, a typical hatch strategy is stripes that rotate every layer. Stripes will divide the area of the part into tiles, which will be the width of the laser scan. The laser will travel along the tiles going back and forth creating the hatch strategy. This strategy does not consider geometry. For a simple cube, this will mean that the thermal behavior will change in the corners compared to the bulk material. Depending on the hatch strategy, the melt pool size will change. As the hatch rotates, there will be a layer where the strip will terminate in the corner of the cube. This decreases the time in between laser passes, which continuously heats the part until it eventually increases the melt pool [63] [64].

Geometry and processing parameters greatly affect the plasma plume. In areas that have progressively smaller geometry with the same process parameters, a thermal transition will occur. In the case of a cube, lines in the corners will have the same energy density as the bulk. However, the time between passes will decrease rapidly as shown in Figure 4.18. This adds heat to the part and creates a larger melt pool [63]. As temperatures rise in small part geometries, the microstructure will change in response.

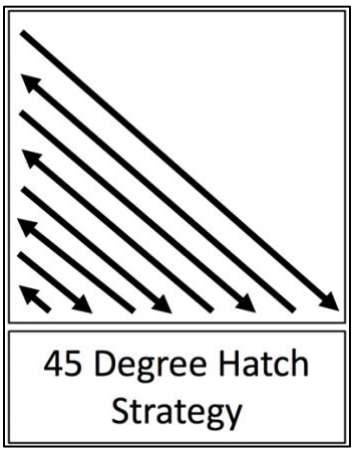

Figure 4.18: 45-degree hatch strategy.

As stated in the Microstructure section, the processing of alloy 718 is dependent on time and temperature. Changing one variable can change the microstructure of the part. Detecting the changes in temperature with the multi-sensor approach will result in the detection of microstructural changes.

In the thick-to-thin specimens, the dimension of the sections was different but both sections used the same process parameters. As the scan strategy changed every layer from horizontal to vertical, different thermal behavior began to appear. Looking at the light microscopy images of the thick-to-thin cross-sections, it was clear that the thick section had larger pores which are indicative of the process parameters. However, the thin section with the same parameters was pore free. This difference in part quality is a direct representation of how changing part geometry affects the thermal behaviors of the part.

4.4.2 Effect of Part Geometry on Microstructure

Chromium is the main wavelength detected when collecting multi-sensor data. The Microstructure section states that depending on the amount of chromium in alloy 718, and how the solidification occurs, the microstructure is affected. During an LPBF build, laser induced plasma is created that represents the species of metal that is being evaporated.

Given that the 3-color spectrometer is fixed on the behavior of the chromium wavelength, the output of the spectrometer gains insight into the possible phase transformations and microstructure solidification [64]. Other ways to identify possible microstructural behavior is through multi-sensor verification. In this process, more than one sensor determines the temperature for a melt pool. The temperature collaborates with the remaining sensors to create a proxy for the temperature of that layer. This propagates throughout the build. Taking the wavelengths in the infrared region and comparing them to the wavelength of chromium and broadband adds a thermal capability to the 3-color spectrometer. This, however, is not viable in all melt pools. Depending on the orientation of the melt pool and the orientation of the plasma plume, a direct comparison is inaccurate.

In the experiments containing the thick-to-thin specimens, an evaluation of the microstructure based on sensor data is confirmed. The photodiode data was able to capture layers of extremely high relative intensities that correlate with pores in the part. The thermal camera was able to compare the temperature on the thick section with the temperature in the thin section, with microstructural images to verify. The temperature in the thin section was 100 ° C higher than the thick section, which is directly related to the time between laser passes because both sections were using the same laser parameters.

4.5 Conclusion

The thick-to-thin experiment is designed to show the difference in thermal behavior depending on part geometry and processing parameters. Areas of smaller features will have less time in between laser passes, which will have a larger effect on the temperature of that local area. In areas of smaller parts and larger heat, the microstructure of the part will change. Based on the behaviors of solidifying metal, the longer the molten metal has to

solidify the larger the grain structure. This behavior was shown in the sensor response. In the thin section, the photodiodes collected data that was lower in relative intensity than the thicker bulk sections. This is indicative of the change in geometry leading to larger solidification times. The photodiodes and thermal camera were able to identify that the thin section has higher temperatures and longer solidification times, leading to a larger melt pool and larger grains.

Chapter 5: Spectral Power Threshold

5.1 Introduction

An Acton grading spectrometer gives data for a range of spectral wavelengths. This data can be used to guide which wavelengths the 3-color spectrometer approach will use. A different intensity response from the Acton spectrometer is directly correlated with the number of photons that are emitted during LPBF. With higher power, more photons will be released leading to a much stronger signal. With a stronger signal present, fluctuations in the signal will then give some insight into the quality of the part. If a strong signal is not present, the sensing method is not suitable for the detection of defects. This experiment systematically reduced the power level to determine the number of photons released, which helped determine the sensitivity of this process monitoring technique when compared to the processing parameters used. A minimum threshold of power was determined to find a domain where enough photons released adequately represented the quality of the LPBF builds.

The first Acton spectrometer experiment performed by UTC prior to the beginning of this work gave results that the main wavelengths seen with strong spectral signatures in

alloy 718 are 422 nm, 455 nm, 520 nm, and 530 nm. Figure 6.1 illustrates the results of the Acton spectrometer readings.

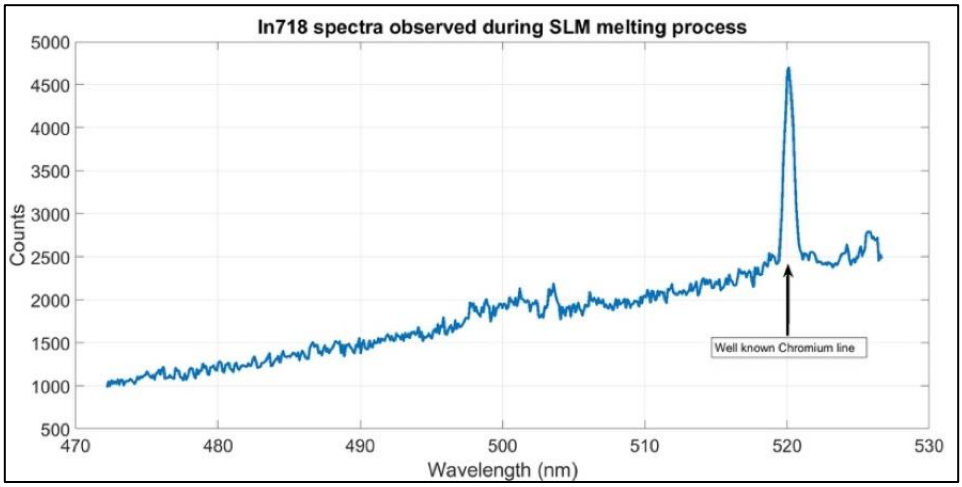

Figure 5.1: Original Acton experiment at 400 W (80%) and 1000 mm/s [52].

In Section 2.1.1.5, a review of the different temperature calculation of spectroscopy reveals that taking the ratio of two wavelengths can create a proxy for the changing temperature in LPBF. For this process, two wavelengths of strong spectral signal were used to collect data, which was used as a ratio for the change in temperature. The theory behind the temperature proxy is that when two wavelengths are used to evaluate the build, the wavelengths will fluctuate at different rates. Therefore, the ratio (or difference) between the wavelengths will indicate the change in temperature. In order for the temperature proxy to be accurate, the data must be equal in intensity. This is challenging because due to Planks distribution of blackbody radiation, the intensity will increase with increasing wavelength. Therefore, the two wavelengths will not have the same intensity. To eliminate the

difference in intensity for the ratio of the two wavelengths to be possible, specific calibration is preformed, as stated in Section 2.1.1.6.

Similar to Figure 5.1, each wavelength that was chosen for the 3-color spectrometer approach appears in the Acton spectrometer data as a strong signal. The parameters of the original Acton spectrometer experiment were 400 W (80% power) and 1000 mm/s scan speed and a powder layer thickness of 50 µm. The single beads and thick-to-thin experiments used parameters that were at lower powers because the layer thickness was decreased to 30 µm. During these experiments, the spectral signatures did not behave as predicted. Therefore, a new experiment with the Acton grading spectrometer was performed.

5.2 Approach

The new Acton spectrometer experiment is used to define the power threshold for the spectral signals in LPBF. The Acton grading spectrometer data was collected for a 10 mm x 10 mm cube, with a rotation strip hatch strategy. The rotation of the hatch was set to 45 degrees and data was collected every layer that was horizontal and vertical. The Acton grading spectrometer collected sixty frames of data that was focused on 520 nm. Only the 520 nm wavelength was considered because when the focus was shifted to the 530 nm wavelength, there was no signal even at max power. The 520 nm wavelength signal was the only signal that appeared in the experimental set up. As the build progressed away from the substrate, data was collected at different power levels. Starting at max power and working down to very low power, the Acton grading spectrometer data evaluated the spectral signal of alloy 718.

5.3 Results

The first experiment adjusted the power levels to define the threshold for the spectral signals. Figure 5.2 demonstrates the number of counts received at the 520 nm wavelength at 500 (100%), 400 (80%), 375 (75%), 300 (60%), 250 (50%), and 175 (35%) W. The counts are the number of photons collected by the Acton grading spectrometer. More counts are a result of high power causing more photons to be released.

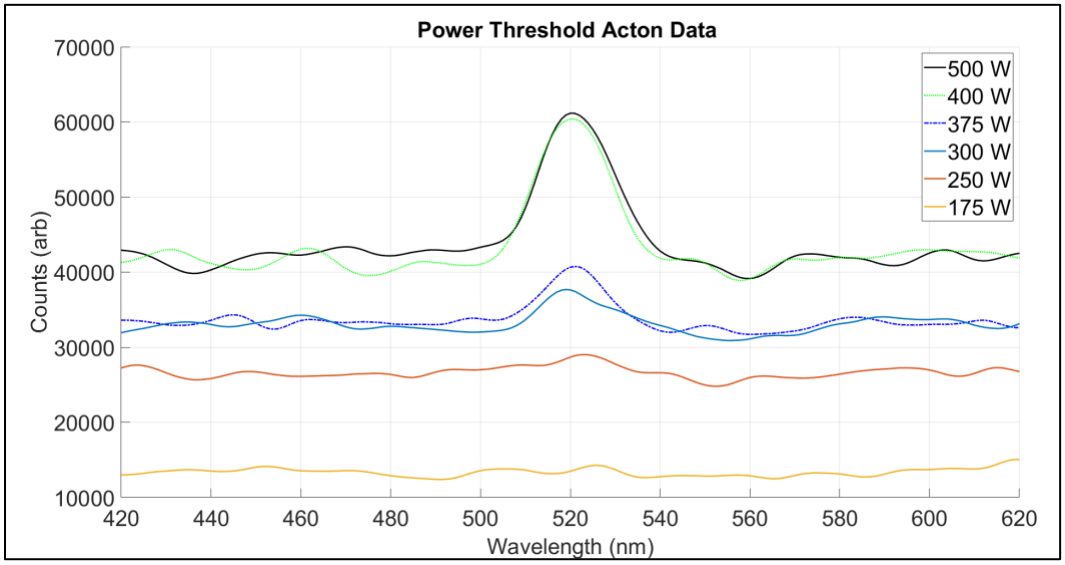

Figure 5.2: Acton Data response of variable laser power at 750mm/s.

When decreasing the power level below 300 W (60% power), the difference between noise in the system and the spectral signal become increasingly similar. When comparing the signals found at 375 W (75% power), the spectral signal is abundant, however once the threshold is crossed into the lower power region of 300 W (60% power), the signal begins to drop off significantly. The signal continues to decrease until the point where the signal and the noise are indistinguishable, such as the 250 W (50% power) line. This point, and arguably sooner, the signal is not strong enough to provide any indication of the part quality.

5.4 Conclusion

The results from the second Acton spectrometer experiment display the threshold of power that establishes a strong spectral signal. To evaluate the part quality, 375 W (75% power) or high is preferred to collect adequate signals. Based on these results, the experiments that used power levels below the threshold are not able collect spectral signatures that are strong enough to indicate part quality. This does not suggest that the information gained through the lower power experiments is not beneficial, only that the ability to ratio the wavelengths is lost. The power threshold determined in this chapter adds new knowledge of the spectral response, creating more accurate experimental designs leading to desired results from the photodiode data.

Chapter 6: Spectral and Thermal Mapping

6.1 Design of Experiment

The big-to-little experiment combined the knowledge gained after the second Acton spectrometer experiment and the new techniques of manipulating the photodiode data to create a spatial representation of the diode data with a power level above the known threshold for spectral response. The big-to-little experiment took design strategies from the thick-to-thin experiment with one major change. The small section was detached from the big section and transformed into a square to simplify the calculations. The goal of the experiment was to take the known length and width of the part and combine that with the known speed to calculate the number of data points collected in each laser line. This data was then mapped spatially to create a comprehensive view of the layer. This combined with the other sensor created a vastly superior experiment that demonstrated the effect geometry has on the microstructure. The parameters selected for this experiment were 750 mm/s and 400 W (80%) power. The power level was high above the threshold for spectral response to guarantee the signature of chromium was visible in the diode data.

6.2 Sensor Data Analysis

The hatch strategy of the build was on a 45° rotation every layer. This means that every other layer there was a straight line across the part. This simplified the calculation for the diode spatial map. However, the layers where the hatching is on a 45° angle had the effect of geometry on microstructure appear. Figure 6.1 visually represents the 45° angel.

The contour is visible in the beginning of the graph, then the laser scan started the hatch. It is noticeable to see the very fast hatching of the corners that open to the bulk of the part and the longest scan times.

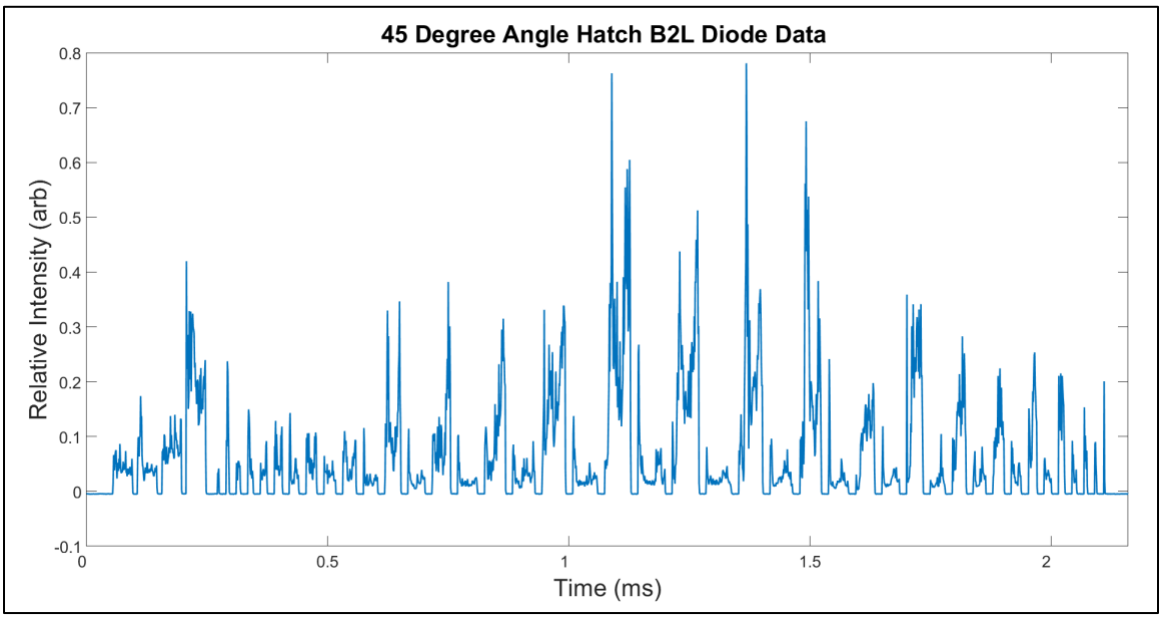

Figure 6.1: The third layer of the 3mm x 3mm section at a 45° angle. The photodiode data captures the change in geometry and relates that to temperature.

The hatch strategy plays a major role in the part quality as well as microstructure development. The fast laser scans in the corners build up heat that attracts powder particles outside of the part to join the melt pool. This phenomenon causes the corners of the part to swell and increase the height of the corners above the powder level. This results in a layer with no powder on the corners due to the swelling. The swelling is represented in the thermal data. Figure 6.2 represents the complete melt pool database for one build. The melt pools do not cover the entire part due to the frame rate of the camera and the exposure time. The reason for this is to be able to calculate temperature accurately.

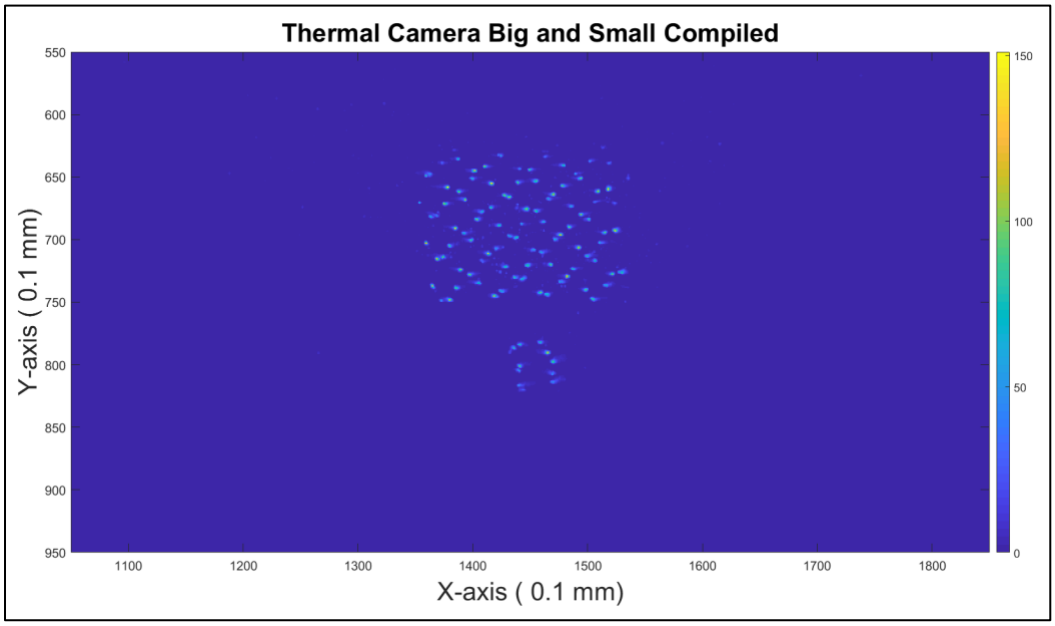

Figure 6.2: Thermal data compiled for Layer 220.

It is possible to extend the exposure time to include more of the laser scan into the image and temperature calculations; however, the calculations become significantly more difficult to accurately represent the melt pool temperature. For this reason, only partial layer melt pool information is used.

Finally, the last ability of the multi sensor approach is the mapping of the diode data. The long exposure time of the visible camera helps determine the topology of the parts surfaces each layer. This information is used in unison with the diode data to help create a reasonable image of the surface based on the diode data. Figure 6.3 displays the long exposure time visible camera data for layer 220 of the big-to-little experiment.

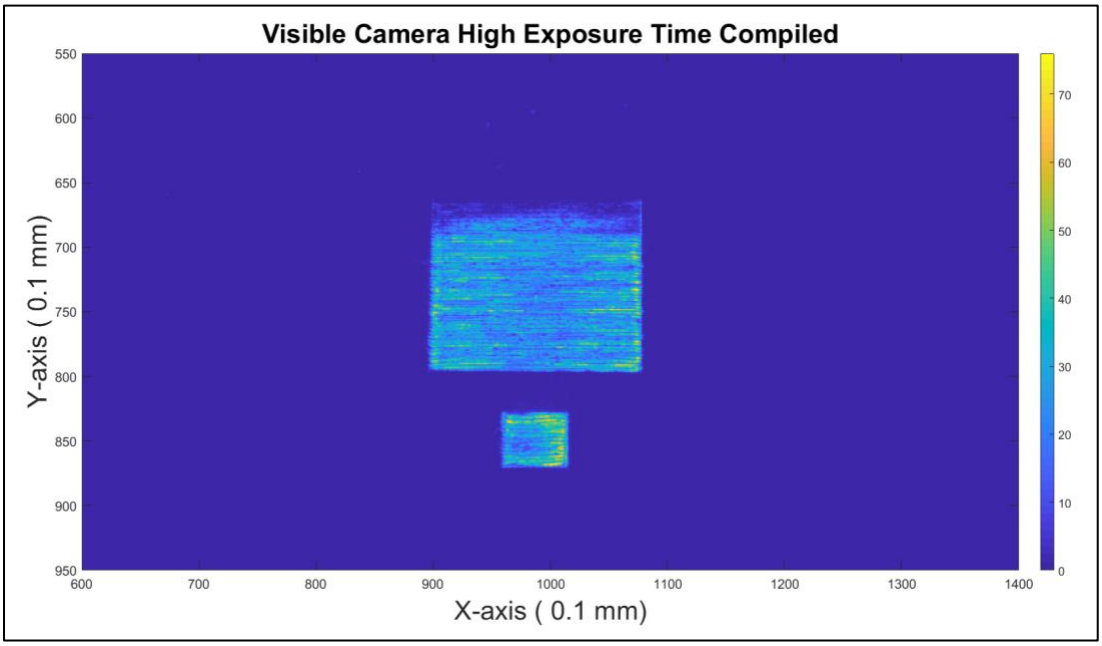

Figure 6.3: Compiled visible camera data for Layer 220 of the big-to-little build.

The long exposure time is able to determine the intensity of the melt pool over a period of 13500 µs. During that time, the light from the melt pool was recorded in the visible camera each frame. The frames were stitched together to produce a complete layer. The diode data was stitched together in a similar manor. Figure 6.4 represents the stitched diode data for the big section and little section in this experiment. When comparing the diode data map with the long exposure visible data it is clear that much of the data is consistent with the visible camera. The strips in the diode data represent the change in direction of the laser, either moving closer to the sensor or away.

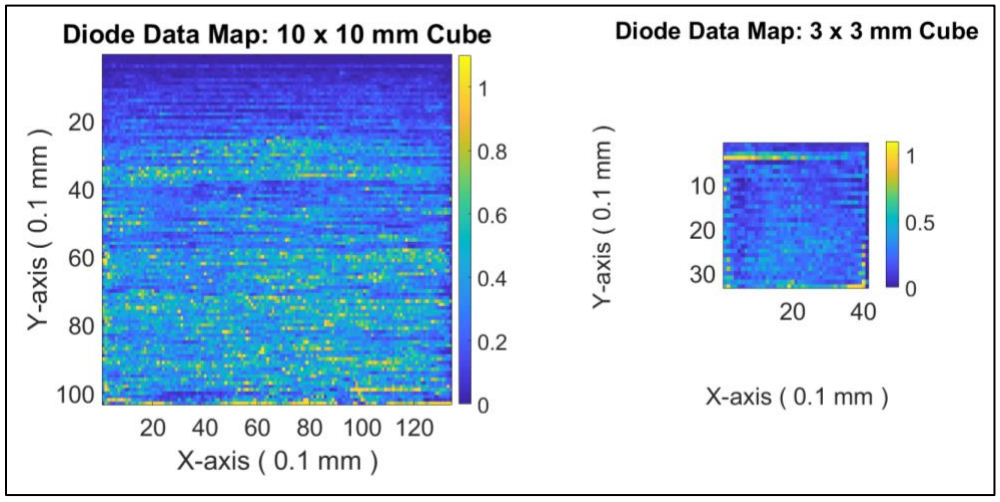

Figure 6.4: Diode data mapped spatially to represent the high intensity points of the big-to-little experiment reflected in the visible and thermal data.

6.3 Conclusion

Fluctuation in the diode data appear because a change in the system occurs. The little section displays higher overall intensity throughout the build. In Figure 6.4, the high temperatures calculated with the thermal camera are correlated with the diode data. With the results from the data, it is possible to monitor the temperature of a LPBF build with a multi sensor approach. To continue this research, the material characterization of the big-to-little experiment will display the changes in microstructure already observed. Computer Tomography (CT) scans will display the location of possible defect. The sensor data will then be analyzed to determine of the location of the defects is represented in the data.

Chapter 7: Conclusion

In this work, an approach to determine the effects geometry has on the microstructure of LPBF build part has been reviewed. The sensors used for this work were one visible camera, one thermal camera, one high-speed phantom camera, and three photodiodes focused on three wavelengths: 520 nm, 530 nm, and 640nm. The following conclusions have been made:

1. The photodiodes accurately recorded the behavior of the plasma plume. The behavior of the laser is captured in the diode data, revealing changes in direction, power, speed, and melt pool area.
2. The thermal camera calculations determine the change in temperature between melt pools. The change in geometry delivers larger hotter melt pools that are captured and confirmed by the thermal camera.
3. The high speed and visible cameras capture the topology of the surface, while extended exposure times create a complete image of each layer's surface.
4. The single beads experiment determined that the direction of the laser changes the relative intensity of the photodiode data. The topology of the plate significantly affects the photodiode data response leading to very sensitive sensor calibration. The single beads also determined how the change in parameters affects the sensor response, creating a full understanding of the sensor's capabilities.
5. The thick-to-thin experiment created a geometrical change in the part with constant parameter. This results in longer times in between scan speeds for the bulk section and vastly short scan speeds times in thin extremities. The result

was a larger thermal gradient and microstructural differences, both determined by the multiple sensors collecting data.

6. The big-to-little experiment explored the possibilities of diode data spatially mapped to determine the effect of defects and geometry on the microstructure of a LPBF part. More work is needed to complete the experiment and data analysis.

Chapter 8: Future Work

8.1 Big-To-Little Continuation

The work in Chapter 5:Spectral Power Threshold was left incomplete. The work of this entire thesis has been culminated into the final big-to-little experiment. The work that still needs to be completed is:

1. CT scans of the part to determine the anomalies that could appear due to process parameters and thermal behavior.
2. Thermal mapping needs to be completed for the thermal camera data. Thermal metrics such as max melt pool temperature and melt pool with should be graphed to show the relationship between melt pool metrics and each layer to determine the evolution of the melt pool during a build.
3. The diode data needs to be mapped for each layer which will create a CT-like scan showing the valleys and peaks during each layer.
4. Once the data has been thoroughly evaluated, it should be compared to the CT scans and to any other material characterization.
5. By comparing the sensor data, it should be possible to determine a location of a defect and compare that to known defect locations.

The data collected during the build is sufficient to complete the analysis of the big-to-little experiment.

WORK CITED

[1] X. Wang, M. Jaing, Z. Zhou, J. Gou and D. Hui, "3D printing of polymer matrix composites: A review and prospective," *Composites Part B,* vol. 110, no. 2017, pp. 442-458, 2016.

[2] T. Ngo, A. Kashani, G. Imbalzano, K. T. Nguyen and D. Hui, "Additive manufacturing (3D printing): A review of materials, methods, applications and challenges," *Composites Part B ,* vol. 143, no. 2018, pp. 172-196, 2018.

[3] W. E. Frazier, "Metal Additive Manufacturing: A Review," *Journal of Materials Engineering and Performance,* vol. 23, no. 6, pp. 1917-1928, 2014.

[4] D. D. Gu, "Laser additive manufacturing of metallic components: materials, processes and mechanisms," *International Material Review,* vol. 57, no. 3, pp. 133-164, 2012.

[5] N. Shamsaei, A. Yadollahi, L. Bian and S. M. Thompson, "An overview of Direct Laser Deposition for additive manufacturing; Part II: Mechanical behavior, process parameter optimization and control," *Elsevier,* vol. 2015, no. 8, pp. 12-35, 2014.

[6] M. J. Donachie and S. J. Donachie, Superalloys: A Technical Guide, Metal Park, OH: American Society for Metals, 2002.

[7] P. S. Technologies, "Material Specifications," 2016. [Online]. Available: http://www.praxairsurfacetechnologies.com/-/media/corporate/praxairsurface/us/documents/brochures/truform-718-metal-powder.pdf?la=en. [Accessed 28 November 2018].

[8] E. Petersen-Overleir, "Effect of 3D Printing on the Microstructure and Mechanical Properties of an Inconel 718 Nickel-alloy," University of Stavanger, Stavanger, 2015.

[9] M. Moiz, *The Influence of Grain Size on the Mechanical Poperties of Inconel 718,* Linkoping: Linkoping University, 2013.

[10] X. Wang and K. Chou, "Effects of thermal cycles on the microstructure evolution of Inconel 718 during selective laser melting process," *Elsevier,* vol. 18, no. 2017, pp. 1-14, 2017.

[11] J. Brooks and P. Bridges, *Metallurgical Stability of Inconel Alloy 718,* Birmingham: The Metallurgical Society, 1988.

[12] S. Sui, J. Chen, E. Fan, H. Yang, X. Lin and W. Huang, "The influence of Laves phases on the high-cycle fatigue behavior of laseradditive manufactured Inconel 718," *Materials Science & Engineering A,* vol. 695, no. 2017, pp. 6-13, 2017.

[13] A. Devaux, L. Naze, R. Molins, A. Pineau, A. Organista, J. Guedou, J. Uginet and P. Heritier, "Gamm Double Prime Precipitation Kinetic in Alloy 718," *Material Science and Engineering A,* vol. 486, no. 2007, pp. 117-122, 2007.

[14] S. Guo, W. Sun, D. Lu and Z. HU, *Effects of Minor Elements on Microsturcutre and Mechanical Properties.*, Shenyang: The Minerals, Metals, and Materials Society, 1997.

[15] Y.-L. Kuo, S. Horikawa and K. Kakehi, "The effect of Interdendritic Delta Phase on the Mechanical Properties of Alloy 718 Built up by Additive Manufacturing," *Materials and Design,* vol. 116, no. 2017, pp. 411-418, 2016.

[16] L. Valle, L. Araujo, S. Gabriel, J. Dille and L. Almedia, "The Effect of Delta Phase on the Mechanical Properties of an Inconel 718 Superalloy," *Journal of Material Engineers and Performance,* vol. 22, no. 5, pp. 1512-1518, 2013.

[17] S. Azadian, L.-Y. Wei and R. Warren, "Delta Phase Precipitation in Inconel 718," *Material Characterization,* vol. 53, no. 2004, pp. 7-16, 2004.

[18] M. Sandararaman, P. Mukhopadhyay and S. Banerjee, *Carbide Precipitate in Nickel Based Superalloy 718 and 625 and their Effect on Mechanical Properties,* Mumbi: The Minerals, Metals, and Materials Society, 1997.

[19] B. Rogers, *Microstructure Development in Direct Laser Sintering Inconel Alloy 718,* Tempe: Arizona State University, 2017.

[20] Impress, "ESA," 2018. [Online]. Available: http://www.spaceflight.esa.int/impress/text/education/Mechanical%20Properties/Dislocations_02.html. [Accessed 1 12 2018].

[21] S. K. Everton, M. Hirsch, P. Stravroulakis, R. K. Leach and A. T. Clare, "Reviee od In-Situ Monitoring ansd In-Situ Metrology for Metal Additive Manufacturing.," *Materials and Design,* vol. 95, no. 2016, pp. 431-445, 2015.

[22] S. Tammas-Williams, H. Zhao, F. Leonard, F. Derguti, I. Todd and P. Prangnell, "XCT analysis of the influence of melt strategies on defect population in Ti–6Al–4V components manufactured by Selective Electron Beam Melting," *Materials Characterization,* vol. 102, no. 2015, pp. 47-61, 2014.

[23] R. Li, J. Liu, Y. shi, L. Wang and W. Jaing, "Balling behavior of stainless steel and nickel powder during selective laser melting process," *Internation Journal of Advanced Manufacturing Technology,* vol. 2012, no. 59, pp. 1025-1035, 2012.

[24] M. F. Zaeh and G. Banner, "Investigations on residual stresses and deformations in selective laser melting," *Prod. Eng. Res. Devel.*, vol. 4, no. 1, pp. 35-45, 2010.

[25] Q. Jia and D. Gu, "Selective Laser Melting Additive Manufacturing of Inconel 718 Superalloy parts: Densification, Microstrucutre and Properties," *Journal of Alloys and Compounds,* vol. 585, no. 2014, pp. 713-721, 2013.

[26] F. Lui, X. Lin, C. Huang, M. Song, G. Yang, J. Chen and W. Huang, "The Effect of Laser Scanning Path on Microstructure and Mechanical Properties of Laser Solid Formed Nicke0Based Superalloy Inconel 718," *Journal of Alloys and Compounds,* vol. 509, no. 2011, pp. 4505-4509, 2010.

[27] Y. Lu, S. Wu, T. Haung, C. Yang and L. Junjie, "Study on the microstructure, mechanical property and residual stress of SLM Inconel-718 alloy manufactured by differing island scanning strategy," *Optics and Laser Technology,* vol. 75, no. 2015, pp. 187-206, 2015.

[28] F. Lui, X. Lin, G. Yang, M. Song, J. Chen and W. Haung, "Microstrucutre and Residual Stress of Laser Rapid Formed Inconel 718 Nickel-Based Superalloy," *Optics and Laser Technology,* vol. 43, no. 2011, pp. 208-213, 2010.

[29] B. Vrancken, V. Cain, R. Knutsen and J. V. Humbeeck, "Residual Stress via the Countour Method in Compact Tension Specimens Produced via Selective Laser Melting," *Scripta Materialia,* vol. 87, no. 2014, pp. 29-32, 2014.

[30] E. Chlebus, K. Gruber, B. Kuznicka, J. Kurzac and T. Kurzynowski, "Effect of Heat Treatment on the Microstructure and Mechanical Proerties of Inconel 718 Precessed by Selective Laser Melting," *Materials Science and Engineering A,* vol. 639, no. 2015, pp. 647-655, 2015.

[31] D. Deng, R. L. Peng, H. Brodin and J. Moverare, "Microstrucutre and Mechanical Properties of Inconel 718 Produced by Selective Laser Melting: Sampel Orientation Dependence and effects of Post Heat Treatment," *Materials Science and Engnieering A,* vol. 713, no. 2018, pp. 294-306, 2018.

[32] G. J. Ram, A. V. Reddy, K. P. rao, G. Reddy and J. S. Sundar, "Microstrucutre and Tensile Properties of Inconel 718 Pulsed Nd-YAG Laser Welds," *Journal od Materials Processing Technology,* vol. 167, no. 2005, pp. 73-82, 2004.

[33] T. G. Spears and S. A. Gold, "In-process sensing in selective laser melting (SLM) additive manufacturing," *Integrated Materials and Manufactuing Innovation,* vol. 2016, no. 5, pp. 1-25, 2016.

[34] T. Purtonen, A. Kalliosaari and A. Salinen, "Monitoring and adaptive control of laser processes," *Physics Procedia,* vol. 56, no. 2014, pp. 1218-1231, 2014.

[35] M. Abdelrahman, E. W. Reutzel, A. R. Nassar and T. L. Starr, "Flaw detection in powder bed fusion using optical imaging," *Additive Manufacturing,* vol. 15, no. 2017, pp. 1-11, 2016.

[36] J. A. Kanko, A. P. Sibley and J. M. Fraser, "In Situ morphology-based defect detection of selective laser melting through inline coherent imaging," *Journal of Materials Processing Technology,* vol. 231, no. 2016, pp. 488-500, 2015.

[37] E. Rodriguez, J. Mireles, C. A. Terrazas, D. Espalin, M. A. Perez and R. B. Wicker, "Approximation of absolute surface temperature measurements of powder bed fusion additive manufacturing technology using in situ infrared thermography," *Additive Manufacturing,* vol. 5, no. 2015, pp. 31-39, 2014.

[38] J. Schwerdtfeger, R. F. Singer and C. Körner, "n situ flaw detection by IR-imaging during electron beam melting," *Rapid Prototyping Journal,* vol. 18, no. 4, pp. 259-263, 2012.

[39] R. B. Dinwiddie, R. R. Dehoff, P. D. Lloyd, L. E. Lowe and J. B. Ulrich, "Thermographic in-situ process monitoring of the electron-beam melting technology used in additive manufacturing," in *Proceedings of Spie,* Baltimore, Maryland, 2013.

[40] J. Raplee, A. Plotkowshi, M. Kirka, R. Dinwiddie, A. Okello, R. R. Dehoff and S. S. Babu, "Thermographic Microstructure Monitoring in Electron Beam Additive Manufacturing," *Scientific Reports,* vol. 7, no. 43554, pp. 1-16, 2016.

[41] B. Cheng, J. Lydon, K. Cooper, V. Cole, P. Northrop and K. Chou, "Melt pool sensing and size analysis in laser powder-bed additive manufactuing," *Journal of Manufacturing Process,* vol. 32, no. 2018, pp. 744-753, 2017.

[42] Y. Zhang, L. Li and G. Zhang, "Spectroscopic measurements of plasma inside the keyhole in deep penetration laser welding," *Journal of physics D: Applied Physics,* vol. 38, no. 2005, pp. 703-710, 2005.

[43] D. Lacroix, G. Jeandel and C. Boudot, "Spectroscopic characterization of laser-induced plasma created during welding with a pulsed Nd:YAG laser," *Journal of Applied Physics,* vol. 81, pp. 6599-6606, 1997.

[44] A. Ancona, V. Spagnolo, P. M. Lugara and M. Ferrara, "Optical sensor for real-time monitoring of CO2 laser welding process," *Applied Optics,* vol. 40, no. 33, pp. 6019-6025, 2001.

[45] T. Sibillano, A. Ancona, V. Berardi and P. M. Lugarà, "A Real-Time Spectroscopic Sensor for Monitoring Laser Welding Processes," *Sensors,* vol. 2009, no. 9, pp. 3376-3385, 2009.

[46] A. R. Nassar, T. J. Spurgeon and E. W. Reutzel, "Sensing defects during directed-energy additive manufacturing of metal parts using optical emissions spectroscopy".

[47] T. Sibillano, D. Rizzi, A. Ancona, S. Saludes-Rodil, J. Rodríguez Nieto, H. Chmelíc̆ková and H. Sebestová, "Spectroscopic monitoring of penetration depth in CO2 Nd:YAG and fiber laser welding processes," *Journal of Materials Processing Technology,* vol. 212, no. 2012, pp. 910-916, 2011.

[48] B. Ribic, P. Burgardt and T. DebRoy, "Optical emission spectroscopy of metal vapor dominated laser-arc hybrid welding plasma," *Journal of Applied Physics,* vol. 109, no. 083301, pp. 1-10, 2011.

[49] S. Clijsters, T. Craeghs, S. Buls, K. Kempen and J.-P. Kruth, "In situ quality control of the selective laser melting process using a high-speed, real-time melt pool monitoring system," *International Journal of Additive Manufactuing Technology,* vol. 75, no. 2014, pp. 1089-1101, 2014.

[50] Z. Szymanski, J. Kurzyna and W. Kalita, "The spectroscopy of the plasma plume indusced during laser welding of stainless steel and titanium," *Journal of Physics D: Applied Physics,* vol. 30, pp. 3153-3162, 1997.

[51] NIST, "NIST Atomic Spectra Database Lines Form," [Online]. Available: https://physics.nist.gov/PhysRefData/ASD/lines_form.html. [Accessed 20 3 2019].

[52] J. Middendorf, "In Process Monitoring of Additive Manufacturing," Dayton, 2018.

[53] Z. Szymanski and J. Kurzyna, "Spectroscopic measurements of laser induced plasma during welding with CO2 laser," *Journal of Applied Physics,* vol. 76, pp. 7750-7756, 1994.

[54] K. Bartowiak, "Direct laser deposition process within spectrographic analysis in situ," *Physics Procedia,* vol. 5, pp. 623-629, 2010.

[55] C. Aragon and J. Aguilera, "Characterization of laser induced plasmas by optical emission spectroscopy: A review of experiments and methods," *Spectrochimica Acta Part B,* vol. 63, pp. 893-916, 2008.

[56] L. Song and J. Mazumder, "Real Time Cr Measurment Using Optical Emission Spectroscopy During Direct Metal Deposition Process," *IEEE Sensors Journal,* vol. 12, no. 5, pp. 958-964, 2012.

[57] Thorlabs, "PDA36A2," Thorlabs, [Online]. Available: https://www.thorlabs.com/thorproduct.cfm?partnumber=PDA36A2. [Accessed 21 3 2019].

[58] W. G. Driscoll and W. Vaughan, Handbook of Optics, New York: Mcgraw-Hill Book Company, 1978.

[59] Basler, "acA1920-155um - Basler ace," [Online]. Available: https://www.baslerweb.com/en/products/cameras/area-scan-cameras/ace/aca1920-155um/. [Accessed 19 3 2019].

[60] B. K. Foster, E. W. Reutzel, A. R. Nassar, C. J. Dickman and B. T. Hall, "A brief survey of sensing for metal based powder bed fusion additive manufacturing," *SPIE,* vol. 9489, pp. 1-9, 2015.

[61] J. Byrnes, "Unexploded Ordnance Detection and Mitigation," Newport, RI, USA, Springer, 2009, pp. 21-22.

[62] Z. Yan, W. Liu, Z. Tang, X. Liu, N. Zhang, M. Li and H. Zhang, "Review on thermal analysis in laser-based additive manufactuing," *Optical Laser Technology,* vol. 106, pp. 427-441, 2017.

[63] T. Craeghs, S. Clijsters, E. Yasa, F. Bechmann, S. Berumen and J.-P. Kruth, "Determination of geometrical factors in layerwise laser melting using optical process monitoring," *Optics and Lasers in Engineering,* vol. 49, pp. 1440-1446, 2011.

[64] L. Song, C. Wang and J. Mazumder, "Identification of phase tranformation using optical emission spectroscopy for direct metal deposition process," *Proceedings of Spie,* vol. 8239, pp. 1-9, 2012.

[65] T. Craeghs, F. Bechmann, S. Berumen and J.-P. Kruth, "Feedback control of layerwise laser melting using optical sensors," *Physics Procedia,* vol. 5, pp. 505-514, 2010.